Phase transitions of three dimensional frustrated Heisenberg systems in an applied magnetic field

by

Daniel Maciel

A Thesis
Submitted to the Faculty of Graduate Studies
in Partial Fulfillment of the Requirements
for the Degree of

Master of Science

Department of Physics and Astronomy
University of Manitoba
Winnipeg, Manitoba

TABLE OF CONTENTS

LIST OF FIGURES

LIST OF TABLES

ACKNOWLEDGMENTS

I would like to begin by thanking my advisor Dr. Byron Southern, my committee, my parents, my significant other, and all the people who have supported me along the way. I would like to thank The Natural Sciences and Engineering Research Council, the University of Manitoba Graduate Enhancement of Tri-Council Stipends (GETS) for financial support. Finally I would like to thank the Compute Canada High Performance Computing Facilities for providing the resources to complete my thesis.

ABSTRACT

A study of three dimensional frustrated Heisenberg systems in an applied magnetic field is presented. Both the stacked triangular lattice and the FCC Kagome lattice are considered. Monte Carlo methods are used to determine the phase diagrams for nearest neighbour antiferromagnetic exchange in the presence of an applied field. Finite size scaling is used to determine the critical exponents which characterize the various phase boundaries.

Chapter 1

INTRODUCTION

Condensed Matter physics is the study of the physics of matter in a condensed state. In this context the term condensed is defined as matter held together due to internal interactions, the simplest and most common example being the solid state of matter. Analyzing systems composed of more than two particles is very difficult and requires a numerical approach. Studying condensed matter requires a statistical treatment of the physics of the many particle system since it is composed of billions of atoms. A statistical approach allows the study of the collective phenomena of the particles in the ensemble using measurable system quantities such as energy, order parameters and response functions. One of the most interesting collective phenomenon observed and studied is a phase transition. Phase transitions are commonly experienced in everyday life, not just in the lab! A common example is boiling a kettle of water where the liquid water undergoes a phase transition known as vaporization and changes from the liquid to gaseous state abruptly. Both states have different distinct properties, but are still chemically the same compound. These phase transitions arise whenever there are is a competition between interactions which influence the equilibirium state of the system. This equilibirium state can be influenced by varying external parameters such as temperature, pressure, and magnetic field for example. Studies of phase transitions using modern statistical methods, such as the Renormalization group, found that phase transitions could be classified into different universality classes. These universality classes could relate systems composed of

different particles but sharing common symmetries. Each class is defined by a set of critical exponents that describe how various physical quantities of the system behave near a phase transition. Therefore study of phase transitions has a strong focus on the determination and/or classification of the relevant universality class for the transition.

Studying these many body systems requires a numerical approach since analytic calculations are extremely difficult. Therefore the role of numerical physics in studying these phase transitions has proven to be crucial and invaluable. One of the major numerical methods employed by physicists is the Monte Carlo Method and its different variants. The Monte Carlo methods allow sampling of the different system quantities in their equilibirum state, which then allows for analysis of the system at a transition.

Condensed matter physics studies the collective phenomena due to competing and/or cooperative interactions in a system as a result of frustration within the system. A frustrated system is a system in which competing interactions in the system cannot be mutually optimized. Therefore the system takes on a non-trivial state due to this competition and often times these non-trivial states lead to a degeneracy in the low-energy modes of the equilibirum configuration. The degenerate energy states in these frustrated systems can lead to a non-zero entropy at zero temperature. Frustration in magnetic systems can be easily realized and are therefore the study of the phase transitions leads to interesting physics due to the highly degenerate states. Frustration can also be due to the underlying geometry of the system. Geometrically frustrated magnetic systems are usually composed of triangular plaquettes which either share a common corner (Kagome) or edge (Triangular) in the lattice.

During the past 30 years there has been a large interest in the nature of phase transitions in frustrated systems in both two and three dimensions on triangular geometries[1]. In particular, the two dimensional triangular lattice and its three dimensional stacked version with nearest neighbour antiferromagnetic interactions in both zero and non-zero applied magnetic fields have been investigated [2, 3, 4, 5, 6, 7, 8, 9]. Both the xy and Heisenberg models exhibit degeneracies in the presence of

a field which appear to be lifted at finite temperature due to an order from disorder process[10, 2, 7]. The nature of the phase transition in the zero field three dimensional model was debated for many years but Monte Carlo studies have confirmed that the system exhibits a weak first order transition at a finite temperature[11]. The two dimensional Kagome lattice has also been studied by many groups[12, 13, 14]. In zero field, there is a macroscopic degeneracy in the ground state and the system does not order. In the presence of an applied field the system exhibits multi-pole ordering[15]. More recent work has considered a three dimensional frustrated lattice which consists of abc stacked Kagome planes in both zero and non-zero applied fields[16, 17, 18]. This latter lattice is referred to as the FCC Kagome lattice. This three dimensional lattice also exhbits degeneracy of the ground state in both zero and non-zero applied magnetic fields. Although the phase diagrams as a function of temperature and field of these systems has been obtained previously, the detailed critical behaviour of the phase boundaries has not been studied.

In this thesis, a detailed study of the three dimensional stacked triangular lattice and the FCC Kagome lattice will be carried out using Monte Carlo methods to determine the nature of the phase transitions in an applied field. The thesis is organized as follows. Chapter 2 provides some basic background on magnetic interactions. The lattice geometries and an analysis of the ground state properties is given in Chapter 3 along with a discussion of degeneracies. In Chapter 4 the various order parameters and response functions that are measured are introduced and in Chapter 5 the Monte Carlo method is described as well as the finite size scaling technique. Chapters 6 and 7 present the results for the triangular and Kagome lattices respectively. Finally Chapter 8 provides a summary and conclusion.

Chapter 2

MAGNETIC HAMILTONIAN

2.1 The Spin Hamiltonian

The model Hamiltonian which will be considered consists of exchange interactions between localized classical spins situated at the sites of a periodic lattice. In addition, the Zeeman interaction of an externally applied magnetic field with the magnetic moment associated with a spin is also included. The next subsections will briefly describe the origins of these magnetic terms in the Hamiltonian.

2.1.1 Exchange Interaction

The exchange interaction is a purely quantum mechanical effect that is a result of the Coulomb repulsion between neighbouring electrons. Remarkably this result can be expressed simply in terms of the dot product between the spins of these neighbouring electrons by considering the energetic contributions from their kinetic energy and Coulomb energy, due to interactions with other protons and electrons in the system, from a quantum mechanical viewpoint. Since the exchange interaction arises from the Coulomb interaction it is a strong effect at room temperature and above. It is this term in our Hamiltonian which is responsible for the *magnetic ordering* in the frustated systems that were studied. Although other interactions can bring about magnetic ordering as well, such as dipole interactions, only exchange interactions were considered in this study.

To understand the origins of this interaction, consider a simple example of two hydrogen-like atoms near each other (an electron orbiting a proton in close proximity

to another electron orbiting another proton). Assuming that the protons are at fixed positions, we consider only the kinetic energy of the electrons and the Coulomb potential energy between the charged particles and we have the following Hamiltonian:

$$\mathcal{H} = \frac{\hat{p_1}^2 + \hat{p_2}^2}{2m_e} + e^2(\frac{1}{r_{ab}} + \frac{1}{r_{12}} - \frac{1}{r_{a1}} - \frac{1}{r_{a2}} - \frac{1}{r_{b1}} - \frac{1}{r_{b2}}) \tag{2.1}$$

where m_e is the mass of the electrons, e is the charge of the electron, r is the distance between particles with the subscripts a, b denoting the protons and subscripts $1, 2$ are used to denote the electrons. We note that there is no explicit dependence on spin in this Hamiltonian and therefore the total spin operator $\hat{S}^2_{tot} = (\hat{S}_1 + \hat{S}_2)^2$ trivially commutes with the Hamiltonian operator and we can expect the energy eigenfunctions of this Hamiltonian to also be an eigenfunction of $\hat{S}_{tot}$. Therefore the wave function Ψ can be written as a simple product of the spatial wave function and a spinor for the total spin.

$$\Psi(\vec{r}_1, \vec{r}_2, \sigma_1, \sigma_2) = \Phi_{spatial}(\vec{r}_1, \vec{r}_2)\chi_{spin}(\sigma_1, \sigma_2) \tag{2.2}$$

Here σ_1 and σ_2 are the electron spin projections onto a given axis, with $\vec{r}_1$ and $\vec{r}_2$ being the position vectors of the electrons. As χ is a spinor of the total spin S_{tot}, we can expect to find it in either the triplet ($S_{tot} = 1$) states or in the singlet ($S_{tot} = 0$) state. Since the electrons are identical fermions and obey Fermi-Dirac statistics, Ψ must be anti-symmetric upon interchange of the coordinates (position and spin) of the two electrons as follows

$$\Psi(\vec{r}_1, \vec{r}_2, \sigma_1, \sigma_2) = -\Psi(\vec{r}_2, \vec{r}_1, \sigma_2, \sigma_1) \tag{2.3}$$

Since Ψ is a product of spatial and spin eigenfunctions, this antisymmetry of the wave function imposes restrictions on how Φ and χ are combined. A symmetric spatial function Φ_S must be combined with an anti-symmetric spin function χ_A and an antisymmetric spatial function Φ_A must be combined with a symmetric spinor χ_S

to preserve the overall antisymmetry of the resulting wave function. The spin function χ is symmetric when in the triplet ($S_{tot} = 1$) states and antisymmetric when in the singlet ($S_{tot} = 0$) state. We can therefore construct the following two allowed wave function compositions:

$$\Psi(\vec{r}_1, \vec{r}_2, \sigma_1, \sigma_2) = \begin{cases} \Phi_A(\vec{r}_1, \vec{r}_2)\chi_S(\sigma_1, \sigma_2) & \text{if } S_{tot} = 1 \\ \Phi_S(\vec{r}_1, \vec{r}_2)\chi_A(\sigma_1, \sigma_2) & \text{if } S_{tot} = 0 \end{cases} \tag{2.4}$$

We can construct the spatial wave functions using symmetric and anti-symmetric combinations of the individual electronic wave functions $\phi_a(\vec{r}), \phi_b(\vec{r})$ where these are taken to be the ground state wave functions of the two hydrogen atoms a and b. These are considered to be normalized energy eigenfunctions of their corresponding electrons in position space. The symmetic and antisymmetric combinations are

$$\Phi_S(\vec{r}_1, \vec{r}_2) = \frac{1}{\sqrt{2(1+c^2)}}(\phi_a(\vec{r}_1)\phi_b(\vec{r}_2) + \phi_a(\vec{r}_2)\phi_b(\vec{r}_1)) \tag{2.5}$$

$$\Phi_A(\vec{r}_1, \vec{r}_2) = \frac{1}{\sqrt{2(1-c^2)}}(\phi_a(\vec{r}_1)\phi_b(\vec{r}_2) - \phi_a(\vec{r}_2)\phi_b(\vec{r}_1)) \tag{2.6}$$

where c is a normalization constant given by

$$c = \int \phi_a^*(\vec{r})\phi_b(\vec{r})d^3r = \int \phi_b^*(\vec{r})\phi_a(\vec{r})d^3r \tag{2.7}$$

and is called the *Overlap Integral*.

Using these symmetrized wave functions we take the expectation value of the Hamiltonian ($2.1 Exchange Interaction equation.2.1.1$) defined earlier to see if the energy depends on the relative spin orientation. Since the Hamiltonian does not explitictly depend on the spins, the spin functions factor out of this calculation and do not affect the energy. This procedure yields the following equations for the energy:

$$E_{+/-} = \frac{A \pm B}{(1 \pm c^2)} \tag{2.8}$$

where E_+ corresponds to the energy calculated using the symmetric spatial wave function and E_- corresponds to the energy found using the antisymmetric spatial wave function. A and B are integrals defined by:

$$A = \iint \phi_a^*(\vec{r}_1)\phi_b^*(\vec{r}_2)\hat{H}\phi_a(\vec{r}_1)\phi_b(\vec{r}_2)d^3r_1d^3r_2 \tag{2.9}$$

$$B = \iint \phi_a^*(\vec{r}_2)\phi_b^*(\vec{r}_1)\hat{H}\phi_a(\vec{r}_1)\phi_b(\vec{r}_2)d^3r_1d^3r_2 \tag{2.10}$$

The symmetry of the spatial wave functions does indeed affect the energy and the difference between the two energy levels is given by:

$$J = \frac{E_- - E_+}{2} = \frac{Ac^2 - B}{1 - c^4} \tag{2.11}$$

where J is called the *exchange constant*. Note that when the hydrogenic wave functions do not overlap, c and B are zero and $J = 0$. Hence overlap of the wave functions is required to produce J. The eigenvalues of the $\hat{S}_{tot}^2$ operator are $S(S+1)$ (setting $\hbar = 1$) and using the relation

$$< \hat{S}_{tot}^2 >=< \hat{s}_1^2 > + < \hat{s}_2^2 > +2 < \hat{s}_1 \cdot \hat{s}_2 > \tag{2.12}$$

we can determine the expected value of the inner product of the two spins

$$< \hat{s}_1 \cdot \hat{s}_2 >= \begin{cases} -\frac{3}{4} & \text{if } S = 0 \\ \frac{1}{4} & \text{if } S = 1 \end{cases} \tag{2.13}$$

Using equations (2.11$ExchangeInteractionequation$.2.1.11) and (2.13$ExchangeInteractionequa$ we can recast our Hamiltonian (2.1$ExchangeInteractionequation$.2.1.1) in terms of the spins of the two electrons as follows

$$\mathcal{H}_{exchange} = -2J < \hat{s}_1 \cdot \hat{s}_2 > +\frac{3}{4}E_+ + \frac{1}{4}E_- \tag{2.14}$$

We see that when $S_{tot} = 1$ we get the E_+ energy and when $S_{tot} = 0$ we get E_-. These are the same results that we arrived at previously but we have recast the Hamiltonian simply in terms of the spins of the atoms when there were previously no spin dependence in the Hamiltonian. This is a very powerful result as the electronic Kinetic and Coulomb interactions are condensed into a simpler spin dependent equation. This result is simply due to the symmetry requirements of the wave function and the Pauli exclusion principle. We also note that the sign of the exchange constant J is physically significant since positive exchange will prefer to align the two spins to minimize the energy, while the a negative exchange will want to anti-align the electron spins. This characteristic leads to the origins of the macroscopic phenomena known as *Ferromagnetism* and *Anti-Ferromagnetism* respectively.

This simple example can then be expanded upon by considering a many electron system, where the exchange Hamiltonians of all electron pairs are added together. The constant terms are then ignored as Dirac[19] noted that the critical features of the system could be extracted by simply considering potentials of the form of the coupled electron spins. The Hamiltonian was then written as:

$$\mathcal{H}_{Heisenberg} = \frac{1}{2}\Big(\sum_{(i,j)}^{N} -2J_{ij}\langle S_i \cdot S_j\rangle\Big) = -\sum_{(i,j)}^{N} J_{ij}\langle S_i \cdot S_j\rangle \tag{2.15}$$

The factor of $\frac{1}{2}$ is multiplied throughout so as to prevent double counting as the sum is taken over all indices i, j and N is the total number of electrons. J_{ij} is a matrix element of the **J** matrix which consists of the exchange constants calculated between electrons i and j. This matrix is necessarily symmetric as the exchange term is the same between two electrons. This Hamiltonian is usually called the *Heisenberg Hamiltonian*[20] or the *Heisenberg-Dirac Hamiltonian*[19] as it was independently derived by both parties. This is the first term in our spin Hamiltonian.

2.1.2 Zeeman Energy

Since electrons are elementary charged particles, their spin angular momentum has a dipole moment called the *Spin Magnetic Moment*. In the presence of an external field an electron's spin moment contributes directly to the total energy of the system. The spin-magnetic moment $\vec{\mu_s}$ of an electron is defined as:

$$\vec{\mu_s} = -g_s \frac{e}{2m_e} \vec{S} = -\frac{g_s \mu_B}{\hbar} \vec{S} \tag{2.16}$$

where $\mu_B = \frac{\hbar e}{2m_e}$ is the *Bohr Magneton* and is the natural unit used to describe the magnetic moment of the electron. The factor g_s is the *Landé g-factor* which is a dimensionless factor, and for electrons is $g_s \approx -2$. It's important to note that this g-factor is negative as it implies that the electron's spin moment points in the same direction as it's spin. The energy contribution due to the spin magnetic moment with the applied field is just the usual Zeeman interaction energy of a magnetic dipole with an external field B_{ext}.

$$E_{Zeeman} = -\vec{\mu}_s \cdot \vec{B}_{ext} \tag{2.17}$$

While this may look like a classical dipole interaction, this energy contribution is quantum mechanical in nature as spin is an intrinsic property of elementary particles. As in the classical case, this energy is minimized when the dipole is aligned with B_{ext} and maximum when anti-aligned. However, unlike the classical case the spin-magnetic moment is quantized to be either $\pm\frac{\hbar}{2}$ on a projected axis and splits the quantum energy levels.

Now considering a many-electron system again with N total electrons we simply sum the individual contributions due to each moment leading to the following:

$$\mathcal{H}_{Zeeman} = -\sum_{i}^{N} \vec{\mu}_i \cdot \vec{B}_{ext} \tag{2.18}$$

This is the total energy contribution made by the spin-magnetic moments in our N-electron system.

2.2 Assumptions and Simplifications

We would now wish to combine our Hamiltonians (2.15$ExchangeInteractionequation$.2.1.15) and (2.18$ZeemanEnergyequation$.2.1.18) and make a few simplifying assumptions to arrive at our Hamiltonian used to model our analysis of magnetism of the different 3-D lattices we will be studying.

$$\mathcal{H} = -\sum_{(i,j)}^{N} J_{ij} S_i \cdot S_j - \sum_{i}^{N} \vec{\mu}_i \cdot \vec{B}_{ext} \tag{2.19}$$

We will further simplify this by assuming that on a lattice only exchange between nearest neighbours is significant, and set non-nearest neighbour matrix elements of J_{ij} to zero. This is a reasonable simplification as the exchange interaction falls with distance, as it requires overlap of the electronic wave functions for the integrals non-zero. The further apart the electrons are positioned on the lattice results in a much-reduced overlap of the wave functions. Therefore the exchange term is now only summed over nearest neighbours. On a regular bravais lattice the inter-atomic spacing between nearest neighbours is the same and therefore the exchange constant betweeen electrons on nearest neighbour atoms is the same.

We would also like to simplify the Zeeman term and rewrite it in terms of spin. Therefore we define

$$\vec{H} = \frac{|g_s|\mu_B}{\hbar} \vec{B}_{ext} \tag{2.20}$$

This allows us to write the Zeeman energy in terms of a simple dot product. Our Hamiltonian now reads as:

$$\mathcal{H}_{spin} = -J \sum_{<i,j>}^{N} S_i \cdot S_j - \sum_{i}^{N} \vec{S}_i \cdot \vec{H} \tag{2.21}$$

where the sum over $< i, j >$ denotes a sum over all nearest neighbour pairs for each particle. For the purposes of our studies and simulations we will also assume classical spins by allowing them to vary continuously from -1 to 1 as opposed to the fixed values of $\pm\frac{\hbar}{2}$ onto a given axis. This is a reasonable assumption as many electron systems have a very large spin quantum number resulting in a large amount of projections onto the unit sphere as the number of allowable states goes with the spin quantum number as $2s + 1$, therefore allowing the continuum limit to be taken reasonably. This assumption is also necessary for the Monte Carlo methods employed to study the finite temperature properties.

Chapter 3

GEOMETRICAL FRUSTRATION

The main focus of this study is the effect of frustration due to the geometry of the lattice of the magnet on the nature of phase transitions in the presence of an applied field. In this chapter we will discuss two types of geometrically frustrated lattices that will be studied, those being the 2-D/3-D Triangular lattices and the 2-D/FCC Kagome lattice structures. Both of these types of lattice structures involve triangles of spins which either share edges or vertices. In the case of antiferromagnetic exchange interactions, the triangular units are *frustrated*.

Consider a situation in which we have one isolated triangle and set the spins on this lattice in such a way as to satisfy the antiferromagnetic bonds between them. With no external forces or fields acting on the system, we simply need to minimize the exchange energy between these spins. If we fix two vertices with spins pointing in opposite directions to minimize their exchange energy, the third spin would then be unable to simultaneously anti-align with the other two spins as shown if Fig 3.1A frustrated triangle. If two spins are anti-parallel, the third spin cannot be anti-parallel to the other twofigure.3.1. We say therefore that this system is frustrated as there is no way to have all pairs of spins simultaneously anti-parallel. In the case of vector spins, there are two minimum energy states on a single triangle which correspond to the spins $\vec{S}_A, \vec{S}_B$ and $\vec{S}_C$ at the vertices of the triangle satisfying the condition

$$\vec{S}_A + \vec{S}_B + \vec{S}_C = 0 \tag{3.1}$$

as shown in Fig. 3.2A planar ground state for a single triangle in the absence of an applied field. a) 120° has positive chirality b) 240° has negative chiralityfigure.3.2. All

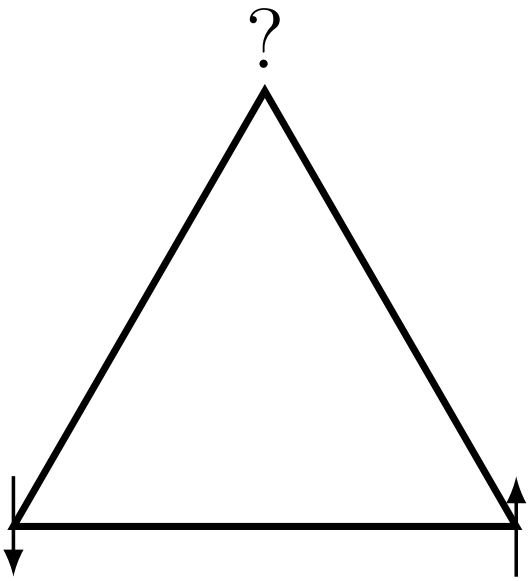

Figure 3.1: A frustrated triangle. If two spins are anti-parallel, the third spin cannot be anti-parallel to the other two.

three spins lie in a plane and form either a 120° or 240° structure which are referred to as plus and minus chiralities. These structures are named as such because the spins on the triangles arrange themselves such that there is a common angle of either 120° or 240° between all three spins.

3.1 Triangular Lattices

The 2-D triangular lattice consists of a plane of edge sharing triangles with a magnetic spin on each site as shown in Fig.3.3The 2-D triangular lattice can be decomposed into three inter-penetrating triangular sublattices A,B and C. Each elementary triangle contains a spin from each sublattice and shares edges with adjacent trianglesfigure.3.3 . When there are anti-ferromagnetic interactions between each of the six nearest neighbours on the lattice, the spins on each triangle are frustrated. However, if

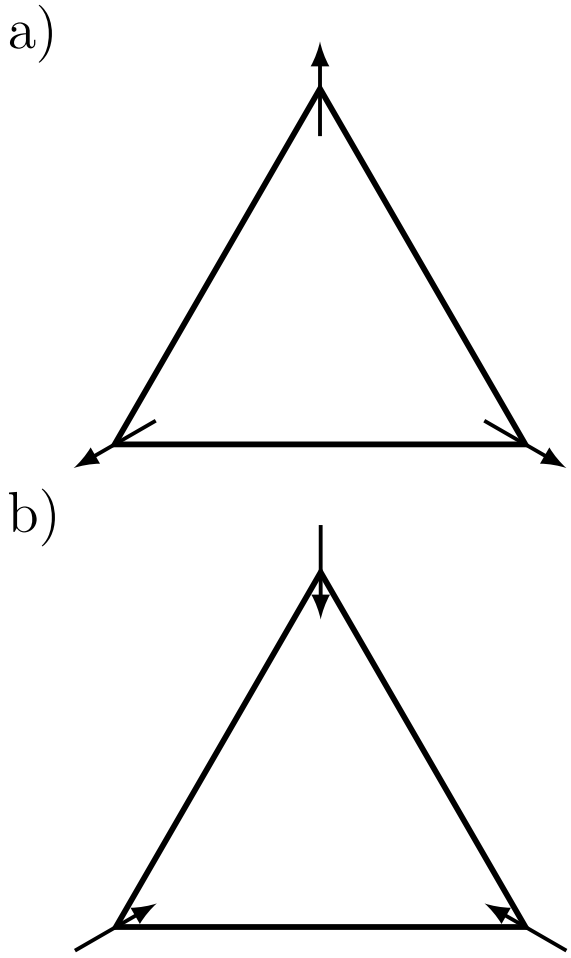

Figure 3.2: A planar ground state for a single triangle in the absence of an applied field. a) 120° has positive chirality b) 240° has negative chirality

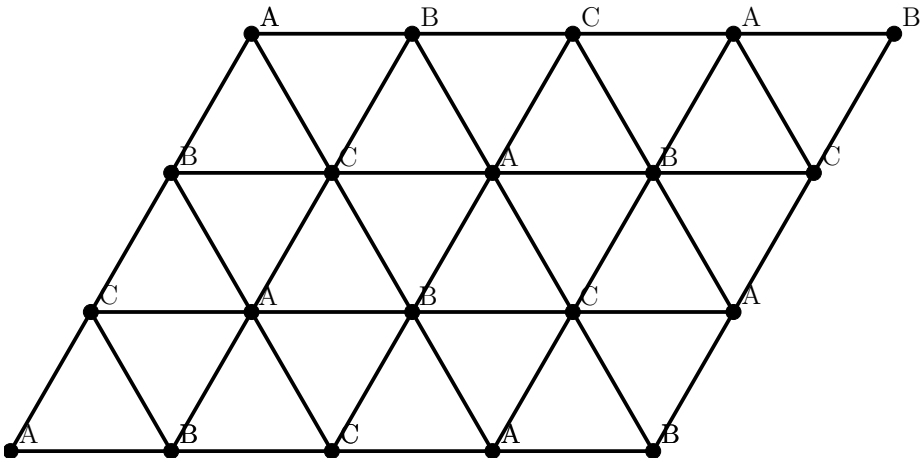

Figure 3.3: The 2-D triangular lattice can be decomposed into three inter-penetrating triangular sublattices A,B and C. Each elementary triangle contains a spin from each sublattice and shares edges with adjacent triangles.

we fix the spins on one triangle into a valid ground state, then that triangle will determine it's neighbouring triangle's configurations. These neighbouring triangles will then determine their neighbours and so on. This feature is due to the fact that this lattice is composed of *edge-sharing* triangles and therefore each triangle shares two of its spins with each neighbouring triangle. The condition in (3.1Geometrical Frustrationequation.3.0.1) propagates the order throughout the lattice. The lattice can be divided into three interpenetrating triangular lattices and we label the spins on each sublattice as $\vec{S}_A$, $\vec{S}_B$ and $\vec{S}_C$ respectively. The spins on each site belonging to the same sublattice are collinear.

A natural extension of this type of lattice to three dimensions is the so called *stacked* triangular lattice which is realized in many rare earth compounds[1]. This type of lattice is formed from taking 2-D planes of the triangular lattice and stacking them directly on top of each other, introducing two more magnetic neighbours located above and below each spin on the plane. The nature of the interaction between planes can be either ferromagnetic or anti-ferromagnetic. The interplanar spacing between

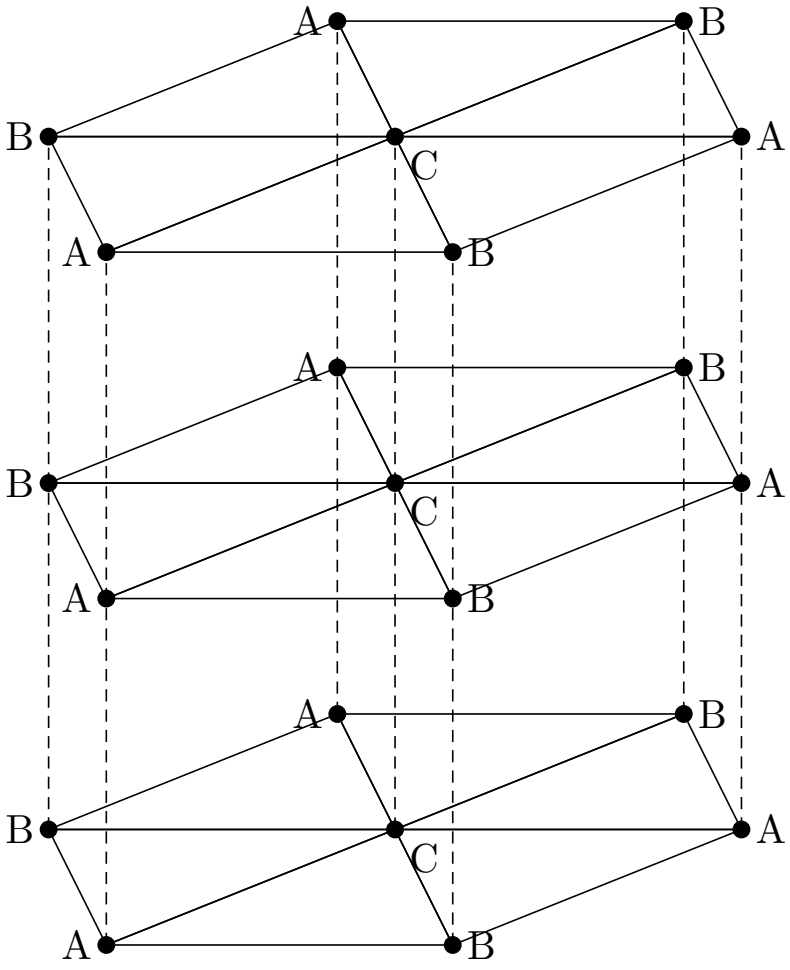

Figure 3.4: The stacked triangular lattice with 2D planes stacked directly on top of each other. Each site interacts anti-ferromagnetically with 6 nearest neighbours on different sublattices within the same plane and ferromagnetically with two nearest neighbours on the same sublattice in the planes above and below.

the 2-D planes can be relatively large or small compared to the spacing between nearest neighbours in the plane. We will assume a ferromagnetic coupling between planes with an interplanar spacing equal to the spacing between nearest neighbours in the plane.

The similarities between this 3-D lattice and the 2-D lattice are striking. The ability to fix the triangular spins in the plane is unaffected as each plane will still have the same features as before. As the coupling between the planes is ferromagnetic in nature the neighbours outside the plane therefore choose to exactly align with their out of plane neighbours. This allows us to apply the same lattice partitioning on this lattice into three triangular sublattices as in the 2-D case.

3.2 Kagome Lattices

The Kagome lattice is a more exotic lattice compared to the triangular lattice and can be thought of as a natural derivative of the latter. Starting with the 2-D triangular lattice, we can partition the lattice into four triangular sublattices A, B, C and D. We 'turn off' the spins on the D sublattice, essentially deleting them from the lattice as they are now occupied by non-magnetic particles and will not interact magnetically with their neighbours. The resulting lattice is shown in Fig. 3.5The Kagome lattice is formed by partitioning the triangular lattice into four triangular sublattices and removing the spins on one of the sublattices. The arrangement of the A, B and C sublattices with their spins in a plane at 120° is called the $q = 0$ statefigure.3.5 and is referred to as the $q = 0$ state[12] since each upward triangle has the same sublattice configuration.

As in the 2-D triangular case, we have three magnetic sublattices interacting with each other. However, in contrast to the 2-D triangular lattice, the triangles now only share a vertex with their nearest neighbour triangles and this reduces the number of nearest neighbour bonds from six to four. Spins on the entire lattice can still

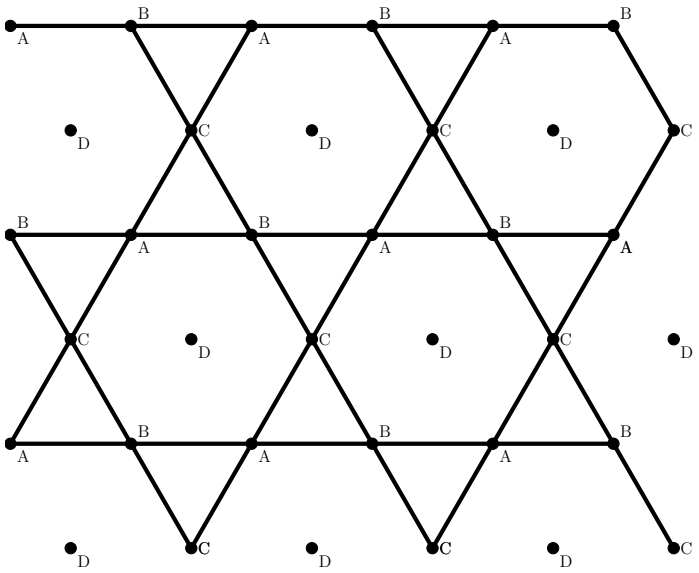

Figure 3.5: The Kagome lattice is formed by partitioning the triangular lattice into four triangular sublattices and removing the spins on one of the sublattices. The arrangement of the A, B and C sublattices with their spins in a plane at 120° is called the $q = 0$ state

be defined by setting the spins on one triangle and giving each sublattice the same vectors throughout the lattice. However there are additional degeneracies introduced due to the fact the triangles only share a single vertex as two spins in a neighbouring triangle can be swapped at no cost in energy resulting in a valid ground state. The 2-D Kagome system has a macroscopic entropy at zero temperature and there is no long ranged magnetic order at finite temperatures[13]. Fig. 3.6A periodic ground state with the same energy as that in Fig. 3.5 but with a larger unit cell. This configuration of the sublattices is called the $\sqrt{3} \times \sqrt{3}$ statefigure.3.6 shows another possible periodic state composed of three sublattices with the same energy but in this case each of the sublattices are also Kagome lattices. This latter configuration is called the $\sqrt{3} \times \sqrt{3}$ state[12] since there are now three types of upward triangles with different sublattice configurations.

A 3-D lattice which consists of stacked Kagome planes along the [111] direction

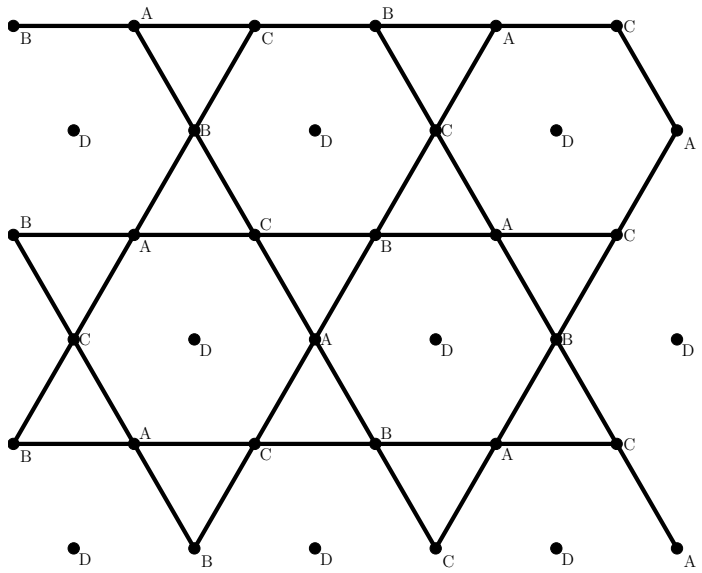

Figure 3.6: A periodic ground state with the same energy as that in Fig. 3.5 but with a larger unit cell. This configuration of the sublattices is called the $\sqrt{3} \times \sqrt{3}$ state.

can be constructed by dividing an FCC lattice into 4 interpenetrating cubic lattices A, B, C and D and choosing the D sites to be nonmagnetic. This structure is realized in $IrMn_3$ which is an important material in hard drives[21]. Figs. 3.7a)The corners of the cube are non-magnetic sites D and correspond to removing 1/4 of the sites. The sublattices A, B and C are on the face-centers of the cube. Note that the B, C sites lie in a plane between the A sites. b) The Kagome planes are stacked along the [111] directionfigure.3.7 and 3.8A [1,1,1] plane of the FCC lattice with 1/4 of the sites removedfigure.3.8 show an FCC lattice with 1/4 of the sites removed. It has planes of kagome lattices stacked on top of each other in a staggered fashion along the [111] direction. Each magnetic site has eight nearest neigbours with four in the plane and two above and below in the next plane. The sublattices A, B and C belong to triangles which share vertices but no edges. We refer to this lattice as the *FCC Kagome Lattice*. This lattice also has a degeneracy related to sublattice switching[16]. If we fix the spins on one triangle and set the spins on each sublattice parallel to one another,

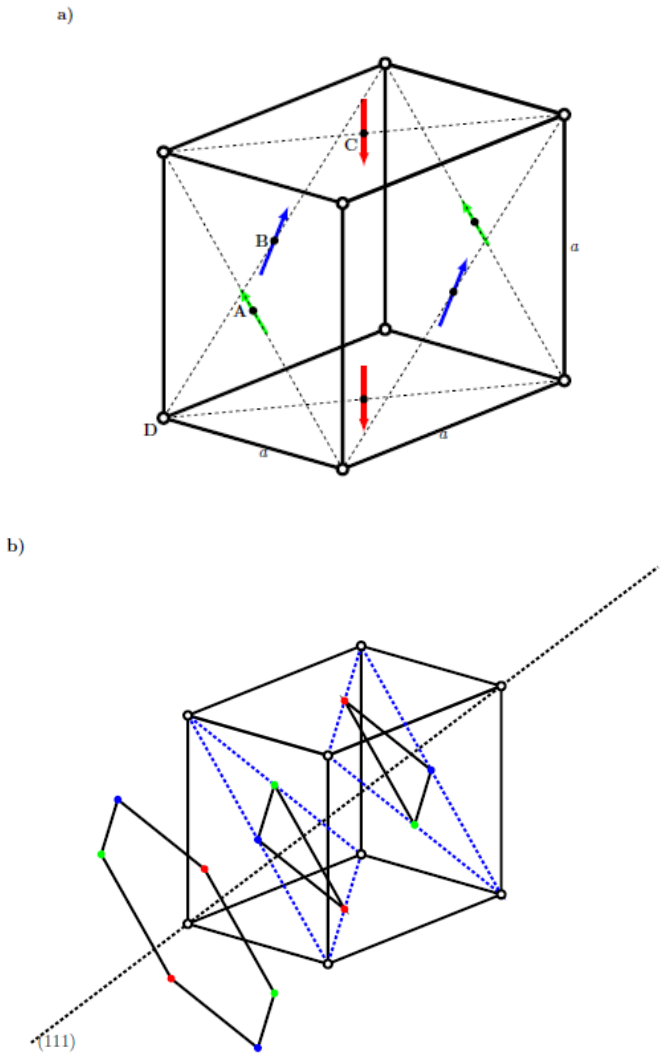

Figure 3.7: a)The corners of the cube are non-magnetic sites D and correspond to removing 1/4 of the sites. The sublattices A, B and C are on the face-centers of the cube. Note that the B, C sites lie in a plane between the A sites. b) The Kagome planes are stacked along the [111] direction.

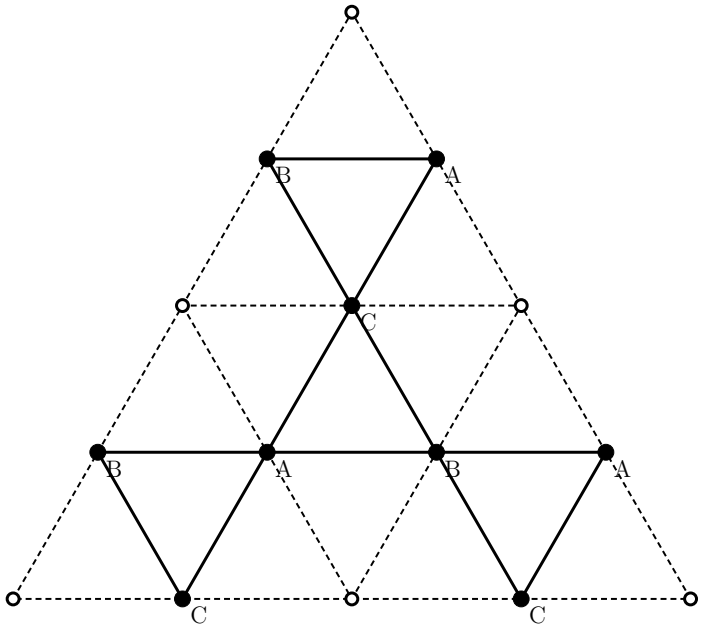

Figure 3.8: A [1,1,1] plane of the FCC lattice with 1/4 of the sites removed.

then we have a ground state characterized by $\vec{S}_A + \vec{S}_B + \vec{S}_C = 0$. However, as can be seen in Fig. 3.7a)The corners of the cube are non-magnetic sites D and correspond to removing 1/4 of the sites. The sublattices A, B and C are on the face-centers of the cube. Note that the B, C sites lie in a plane between the A sites. b) The Kagome planes are stacked along the [111] directionfigure.3.7 the B and C sites lie in planes between the A sites. If we interchange all of the B and C spin directions in any one plane, it will not change the energy and is a valid ground state. However, the entropy at zero temperature is not macroscopic and a phase transition occurs at a finite temperature[16].

3.3 Zero Temperature Analysis

Now that we have introduced the main lattice types that will be analyzed in this thesis, we will consider a general derivation of the zero temperature configurations in

a finite field. Consider a lattice of N magnetic sites composed of triangles in some sort of interlocking way, with anti-ferromagnetic interactions between nearest neighbours. If we impose the condition that it can be divided into three sublattices located at the vertices of each triangle, which we label A,B and C, we can perform an exact analysis of the ground state energy. We label the spins on the sublattices $\vec{S}_A$, $\vec{S}_B$, and $\vec{S}_C$ respectively.

We now introduce z, the number of nearest neighbours of each lattice site. Each spin in the lattice belongs to $\frac{z}{2}$ triangles and since there are three spins per triangle, we can define the total number of triangles in the lattice as $\frac{1}{3}\frac{Nz}{2}$. If we divide this expression by N we get the number of triangles per site $\frac{z}{6}$. Referring back to our spin Hamiltonian (2.21Assumptions and Simplificationsequation.2.2.21), the energy on each triangle is

$$E_\Delta = J(\vec{S}_A \cdot \vec{S}_B + \vec{S}_B \cdot \vec{S}_C + \vec{S}_C \cdot \vec{S}_A) - \frac{\vec{H} \cdot (\vec{S}_A + \vec{S}_B + \vec{S}_C)}{\frac{z}{2}} \tag{3.2}$$

where $J > 0$ is the nearest neighbour anti-ferromagnetic coupling. The Zeeman term in the energy is divided by the number of triangles belonging to the spin to prevent double counting. We can recast this equation in terms of one variable instead of three as follows. We define $\vec{m} = \frac{(\vec{S}_A+\vec{S}_B+\vec{S}_C)}{3}$ as the net magnetization per site on a triangle. Rewriting the coupled spins in the energy as a square of their sums and since the spins are normalized to unity, we arrive at the following expression:

$$\vec{S}_A \cdot \vec{S}_B + \vec{S}_B \cdot \vec{S}_C + \vec{S}_C \cdot \vec{S}_A = \frac{(\vec{S}_A + \vec{S}_B + \vec{S}_C)^2 - \vec{S}_A^2 - \vec{S}_B^2 - \vec{S}_C^2}{2} = \frac{9\vec{m} \cdot \vec{m} - 3}{2} \tag{3.3}$$

Rewriting our earlier expression for E_Δ (3.2Zero Temperature Analysisequation.3.3.2) in terms of $\vec{m}$ yields

$$E_\Delta = \frac{J}{2}(9\vec{m} \cdot \vec{m} - 3) - \frac{6}{z}\vec{H} \cdot \vec{m} \tag{3.4}$$

and multiplying E_Δ by $\frac{z}{6}$ gives the total energy per magnetic site.

$$E_{site} = \frac{zJ}{12}(9\vec{m}\cdot\vec{m} - 3) - \vec{H}\cdot\vec{m} \tag{3.5}$$

This equation can now be minimized with respect to $\vec{m}$, and we find that this function is minimal when

$$\vec{m}_{min} = \frac{2}{3zJ}\vec{H} \tag{3.6}$$

When $|\vec{H}| > \frac{3zJ}{2}$ the spins are saturated and all point in the direction of the field with $\vec{m} = \hat{H}$. However when $|\vec{H}| < \frac{3zJ}{2}$, there are many different sublattice orderings allowed. Substituting the solution for $\vec{m}$ into the energy we find

$$\begin{aligned} E_{site} &= -\frac{zJ}{4} - \frac{H^2}{3zJ} \quad H < \frac{3zJ}{2} \\ &= \frac{zJ}{2} - H \qquad H > \frac{3zJ}{2} \end{aligned} \tag{3.7}$$

The sublattice vectors satisfy

$$\vec{S}_A + \vec{S}_B + \vec{S}_C = \frac{2}{z}\vec{H} \tag{3.8}$$

Hence the components of the sublattice vectors perpendicular to $\vec{H}$ sum to zero. Since each sublattice vector is characterized by two angles, we have six degrees of freedom and only 3 constraints. Hence there is a large degeneracy of solutions. However, as we shall discuss in later chapters, there is a selection of planar states at finite temperatures that minimize the free energy. We will assume that the sublattice vectors lie in a plane and that the magnetic field is in the z-direction $\vec{H} = H\hat{z}$.

We begin the analysis at $\vec{H} = 0$, therefore the magnetization $\vec{m} = 0$ which by definition means we must solve the following equation:

$$(\vec{S}_A + \vec{S}_B + \vec{S}_C) = 0 \tag{3.9}$$

As can easily be seen there are a multitude of valid solutions to this equation. Using

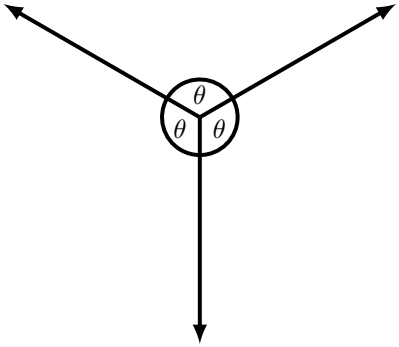

Figure 3.9: At $H = 0$ the resultant co-planar phase on the triangle results in an equal 120 degree separation between the spins on the triangle

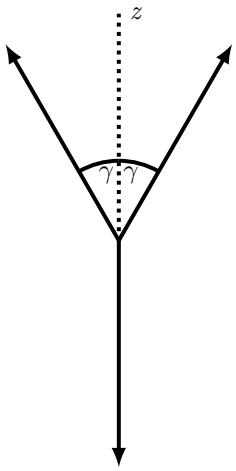

Figure 3.10: For $0 < H \leq \frac{3zJ}{2}$ the 120 degree structures becomes distorted as the magnetic field increases. As the field becomes stronger the angle γ decreases.

our knowledge that the the spins on the triangle assume a co-planar state to minimize their energy and the fact that the bonds between spins are anti-ferromagnetic we can refine our picture of this ground state. Due to the repulsive nature of the anti-ferromagnetic terms the three spins on the triangle will separate themselves with an equal angle between each spin. Therefore it is easily seen that each spin must be separated by an angle of $\frac{2\pi}{3}$ (120 degrees) as indicated in Fig. 3.9At $H = 0$ the resultant co-planar phase on the triangle results in an equal 120 degree separation between the spins on the trianglefigure.3.9. This 120 degree structure can be oriented on any plane in spin space as there is no magnetic field present which would influence the direction.

When the magnetic field is slowly turned on, the plane will align with the field. However the anti-ferromagnetic interactions are still strong and the spins will still prefer to be anti-aligned. The 120 degree structure will become distorted with one spin anti-aligned with the field, with the other two spins attempting to align with the field along the z-axis. Defining the angle γ to be the angle that the two spins make with the field axis,we find the z-components of each spin on the triangle to be $S_A^z = S_B^z = \cos\gamma$ with the anti-aligned spin having $S_C^z = -1$ as shown in Fig. 3.10For $0 < H \leq \frac{3zJ}{2}$ the 120 degree structures becomes distorted as the magnetic field increases. As the field becomes stronger the angle γ decreasesfigure.3.10. Note that the labelling of the sublattices is completely arbitrary. Using equation (3.6Zero Temperature Analysisequation.3.3.6) yields the following expression

$$\cos\gamma = \frac{(\frac{2H}{zJ} + 1)}{2} \tag{3.10}$$

From this equation, we note that it is only valid in the regime $0 < H \leq \frac{zJ}{2}$ and that at $H = \frac{zJ}{2}$ two spins on the triangle become completely aligned in the field direction with one spin still anti-aligned (Fig. 3.11When the magnetic field strength $H = \frac{zJ}{2}$, two spins on the triangle completely align with the field while one remains anti-aligned in a collinear statefigure.3.11). This configuration is called the collinear

Figure 3.11: When the magnetic field strength $H = \frac{zJ}{2}$, two spins on the triangle completely align with the field while one remains anti-aligned in a collinear state

phase or C-phase for short. The magnetization per site for this latter configuration is $m = \frac{1}{3}$. However, this state is highly degenerate. Two sublattices are anti-parallel and these two sublattices can be rigidly rotated to any direction without changing the energy as long as the third sublattice is parallel to the field. Hence the collinear state can be distorted into a planar state with zero energy cost. At finite temperatures, fluctuations may lead to an entropic selection process.

For fields in the range $\frac{zJ}{2} < H < \frac{3zJ}{2}$, the spins on the triangle will still assume a planar structure with two spins being aligned with each other and the third spin swinging up towards the field from the anti-aligned position forming an angle β with the field direction as shown in Fig. 3.12In this regime the spins deviate from the C-phase by the angles β and α with two spins remaining collinearfigure.3.12. The two aligned spins will no longer be oriented exactly with the field but will instead form an angle α with it instead.

Analytic expressions for these angles can be obtained by solving the vector equation (3.6Zero Temperature Analysisequation.3.3.6). As there are two angles to solve for we must solve this system for the parallel and perpendicular components of the

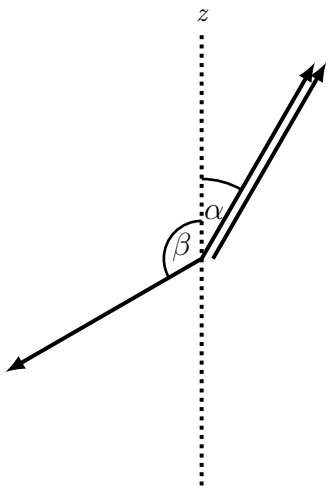

Figure 3.12: In this regime the spins deviate from the C-phase by the angles β and α with two spins remaining collinear

spins with respect to the field.

$$\begin{aligned} \cos\beta + 2\cos\alpha &= \frac{2H}{zJ} \\ \sin\beta + 2\sin\alpha &= 0 \end{aligned} \tag{3.11}$$

Solving for $\cos\beta$ and $\cos\alpha$ we find

$$\begin{aligned} \cos\alpha &= \frac{zJ\left[\left(\frac{2H}{zJ}\right)^2 + 3\right]}{8H} \\ \cos\beta &= \frac{zJ\left[\left(\frac{2H}{zJ}\right)^2 - 3\right]}{4H} \end{aligned} \tag{3.12}$$

The spins maintain this so-called V-phase until the magnetic field reaches $H = \frac{3zJ}{2}$. These results completely agree with our previous analysis of equation (3.6Zero Temperature Analysisequation.3.3.6) entering the paramagnetic state when the magnetic field reaches the saturation point. The spins are all collinear and pointing in the direction of the field for $H \geq \frac{3zJ}{2}$.

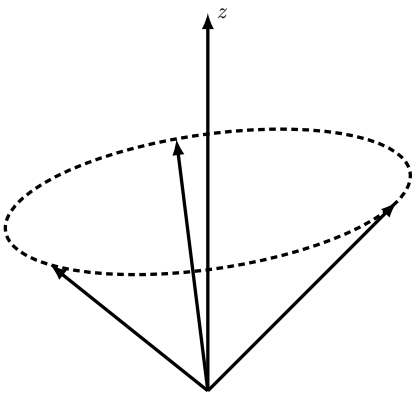

Figure 3.13: Umbrella state

In addition to these planar states, there are also non-planar states at zero temperature with the same energy. One simple example is the *umbrella* state where the 120° state at $H = 0$ simply closes up along the direction of $\vec{H}$ as shown in Fig. 3.13Umbrella statefigure.3.13. However, we shall see later that finite temperatures destabilize this state.

This general analysis can be applied to the lattices covered earlier. The 2-D triangular lattice has $z = 6$ and the 3-D stacked triangular has $z = 6$ in the plane and an additional two neighbours above and below. These latter neighbours do not enter into the analysis above except to add a constant term to the energy. The 2-D and 3-D kagome lattices have $z = 4$ and $z = 8$ respectively. The triangles in the different lattices are either edge-sharing or vertex-sharing, and the fact that they are composed of triangles with anti-ferromagnetic interactions between neighbours is all the information that is needed. The foregoing analysis applies to both cases.

3.4 Sublattice Switching

In all of the planar phases discussed above, the sublattice magnetizations $|\vec{m}_A|, |\vec{m}_B|$ and $|\vec{m}_C|$ are fully saturated at zero temperature. However, the FCC Kagome lattice

has a degeneracy of the planar states associated with sublattice switching. If we fix the direction of the spins on the A sublattice, then we can switch all of the B and C spins in a plane perpendicular to the x-axis with no change in energy or the net magnetization parallel to the field. However, the magnitude of the sublattice magnetizations that are switched are reduced. For example, in the V-phase, the magnitudes of the sublattice magnetizations are given by

$$\begin{aligned} |\vec{m}_A| &= 1 \\ |\vec{m}_B| = |\vec{m}_C| &= \sqrt{1 + 2x(x-1)(1-\cos(\alpha+\beta))} \end{aligned} \tag{3.13}$$

where α and β are the angles of the sublattices with the field direction and x is the fraction of planes in which switching occurs. These expressions remain valid in the C-phase if we choose $\alpha = 0$ and $\beta = \pi$. They are also valid in the Y-phase for $\beta = \pi$ and $\alpha = \gamma$.

In addition to sublattice switching, there is an additional degeneracy in the Y-phase. In this case one of the sublattices is anti-aligned with the field and the other two sublattices have the same component parallel to the field and opposite components perpendicular to the field. However, these two sublattices can be rigidly rotated by any angle about the field direction with no change in energy. In addition, these rotation angles can vary from plane to plane along one of the cartesian axes. This results in the z-components of the sublattice magnetizations remaining unchanged but the transverse components are reduced which leads to a decrease in the magnitude of the sublattice magnetizations on two of the sublattices. If the A sublattice is anti-aligned with the field and the B and C spins in a plane are rotated, then for planar states the rotation angle in each plane is either 0 or π. In this case the sublattice magnetizations at zero temperature are

$$\begin{aligned} |\vec{m}_A| &= 1 \\ |\vec{m}_B| = |\vec{m}_C| &= \sqrt{1 + 4x(x-1)\sin^2\gamma} \end{aligned} \tag{3.14}$$

where x is the fraction of planes in which the angle is π. We will discuss these

degeneracies further in Chapters 5 and 7.

Chapter 4

ORDER PARAMETERS/RESPONSE FUNCTIONS

In order to identify when the system makes a transition from one phase to another we define quantities called *order parameters* that measure the degree of order in a given phase. Order parameters usually have a finite value on one side of a transition and change abruptly or are equal to zero on the other, enabling us to detect the phase boundary for the transition being studied. In this thesis we will use slightly different order parameters for the two lattices being studied, due to the fact that the stacked triangular lattice is a Bravais lattice and the FCC Kagome lattice is not. We also use response functions which measure the response of a given system to an infinitesimal perturbation of the system.

4.1 Spin Stiffness

A useful response function is the spin stiffness which is a measure of the rigidity of the ordered phase with respect to a twist. It is the response to a gradient imposed on the spin ordering. Since there is an applied magnetic field in our spin system, there is an energy contribution due to the spins coupling with the field from the Zeeman term in our Hamiltonian. Therefore we perform a twists about the field direction. The Zeeman interaction will be constant and can be ignored when finding the difference between the energies of the twisted and non-twisted states. As in the previous chapter, we define the field direction to be in the $\hat{z}$ direction to simplify calculations.

We perform a twist about the field direction in which each spin in the lattice is rotated by an angle of $\theta_i = (\vec{r}_i \cdot \hat{u})\frac{\Theta}{L}$. Here $\vec{r}_i$ is the position vector of the spin at site

i in the lattice. This is equivalent to imposing a gradient $\hat{u}\frac{\Theta}{L}$ upon all spins in the lattice. Imposing this twist about the $\hat{z}$ direction is equivalent to left multiplying the Heisenberg spin vectors by the basic rotation matrix R_z for a rotation of theta about $\hat{z}$

$$R_z = \begin{bmatrix} \cos\theta_i & -\sin\theta_i & 0 \\ \sin\theta_i & \cos\theta_i & 0 \\ 0 & 0 & 1 \end{bmatrix} \tag{4.1}$$

Applying this rotation to the Spin-Hamiltonian (2.21Assumptions and Simplificationsequation.2.2.21 we find the following result

$$H' = -\sum_{<i,j>}^{N} J_{ij} S_i^T R_z^T(\theta_i) R_z(\theta_j) S_j - \sum_{i}^{N} \vec{h}^T R_z(\theta_i) \vec{S}_i \tag{4.2}$$

This expression can be simplified using the following properties of the rotation matrix

$$\begin{cases} R^T(\theta) = R(-\theta) \\ R(\beta)R(\alpha) = R(\beta+\alpha) \end{cases} \tag{4.3}$$

Using the fact that the z-direction is defined to be parallel to the field direction and that the z coordinate is unchanged under a rotation about the z-axis, we see that the Zeeman energy is unchanged yielding the following simplification of the Hamiltonian

$$H(\alpha) = -\sum_{<i,j>}^{N} J_{ij} S_i^T R_z(\theta_{ij}) S_j - \sum_{i}^{N} H S_i^z \tag{4.4}$$

where

$$\theta_{ij} = \theta_j - \theta_i = (\vec{r}_j - \vec{r}_i) \cdot \hat{u}\frac{\Theta}{L} = (\vec{r}_{ij} \cdot \hat{u})\alpha \tag{4.5}$$

The α term is the *gradient magnitude* and $\hat{u}$ is the direction of the gradient imposed on the lattice spins.

The *classical partition function* Z' for the twisted system is

$$Z' = Tre^{-\frac{H(\theta_{ij})}{k_B T}} \tag{4.6}$$

and the free energy pers site f' is

$$f' = \frac{F'}{N} = -\frac{k_B T}{N} \ln(Z') \tag{4.7}$$

The twisted free energy is the sum of the untwisted free energy f plus an energy modification term that varies quadratically with the gradient magnitude α

$$f' = f + \frac{1}{2}\rho_{\hat{z}}\alpha^2 \tag{4.8}$$

Therefore we define the *spin stiffness* $\rho_{\hat{z}}$ for a twist about the $\hat{z}$ direction as follows

$$\rho_{\hat{z}} = \frac{d^2 f'}{d\alpha^2}|_{\alpha=0} \tag{4.9}$$

where we evaluate the derivative at $\alpha = 0$ since we are considering the limit of a twist of infinitesimal strength with a given direction. Using the definition of f' in ($4.7 SpinStiffnessequation.4.1.7$) we can write the second derivative with respect to α as

$$\begin{aligned} \frac{d^2 f'}{d\alpha^2} &= \frac{k_B T}{N}\left[\frac{1}{Z'^2}\left(\frac{dZ'}{d\alpha}\right)^2 - \frac{1}{Z'}\frac{d^2 Z'}{d\alpha^2}\right] \\ &= \frac{1}{N}\left[\left\langle \frac{d^2 H'(\alpha}{d\alpha^2}\right\rangle_T - \frac{1}{k_B T}\left\langle\left(\frac{dH'(\alpha)}{d\alpha}\right)^2\right\rangle_T + \frac{1}{k_B T}\left(\left\langle\frac{dH'(\alpha)}{d\alpha}\right\rangle_T\right)^2\right] \end{aligned} \tag{4.10}$$

The angle brackets denote thermal averages. Since the Hamiltonian is even in α , $\frac{dH'(\alpha)}{d\alpha}$ will be odd in α and $\frac{d^2 H'(\alpha)}{d\alpha^2}$ will be even. Using these symmetries we note that the last term in ($4.10 SpinStiffnessequation.4.1.10$) will average to zero since the function is odd. Hence only the first two terms contribute to the spin stiffness in equilibrium.

$$\begin{aligned} \frac{dH'(\alpha)}{d\alpha} &= -\sum_{<i,j>} J_{ij}\vec{S}_i \frac{dR_z(\theta_{ij})}{d\alpha}\vec{S}_j \\ \frac{d^2 H'(\alpha)}{d\alpha^2} &= -\sum_{<i,j>} J_{ij}\vec{S}_i \frac{d^2 R_z(\theta_{ij})}{d\alpha^2}\vec{S}_j \end{aligned} \tag{4.11}$$

Evaluating the derivatives of our rotation matrices, we find

$$\left.\frac{dR_z(\theta_{ij})}{d\alpha}\right|_{\alpha=0} = (\vec{r}_{ij}\cdot\hat{u})\begin{bmatrix} -\sin\theta_{ij} & -\cos\theta_{ij} & 0 \\ \cos\theta_{ij} & -\sin\theta_{ij} & 0 \\ 0 & 0 & 0 \end{bmatrix}_{\theta_{ij}=0} = (\vec{r}_{ij}\cdot\hat{u})\begin{bmatrix} 0 & -1 & 0 \\ 1 & 0 & 0 \\ 0 & 0 & 0 \end{bmatrix} \quad (4.12)$$

$$\left.\frac{d^2R_z(\theta_{ij})}{d\alpha^2}\right|_{\alpha=0} = (\vec{r}_{ij}\cdot\hat{u})^2\begin{bmatrix} -\cos\theta_{ij} & \sin\theta_{ij} & 0 \\ -\sin\theta_{ij} & -\cos\theta_{ij} & 0 \\ 0 & 0 & 0 \end{bmatrix}_{\theta_{ij}=0} = (\vec{r}_{ij}\cdot\hat{u})^2\begin{bmatrix} -1 & 0 & 0 \\ 0 & -1 & 0 \\ 0 & 0 & 0 \end{bmatrix} \quad (4.13)$$

This yields our final expression for the spin stiffness for twists about the field direction

$$\rho_{\hat{z}} = \frac{1}{N}\Big\{\sum_{<i,j>}(\vec{r}_{ij}\cdot\hat{u})^2\langle S_i^xS_J^x+S_i^yS_j^y\rangle - \frac{1}{k_bT}\Big\langle\Big[\sum_{<i,j>}(\vec{r}_{ij}\cdot\hat{u})J_{ij}(S_i^xS_j^y-S_i^yS_j^x)\Big]^2\Big\rangle\Big\} \quad (4.14)$$

To illustrate why the spin stiffness will prove to be a useful indicator for transitions to different structured phases, we can easily make some predictions for the stiffness at zero temperature for the different phases assuming the planar sublattice geometries of the Kagome and stacked triangular lattice. We need only consider the first term in eqn.(4.14Spin Stiffnessequation.4.1.14) at zero temperature since it is easily shown that the second term is zero.

4.1.1 Stacked Triangular lattice

For the stacked triangular lattice the *gradient direction* can be chosen in any direction. We will consider the case $\hat{u}=\hat{z}$ which is perpendicular to the antiferromagnetic spin planes. Using the planar ground states described in the previous chapter we find that at zero temperature the spin stiffness is given by

$$\begin{aligned}\rho_{\hat{z}} &= \frac{2}{3}[1-(\frac{H+3}{6})^2] \quad \text{Y-phase} \\ &= 2[1-(\frac{H^2+27}{12H})^2] \quad \text{V-phase}\end{aligned} \quad (4.15)$$

Taking the limit $H \to 3$ for both the Y-phase and V-phase the stiffness goes to zero as they transition to the C-phase. In the V-phase the stiffness is also zero where it meets the paramagnetic phase at $H = 9$. Hence the spin stiffness will be useful in detecting transitions from the Y-phase to the UUD phase as well as from the V-phase to the paramagnetic phase.

4.1.2 Kagome Lattice

For the Kagome lattice we choose a gradient perpendicular to the $(1,1,1)$ Kagome planes. Using $\hat{u} = \frac{1}{\sqrt{3}}(1,1,1)$ we find the spin stiffness at zero temperature to be given by

$$\begin{aligned} \rho_{\hat{z}} &= \frac{2}{9}[1 - (\frac{H+4}{8})^2] \quad \text{Y-phase} \\ &= \frac{2}{3}[1 - (\frac{H}{16} + \frac{3}{H})^2] \text{ V-phase} \end{aligned} \tag{4.16}$$

In the limit $H \to 4$ the stiffness goes to zero as the C-phase is approached as in the case of the stacked triangular lattice. The spin stiffness helps pick up transitions to the UUD phase as well as the paramagnetic phase where it approaches zero at $H = 12$ in the V-phase.

4.2 Structure Factor and Correlation Length

The stacked triangular lattice is a Bravais lattice and has a reciprocal lattice corresponding to the Fourier Transform of the lattice coordinates. For a Bravais lattice there is one atom per unit cell. The sublattice spin configurations in the ground state can be described in terms of a single wavevector $\vec{Q}$ which has the values $\vec{Q} = (\pm\frac{4\pi}{3}, 0, 0)$ corresponding to the two chiralities in Fig.3.2A planar ground state for a single triangle in the absence of an applied field. a) 120° has positive chirality b) 240° has negative chiralityfigure.3.2. Consider the *Structure Factor* at wavevector $\vec{q}$ defined as follows

$$\mathcal{S}^{\alpha}(\vec{q}) = \frac{1}{N}\left\langle \left| \sum_{j}^{N} S_j^{\alpha} e^{-i\vec{q}\cdot\vec{r}_j} \right|^2 \right\rangle_T \tag{4.17}$$

where $\alpha = x, y, z$ are the cartesian components of the spins and the angled brackets denote the thermal average. We note that this is a vector equation and we define the components that are perpendicular and parallel to the applied field as follows

$$\begin{aligned} \mathcal{S}^{\parallel} &= \mathcal{S}^{z} \\ \mathcal{S}^{\perp} &= \mathcal{S}^{x} + \mathcal{S}^{y} \end{aligned} \tag{4.18}$$

The structure factor has a maximum in reciprocal space at the ordering wavevector $\vec{Q}$ which diverges at the ordering temperature. It has a Lorentzian form [22]

$$S(\vec{q}) \sim \frac{1}{(\vec{q} - \vec{Q})^2 + \xi^{-2}} \tag{4.19}$$

where ξ is the correlation length. We can obtain the correlation length ξ for sufficiently large systems(small q) as follows

$$\xi = \frac{1}{|\delta\vec{q}|}\sqrt{\frac{\mathcal{S}(\vec{Q})}{\mathcal{S}(\vec{Q} + \delta\vec{q})} - 1} \tag{4.20}$$

We can define both a parallel and perpendicular component $\xi_{\parallel}$, $\xi_{\perp}$ by using the relevant structure factors in this expression. However, we are restricted in our choices for $\delta\vec{q}$. Due to the periodic boundary conditions imposed on the system there is a discrete number of allowed wave vectors

$$\vec{q}_{n,m,l} = \left(\frac{n2\pi}{L_x}, \frac{m2\pi}{L_y}, \frac{l2\pi}{L_z}\right) \Big| \, n, m, l \in Z \tag{4.21}$$

In our case $L = L_x = L_y = L_z$ and we choose a $\delta\vec{q} = \left(\frac{2\pi}{L}, 0, 0\right)$, the smallest allowed displacement between two wave vectors on the reciprocal lattice. Both the structure factor and the correlation length can be used to detect the transitions and the correlation length will allow us to do some finite size scaling analysis.

While we cannot predict the value of the correlation length for the different phases, we can simplify the expression for the structure factor using the three sublattice structure of the triangular lattice. We first rewrite the structure factor at its ordering wavevector $\vec{Q}$ using *Euler's formula* for the complex exponential.

$$\mathcal{S}^{\alpha}(\vec{Q}) = \frac{1}{N}\Big\langle \Big[\Big(\sum_{j}^{N} S_j^{\alpha}\cos(-\vec{Q}\cdot\vec{r}_j)\Big)^2 + \Big(\sum_{j}^{N} S_j^{\alpha}\sin(-\vec{Q}\cdot\vec{r}_j)\Big)^2\Big]\Big\rangle_T \tag{4.22}$$

Next we simplify the trigonometric functions using the periodic properties of the lattice. They only take on three distinct arguments

$$(-\vec{Q}\cdot\vec{r}_j) = \begin{cases} -\frac{2\pi}{3} \\ -\frac{4\pi}{3} \\ -2\pi \end{cases} \tag{4.23}$$

representing the values on the three sublattices. Using a site on the C sublattice as origin, the structure factor becomes

$$\begin{aligned} \mathcal{S}^{\alpha}(\vec{Q}) &= \frac{1}{N}\Big\langle \Big[\frac{N}{3}\Big(\frac{2m_C^{\alpha} - m_B^{\alpha} - m_A^{\alpha}}{2}\Big)\Big]^2 + \Big[\frac{N}{3}\frac{\sqrt{3}}{2}\Big(m_A^{\alpha} - m_B^{\alpha}\Big)\Big]^2\Big\rangle_T \\ &= \frac{N}{9}\Big\langle \Big(\frac{2m_C^{\alpha} - m_B^{\alpha} - m_A^{\alpha}}{2}\Big)^2 + \Big(\frac{\sqrt{3}(m_A^{\alpha} - m_B^{\alpha})}{2}\Big)^2\Big\rangle_T \\ &= \frac{N}{9}\Big\langle \psi_1^2 + \psi_2^2\Big\rangle_T \\ &= \frac{N}{9}\Big\langle \Psi^2\Big\rangle_T \end{aligned} \tag{4.24}$$

where $m_A^{\alpha}, m_B^{\alpha}$ and m_C^{α} are the sublattice magnetization components and

$$\begin{aligned} \psi_1^{\alpha} &= \Big(\frac{2m_C^{\alpha} - m_B^{\alpha} - m_A^{\alpha}}{2}\Big) \\ \psi_2^{\alpha} &= \Big(\frac{\sqrt{3}(m_A^{\alpha} - m_B^{\alpha})}{2}\Big) \\ (\Psi^{\alpha})^2 &= (\psi_1^{\alpha})^2 + (\psi_2^{\alpha})^2 \end{aligned} \tag{4.25}$$

The ψ functions have the advantage that they vanish in the paramagnetic phase whereas the sublattice magnetizations do not vanish in a field.

The FCC Kagome lattice is not a Bravais lattice but has 3 atoms in the unit cell and the ordering cannot be described in terms of a single wavevector. However, three sublattice structure allows us to use the same definitions of the ψ functions.

We now define the parallel and perpendicular components of this order parameter as such

$$\Psi_z^2 = (\psi_1^z)^2 + (\psi_2^z)^2 \tag{4.26}$$

$$\Psi_\perp^2 = (\psi_1^x)^2 + (\psi_2^x)^2 + (\psi_1^y)^2 + (\psi_2^y)^2 \tag{4.27}$$

The perpendicular and parallel order parameter components in terms of the spherical coordinates of the sublattices are

$$\begin{aligned}\Psi_z^2 = {} & \cos^2(\theta_A) + \cos^2(\theta_B) + \cos^2(\theta_C) - \cos(\theta_A)\cos(\theta_B) \\ & - \cos(\theta_B)\cos(\theta_C) - \cos(\theta_C)\cos(\theta_A)\end{aligned} \tag{4.28}$$

$$\begin{aligned}\Psi_\perp^2 = {} & \sin^2(\theta_A) + \sin^2(\theta_B) + \sin^2(\theta_C) - \sin(\theta_A)\sin(\theta_B)\cos(\phi_A - \phi_B) \\ & - \sin(\theta_B)\sin(\theta_C)\cos(\phi_B - \phi_C) - \sin(\theta_C)\sin(\theta_A)\cos(\phi_C - \phi_A)\end{aligned} \tag{4.29}$$

We can now easily make predictions for for the ψ functions at zero temperature in each phase that we expect to see

$$\Psi_z^2 = \begin{cases} \Big(\cos\gamma + 1\Big)^2 & \text{Y-phase} \\ 4 & \text{C-phase} \\ \Big(\cos\alpha - \cos\beta\Big)^2 & \text{V-phase} \\ 0 & \text{paramagnetic phase} \end{cases} \tag{4.30}$$

$$\Psi_{\perp}^{2} = \begin{cases} 3\sin^{2}\gamma & \text{Y-phase} \\ 0 & \text{C-phase} \\ \Big(\sin\alpha + \sin\beta\Big)^{2} & \text{V-phase} \\ 0 & \text{paramagnetic phase} \end{cases} \tag{4.31}$$

We can see that the perpendicular component will detect transitions from the Y-phase to the C-phase, and transitions from the V-phase to the paramagnetic phase. However, it will not be able to pick out the transition from the C-phase to the paramagnetic phase since it is zero in both. On the other hand, the parallel component will allow us to detect the transition from the C-phase to the paramagnetic phase as it is finite valued in the C-phase.

These order parameters will be used to find other quantities that are calculated using the equilibrium values of Ψ. We define the thermal average as $\mathcal{O}$, the ordering susceptibility χ, and a temperature-dependent structure factor $\mathcal{S}$ as such.

$$\begin{aligned} \mathcal{O} &= \langle|\Psi|\rangle \\ \chi &= N\frac{\langle\Psi^{2}\rangle - \langle|\Psi|\rangle^{2}}{T} \\ \mathcal{S} &= N\frac{\langle\Psi^{2}\rangle}{T} \end{aligned} \tag{4.32}$$

These response functions will provide useful information as well on the nature of the transitiom. As we have a parallel and perpendicular component to the order parameter Ψ there will also be a parallel and perpendicular component to these quantities.

4.3 Average Energy and Heat Capacity

In addition we also calculate the average energy per site

$$\frac{\langle E\rangle_T}{N} = \frac{1}{N}\Big\langle - J \sum_{<i,j>} \vec{S}_i \cdot \vec{S}_j - H \sum_i S_i^z \Big\rangle_T \tag{4.33}$$

and the specific heat

$$\frac{\langle C_v\rangle_T}{N} = \frac{1}{N k_B T^2}\Big\langle (E - \langle E\rangle_T)^2 \Big\rangle_T \tag{4.34}$$

4.4 Sublattice Switching

In the case of the Kagome lattice, sublattice switching can occur as decribed in section 3.4 of the previous chapter. The energy, the stiffness, and the total M_z are not affected by the switching. However, the individual sublattice magnetizations are changed. Hence the order parameters Ψ_z and $\Psi_\perp$ are also affected.

In the V-phase, the order parameters take the values

$$\begin{aligned} \Psi_z^2 &= (1 - 3x + 3x^2)(cos\alpha - cos\beta)^2 \\ \Psi_\perp^2 &= (1 - 3x + 3x^2)(sin\alpha + sin\beta)^2 \end{aligned} \tag{4.35}$$

where x is the fraction of planes in which switching occurs and α, β are defined in Fig. 3.13. In the Y-phase, these quantities are given by

$$\begin{aligned} \Psi_z^2 &= (1 - 3x + 3x^2)(1 + cos\gamma)^2 \\ \Psi_\perp^2 &= 3(1 - x + x^2)sin^2\gamma \end{aligned} \tag{4.36}$$

where γ is defined as in Fig.3.11.

In addition to the above which involves switches of two sublattices with unequal z components, we can also have rotations of sublattices with equal z components about the field direction in the Y-phase. In this latter case, Ψ_z is unaffected but $\Psi_\perp$ will depend on the fraction of planes in which rotations occur. For planar states the rotations are restricted to be by zero or π and the order parameters have the following

values

$$\begin{aligned} \Psi_z^2 &= (1 + cos\gamma)^2 \\ \Psi_\perp^2 &= 3(1 - 2x)^2 sin^2\gamma \end{aligned} \tag{4.37}$$

We will discuss these effects further in chapter 7.

Chapter 5

MONTE CARLO AND FINITE SIZE ANALYSIS

Many of quantities defined in the previous chapter require thermal averages to be calculated. However, the system has many interacting spins and it is not possible to find analytic expressions. Hence we need to calculate these averages numerically and a convenient way to do so is to simulate the system on a computer with Monte Carlo methods using Boltzmann statistics. In the case of classical Heisenberg spins which have unit length, the heat bath method provides a direct procedure for obtaining spin configurations which satisfy the Boltzmann distribution. We will first consider a single spin in an applied field to illustrate the approach.

5.1 Single Spin System

As a simple example consider a single spin in a magnetic field $\vec{H}$ such that the spin forms an angle θ with the field. The energy of this system arises purely from the Zeeman interaction of the spin with the field and the Hamiltonian has the form

$$\mathcal{H} = -\vec{H} \cdot \vec{S} = -|H| \cos\theta \tag{5.1}$$

We define our coordinate system such that the z-direction is parallel with the field $\vec{H}$ and the energy only depends on the polar angle θ and is independent of ϕ. At a finite T, we can define the probability to observe the spin at an angle θ with the field as

$$P(\theta) = Ce^{-\frac{\mathcal{H}}{k_B T}} = Ce^{\frac{H\cos\theta}{k_B T}} \tag{5.2}$$

This is a Boltzmann distribution for the energy with C being the normalization constant as probability distributions must be normalized to unity. We can find C by integrating $P(\theta)$ over the surface of the unit sphere and setting the integral to unity.

$$\begin{aligned} 1 &= \int_0^{2\pi} d\phi \int_0^{\pi} (\sin\theta d\theta) P(\theta) \\ &= \frac{k_B T}{h} 4\pi \sinh\left(\frac{H}{k_B T}\right) \\ \Rightarrow C &= \frac{H}{k_B T} \frac{1}{4\pi \sinh\left(\frac{H}{k_B T}\right)} \qquad (5.3) \\ \Rightarrow P(\theta) &= \frac{H}{k_B T} \frac{1}{4\pi \sinh\left(\frac{H}{k_B T}\right)} e^{\frac{H\cos\theta}{k_B T}} \qquad (5.4) \end{aligned}$$

To check that this distribution makes sense we take the extreme limits of T for the probability distribution.

$$\begin{cases} \frac{k_B T}{H} \to 0 & P(\theta) \text{ is unity at } \theta = 0 \text{ and 0 for } \theta \neq 0 \\ & \text{no thermal fluctuations at zero temperature} \\ & \text{the spin is in perfect alignment with the field to minimize its energy} \\ \frac{k_B T}{h} \to \infty & p(\theta) \to \frac{1}{4\pi} \\ & \text{therefore the spin is distributed uniformly on the unit sphere} \end{cases} \qquad (5.5)$$

Using this distribution we can obtain an expression for $\langle E \rangle_T = -H \langle \cos\theta \rangle_T$

$$\begin{aligned} \langle E \rangle_T &= \int_0^{2\pi} d\phi \int_0^{\pi} (\sin\theta d\theta)(-H cos\theta) P(\theta) \\ &= -H\Big[\coth\left(\frac{H}{k_B T}\right) - \frac{k_b T}{H}\Big] \qquad (5.6) \\ &= -H\langle \cos\theta \rangle_T \end{aligned}$$

Once again we can take the limits of T to see if the energy behaves as expected at the extrema.

$$\begin{cases} \frac{k_b T}{H} \to 0 & \langle \cos\theta \rangle_T \to 1 \, \text{spin alligned with field} \\ \frac{k_b T}{H} \to \infty & \langle \cos\theta \rangle_T \to 0 \, \text{spin randomly aligned} \end{cases} \tag{5.7}$$

5.1.1 Generating the Boltzmann distribution for a single spin

We would now like to numerically generate the probability $P(\theta)$ at a fixed temperature and field. Most programming languages/compilers have built in random number generators that distribute the random variable uniformly on the range [0..1]. We can choose a random variable $r \in [0, 1]$ by integrating a normalized probability distribution $P(x)$ from it's lower domain limit to a point x.

$$r = \int_{-\infty}^{x} P(x')dx' \tag{5.8}$$

$$\text{where} \quad \frac{dr}{dx} = P(x) \tag{5.9}$$

We can easily see that r is in the domain described as the probability when integrated over the entire domain is equal to unity. As probabilities can never be negative, the lower bound for this integral must be zero. If we invert this expression for x, we will be able to use a uniformly distributed random variable and transform it into a random variable that is generated according to $P(x)$.

In the case of a single spin, the integral must be over a unit sphere and we must randomly generate ϕ and θ. As our distribution did not explicitly depend on ϕ we assume that it is distributed uniformly over its domain. Therefore we can decompose our previous distribution into the product of two distributions.

$$P(\phi,\theta) = \frac{H}{k_BT}\frac{1}{4\pi\sinh\left(\frac{H}{k_BT}\right)}e^{\frac{H\cos\theta}{k_BT}}$$
$$= P(\phi)P(\theta) \tag{5.10}$$
$$P(\phi) = \frac{1}{2\pi} \tag{5.11}$$
$$P(\theta) = \frac{H}{k_BT}\frac{1}{2\sinh\left(\frac{H}{k_BT}\right)}e^{\frac{H\cos\theta}{k_BT}} \tag{5.12}$$

If we now invert equation (5.8$Generating the Boltzmann distribution for a single spin equation$.5.1.8) for $P(\phi)$

$$r_1 = \int_0^x \frac{1}{2\pi}\,d\phi$$
$$= \frac{1}{2\pi}x$$
$$\Rightarrow x = 2\pi r_1 \tag{5.13}$$

As we can see, this function will take in a random number r_1 distributed uniformly on $[0,1)$ and will output $x \in [0,2\pi)$ as desired. We now look at the more complicated integral involving $P(\theta)$.

$$r_2 = \int_0^x (\sin\theta\,d\theta)\frac{H}{k_BT}\frac{1}{2\sinh\left(\frac{H}{k_BT}\right)}e^{\frac{H\cos\theta}{k_BT}}$$
$$= \frac{e^{\frac{H}{k_BT}} - e^{\frac{H\cos(x)}{k_BT}}}{2\sinh\left(\frac{H}{k_BT}\right)}$$
$$\Rightarrow \cos(x) = 1 + \frac{k_BT}{H}\ln\left(e^{-\frac{2H}{k_BT}}r_2 + (1-r_2)\right) \tag{5.14}$$

We leave the left hand side in terms of $\cos(x)$, as we will be required to find this quantity anyways and there is no need to invert the cosine function. We note that $\cos(x) \in [-1,1]$ as required and is completely generated using our uniformly distributed variable r_2, given a specified temperature and field strength.

Since $\sin\theta = \sqrt{1-\cos^2\theta}$, we can use these randomly generated values of ϕ and $\cos\theta$ to define a direction of the spin using spherical coordinates.

$$\vec{S} = \big(\sin\theta\cos\phi, \sin\theta\sin\phi, \cos\theta\big) \tag{5.15}$$

Repeating this procedure many times on a computer we can sample all important directions of the spin for a given T and H, and average to calculate thermal averages for any variable or function we wish. This example is rather trivial since there are closed form solutions for almost anything we would like to calculate in the single spin system. However this example establishes the groundwork and general technique that will be employed in the many interacting spin system.

5.2 Many Interacting Spins

We now consider the problem of generating the Boltzmann distribution for multiple interacting spins on a lattice. Consider the many spin system with the Hamiltonian as defined by equation (2.21$Assumptions and Simplification sequation$.2.2.21) in Chapter 2. We define our global coordinate system such that the z-direction is parallel with the applied field direction.

$$\mathcal{H}_{spin} = -\sum_{<i,j>}^{N} J_{ij} S_i \cdot S_j - H\sum_{i}^{N} S^z \tag{5.16}$$

If we look at a single spin on site i, we can define a *local effective field* that is the vector sum of the exchange interactions with its nearest neighbours and the Zeeman interaction with the field.

$$\vec{h}_{local\,i} = \sum_{j} J_{ij}\vec{S}_j + \vec{H} \tag{5.17}$$

We also consider a local coordinate system such that the local z'-coordinate is parallel with the local field direction $\vec{h}_{local,i}$. This allows us to define the local Hamiltonian

on site i as

$$\mathcal{H}_{local\,i} = -\vec{h} \cdot \vec{S}_i = -|h_{local\,i}| \cos\theta_{local\,i} \tag{5.18}$$

where $\theta_{local\,i}$ is the angle between the spin and the local field. We have now effectively transformed the problem for the spin on site i into the single spin in a field problem, as we have accounted for all interactions acting on $\vec{S}_i$. Therefore we can write down the generating functions (5.14$GeneratingtheBoltzmanndistributionforasinglespinequation$.5.1.14) and (5.13$GeneratingtheBoltzmanndistributionforasinglespinequation$.5.1.13) for $\phi_{local\,i}$ and $\cos\theta_{local\,i}$ that we defined for the single spin system to generate a new direction for the spin on lattice site i.

$$\phi_{local\,i} = 2\pi r_1 \tag{5.19}$$

$$\cos(\theta_{local\,i}) = 1 + \frac{k_B T}{h_{local\,i}} \ln\left(e^{-\frac{2h_{local\,i}}{k_B T}} r_2 + (1 - r_2)\right) \tag{5.20}$$

where r_1 and r_2 are uniformly distributed random variables on $[0, 1)$ as per the single spin case. The new value of the spin $\vec{S}_i$ becomes using these variables

$$\vec{S}_{local\,i} = \left(\sin\theta_{local\,i}\cos\phi_{local\,i}, \sin\theta_{local\,i}\sin\phi_{local\,i}, \cos\theta_{local\,i}\right) \tag{5.21}$$

However, we now must rotate the spin back into the global coordinate system since $\vec{S}_{local\,i}$ is only defined in the local coordinate system determined by the local field. The angles of rotation are obtained from the local field direction

$$\begin{aligned}
\cos\Theta_i &= \frac{h^z_{local\,i}}{|h_{local\,i}|} \\
\sin\Theta_i &= \frac{\sqrt{h^{x\,2}_{local\,i} + h^{y\,2}_{local\,i}}}{|h_{local\,i}|} \\
\cos\Phi_i &= \frac{h^x_{local\,i}}{|h_{local\,i}|\sin\Theta} \\
\sin\Phi_i &= \frac{h^y_{local\,i}}{|h_{local\,i}|\sin\Theta}
\end{aligned} \tag{5.22}$$

We can perform an inverse rotation on the local spin components to the global coordinate system

$$
\begin{aligned}
S_i^x &= \cos\Phi_i\Big(\cos\Theta_i S_{local\,i}^{x'} + \sin\Theta_i S_{local\,i}^{z'}\Big) - \sin\Phi_i S_{local\,i}^{y'} \\
S_i^y &= \sin\Phi_i\Big(\cos\Theta_i S_{local\,i}^{x'} + \sin\Theta_i S_{local\,i}^{z'}\Big) + \cos\Phi_i S_{local\,i}^{y'} \\
S_i^z &= \cos\Theta_i S_{local\,i}^{z'} - \sin\Theta_i S_{local\,i}^{x'}
\end{aligned}
\tag{5.23}
$$

We now have a spin that is distributed according to the Boltzmann statistics for an interacting system of many spins in the global coordinate system. This was generated from two uniformly distibuted variables r_1 and r_2. We can do this for every spin on the lattice. We impose periodic boundary condition and the surface effects can be ignored.

This type of random number generation for non-uniform distributions is called the *Heat Bath Method*. It is useful to note that an initial seed must be set before the first Monte Carlo step for the spins of the entire lattice, as the spin update requires the spin of nearest neighbours be set already. This can be a random seed or curated to an initial configuration of your choosing. For the work done in this thesis a random seed was used prior to performing the first Monte Carlo step. Updating all of the spins in the lattice defines one Monte Carlo step. The transformation done on the set of spins on the lattice forms a Markov Chain that will sample equilibrium states for a given field and temperature. Using this method we will be able to extract thermal averages of order parameters and response functions at different values of T and H.

It is useful to note that all quantities sampled from the Monte Carlo simulation will be non-dynamic and therefore the static equilibrium quantities.

5.3 Phase transitions

A system of infinite size $L \to \infty$ can undergo a phase transition from one phase to another at particular values of T and H. The transition can be discontinuous accom-

panied by phase coexistence or continuous with a unique phase at the critical point. These transitions are called phase transitions of first and second order respectively. The transitions can be described in terms of order parameters and symmetry.

5.3.1 Continuous phase transitions : critical exponents, scaling and universality

A continuous (second order) phase transition is characterized by a singularity in the free energy with singular behaviour of its second derivatives. The order parameter changes from zero to a non-zero value at the critical point in a continuous way which is characterized by a nonanalytic power law behaviour and is described by a critical exponent. Ihe distance from the critical point in magnetic systems can be described by reduced variables such as $t = \frac{T-T_c}{T_c}$ and $h = \frac{H-H_c}{H_c}$ where T_c and H_c denote the critical temperature and critical field. The definition of various critical point exponents[23] in the vicinity of the critical point for zero applied field is summarized as follows:

Susceptibility	$\chi \sim t^{-\gamma}$	$t > 0$
Specific heat	$C_V \sim t^{-\alpha}$	$t > 0$
Order parameter	$\mathcal{O} \sim (-t)^{\beta}$	$t < 0$
Correlation length	$\xi \sim t^{-\nu}$	$t > 0$
Correlation function	$G(q) \sim q^{-2+\eta}$	$t = 0$
Stiffness	$\rho \sim (-t)^{(d-2)\nu}$	$t < 0$

The critical exponents $\alpha, \beta, \gamma, \nu$, and η are not all independent but are related by scaling relations[23]:

$$\alpha + 2\beta + \gamma = 2 \tag{5.24}$$
$$\gamma = (2 - \eta)\nu$$
$$\beta = \frac{1}{2}(d - 2 + \eta)\nu$$
$$d\nu = \gamma + 2\beta$$

The last two scaling relations explicitly involve the spatial dimension d and are called hyperscaling relations. Hence there are only two independent exponents.

The universality hypothesis states that the critical exponent values depend only on the dimensionality d of the physical system, the symmetry describing the order parameter and whether the interactions are short or long ranged.

5.4 Finite size scaling

A continuous phase transition is characterized by a singular behaviour of the free energy and related quantities when the system has an infinite number of particles, i.e. in the thermodynamic limit. However, in numerical simulations, one deals with systems of finite size. In these cases, mathematical singularities are modified and become regular functions and the singularities of the infinite system become rounded and shifted in the finite system. When interpreting Monte Carlo simulation results in the study of phase transitions, the most important task is to extrapolate the data obtained for finite systems to the thermodynamic limit. Such extrapolations are possible by using Finite Size Scaling theory (FSS) [24, 25, 26].

FSS was first introduced in the early seventies by Fisher [24, 25], Kadanoff [27] and others as a phenomenological theory but was later justified by a theoretical approach called the 'Renormalization Group'. Close to a critical point the distance over which microscopic order parameter fluctuations are significantly correlated is called a correlation length. The finite size scaling approach assumes that the only significant

characteristic length in the system is correlation length. The finite size effects depend upon the ratio of the linear dimension of the system to the correlation length L/ξ.

5.4.1 Finite Size Scaling at Second Order Transitions

At a second order transition, the free energy density $f(T,h)$ for an infinite system has a singular part that can be written in the form

$$\beta f(T,h) \sim t^{2-\alpha} Y(h/t^{\Delta}) \tag{5.25}$$

where t is the reduced temperature defined above. The so called gap exponent Δ is related to α and γ by $\Delta = \frac{1}{2}(2-\alpha+\gamma)$ and the scaling function Y is a universal function of a single argument. In an infinite system, the correlation length diverges with the power law form $\xi \sim |t|^{-\nu}$ where ν is the correlation length critical exponent. Hence the above scaling form can be rewritten as

$$\beta f(T,h) \sim \xi^{(\alpha-2)/\nu} Y(h\xi^{\Delta/\nu}) \tag{5.26}$$

In a finite size system, the correlation length is limited by the system size L and the corresponding free energy density $f_L(T,h)$ is assumed to also depend on the ratio L/ξ with the scaling form

$$\beta f_L(T,h) \sim L^{(\alpha-2)/\nu} Y(L/\xi, hL^{\Delta/\nu}) \tag{5.27}$$

The scaling relations for the order paramter $\mathcal{O}$, susceptibility χ, specific heat C_V and the stiffness ρ are obtained from (5.27Finite Size Scaling at Second Order Transitionsequation.5.4.27) by taking derivatives with respect to t and h

$$\begin{aligned}
\mathcal{O} &= L^{-\beta/\nu} f_{\mathcal{O}}(tL^{1/\nu}) \\
\chi &= L^{\gamma/\nu} f_{\chi}(tL^{1/\nu}) \\
C_V &= L^{\alpha/\nu} f_{C_V}(tL^{1/\nu}) \\
\rho &= L^{2-d} f_{\rho}(tL^{1/\nu}) \\
\xi &= L f_{\xi}(tL^{1/\nu})
\end{aligned} \tag{5.28}$$

where the magnetic field h has been set to zero and each quantity has its own universal scaling function with a single argument. At the critical point the scaling functions become constant and the prefactors describe the size dependence of the various quantities

$$\begin{aligned} \mathcal{O} &\propto L^{-\beta/\nu} \\ \chi &\propto L^{\gamma/\nu} \\ C_V &\propto L^{\alpha/\nu} \\ \rho &\propto L^{2-d} \\ \xi &\propto L \end{aligned} \tag{5.29}$$

In the limit where $L \to \infty$, the arguments of the scaling functions become large and vary as a power of the argument which exactly cancels the L dependence of the prefactor in each case. For example, the scaling function for the stiffness behaves as

$$\rho \sim L^{2-d}(tL^{1/\nu})^{(d-2)\nu} \sim t^{(d-2)\nu} \tag{5.30}$$

These relations can be used to find ratios of the critical exponents, or in the case of the spin stiffness, the exponent ν directly. Once this is done, the scaling functions can be determined by collapsing the data for several different sizes onto to a universal curve.

Chapter 6

THE STACKED TRIANGULAR LATTICE IN AN APPLIED FIELD

Both the Heisenberg and XY stacked triangular antiferromagnets are commonly referred to as the STA model. There are several experimental realizations of the stacked triangular geometry in which the exchange interactions are antiferromagnetic [1, 28, 29]. Examples include the ABX_3 type compounds where A is an element such as Cs or Rb, B is a magnetic ion such as Mn, Cu, Ni or Co, and X is a halogen such as Cl, Br or I. Another group that has been studied is the vanadium dihalides which include VCl_2 and VBr_2 as examples. Magnetic neutron scattering and specific heat measurements on these systems revealed finite temperature phase transitions which appeared to be continuous. The measured critical exponents exhibited scaling laws and the values seemed to support the prediction of a new universality class. Kawamura and Miyashita[7] have used Monte Carlo methods to study the Heisenberg antiferromagnet in a field on the two dimensional triangular lattice. They obtained a phase diagram in the $H-T$ plane which indicated three ordered phases but they did not study the critical behaviour. Seabra et. al[9] have recently carried out a more detailed study of the two dimensional case but we are not aware of any studies of the three dimensional Heisenberg stacked triangular lattice in a field. However, Plumer et. al[6] have used Monte Carlo methods to study the XY model in a field. In the following sections we describe our methods of calculations and results. We have used the heat bath method described in Chapter 5 to study the phase diagram in the $H-T$ plane. For the results presented in this chapter and the next we express both T and

H in units of the near neighbour coupling J. In the next section we first consider the low temperature behaviour as a function of the applied field to compare with the predictions in Chapters 3 and 4. All Monte Carlo simulations in this chapter used 10^5 steps, disregarding the initial 10^4 to reduce transients in the data. A random initial seed was used as well.

6.1 Low Temperature Analysis

In section 3.3 we outlined the stable phases at zero temperature as a function of the applied field. Both planar and nonplanar configurations are degenerate but it has been shown that for the XY model, at finite temperatures, the planar states have lower free energy[2, 3] and it is believed that the same conclusion applies to Heisenberg systems. We have used the heat bath Monte Carlo method described in section 5.2 to perform a sweep across all the field values at a fixed temperature of $T = 0.01$ to verify our zero temperature prediction for the different order parameters and magnetizations. Unfortunately simulations cannot be run at $T = 0$ exactly as the Heat Bath method involves division by temperature in the algorithm and therefore the simulation must be done near zero. We assume an applied field in the z-direction.

The z-component of the magnetization per site, and the sublattice magnetizations per site are shown in Fig. 6.1The total z-magnetization and z-sublattice magnetizations (symbols) compared to the predicted values (solid lines) near zero temperaturefigure.6.1 as a function of the field strength and they indicate that planar states are indeed favoured at finite T in agreement with the predicted values. One can see that the predictions seem to be perfectly superimposed on the computed values with only minor discrepencies at low field strength. This can be explained due to the fact that in this regime, the Zeeman energy is competing with the exchange energy. In zero field, the spin plane can have any orientation in spin space but in finite fields the plane normal orients perpendicular to the field direction. This competition at low fields

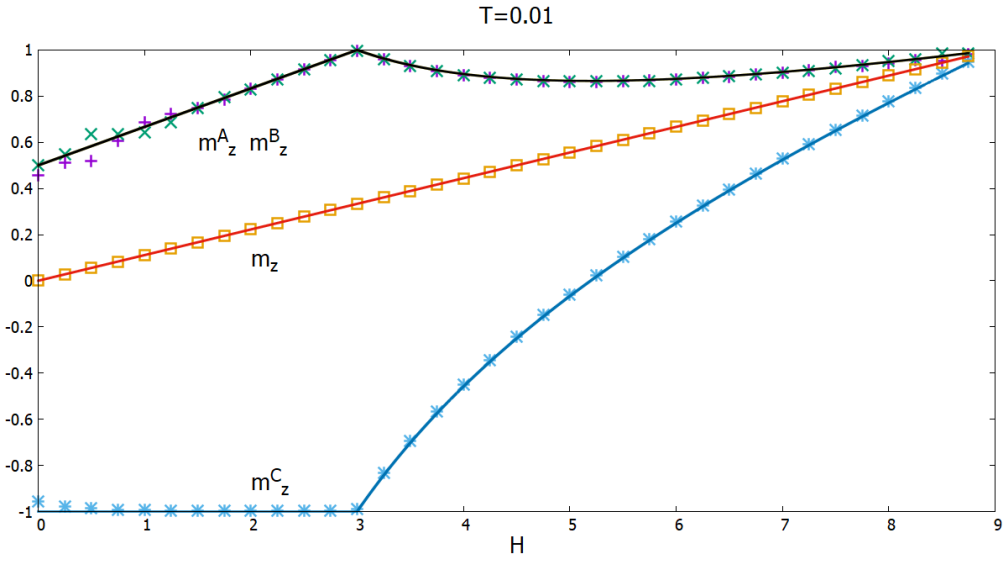

Figure 6.1: The total z-magnetization and z-sublattice magnetizations (symbols) compared to the predicted values (solid lines) near zero temperature.

results in the normal direction not being completely perpendicular to the field.

The computed values of the order parameters Ψ_z and $\Psi_\perp$ are plotted as a function of the field strength in Figs. 6.2The $\Psi_\perp$ order parameters(symbols) compared to the predicted values(solid lines) near zero temperaturefigure.6.2 and 6.3The Ψ_z order parameters(symbols) compared to the predicted values(solid lines) near zero temperaturefigure.6.3 along with the predicted zero temperature values and we see that our predictions fit perfectly on the curve drawn by our computed results, verifying our predictions for the behaviour of the order parameters. Similarly we observe in Fig. 6.4Monte Carlo results for the spin stiffness ρ_z (symbols) compared to the predicted values (solid lines)figure.6.4 the same qualitative features as $\Psi_\perp$ when plotting the spin stiffness ρ_z as a function of the field strength, due to the fact that both quantities are zero in the collinear and paramagnetic phases. These low T results agree with our zero temperature analysis confirming that the Monte Carlo simulation is working correctly in the low/zero temperature regime and indicate that the planar

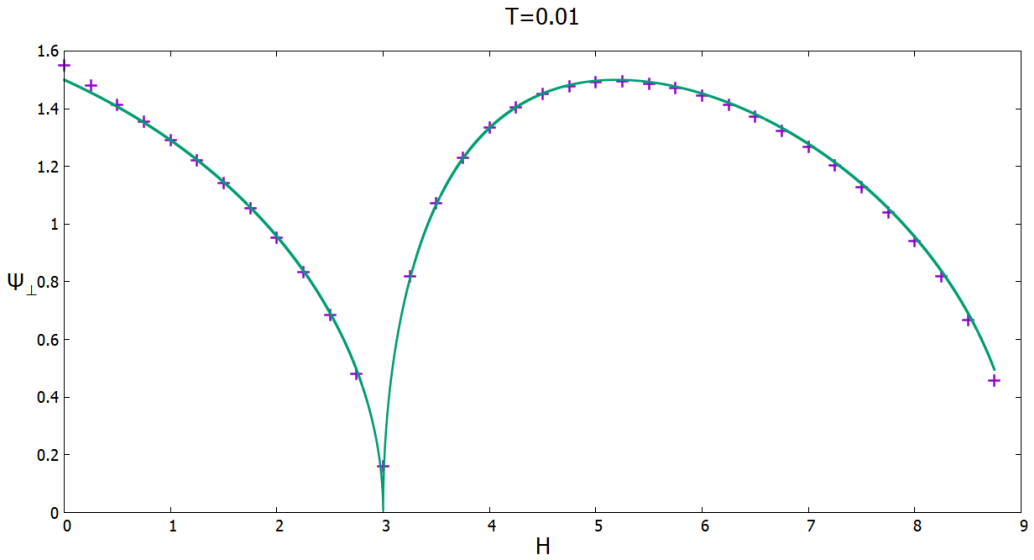

Figure 6.2: The $\Psi_{\perp}$ order parameters(symbols) compared to the predicted values(solid lines) near zero temperature.

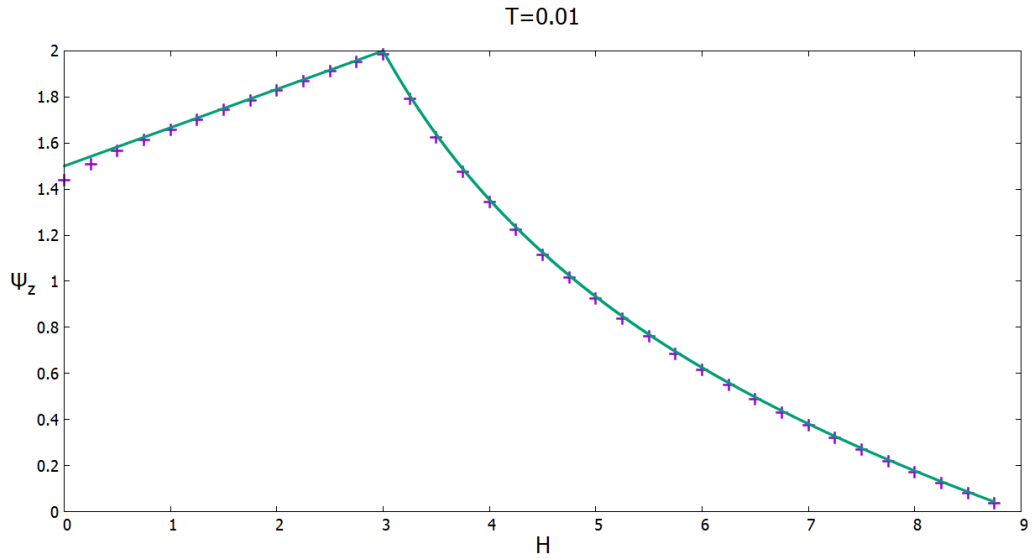

Figure 6.3: The Ψ_z order parameters(symbols) compared to the predicted values(solid lines) near zero temperature.

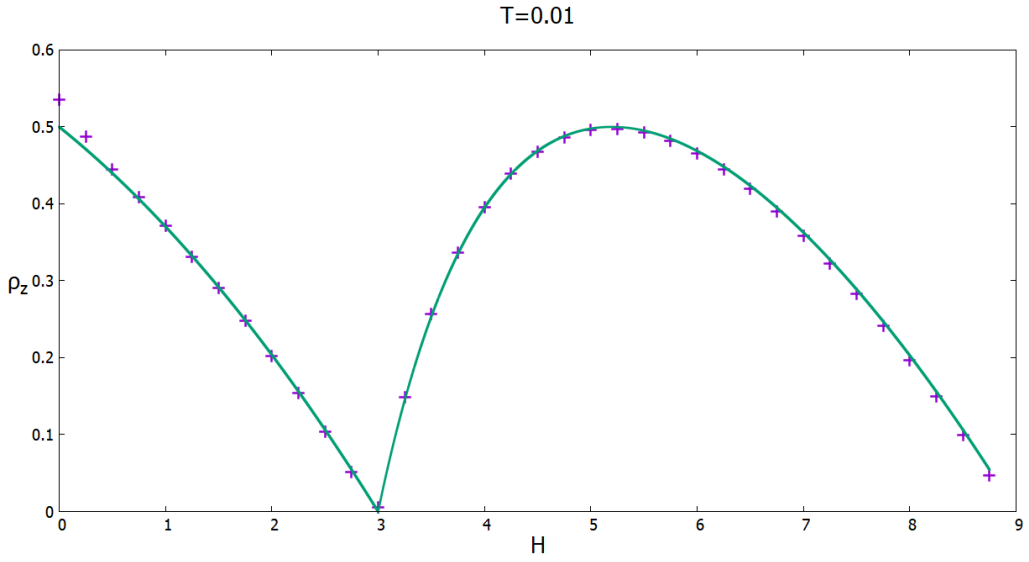

Figure 6.4: Monte Carlo results for the spin stiffness ρ_z (symbols) compared to the predicted values (solid lines).

states are energetically favoured at low but finite T.

6.2 Fixed Field Analysis

With the behaviour of the order parameters matching predictions at low/zero temperature, Monte Carlo simulations were then performed at fixed field strength while varying temperature. This was to verify whether the order parameters behave as expected in the different phase configurations. Fixing the field at a value between $3.0 < H < 9.0$ and varying the temperature, the results obtained from the Monte Carlo runs are shown in Figs. 6.5The spin stiffness ρ_z at $H = 5$ vs. Tfigure.6.5, 6.6The order parameters Ψ_z, $\Psi_\perp$ at $H = 5$ vs. Tfigure.6.6 and 6.7Total m_z and z-sublattice magnetizations at $H = 5$ vs. Tfigure.6.7 for $H = 5$.

Using the zero temperature analysis, the system is expected to be in the V-phase near zero temperature. The order parameters Ψ_z, $\Psi_\perp$ and ρ_z are non-zero at low temperature and all vanish at the same temperature $T_c \sim 0.8$ as the temperature is

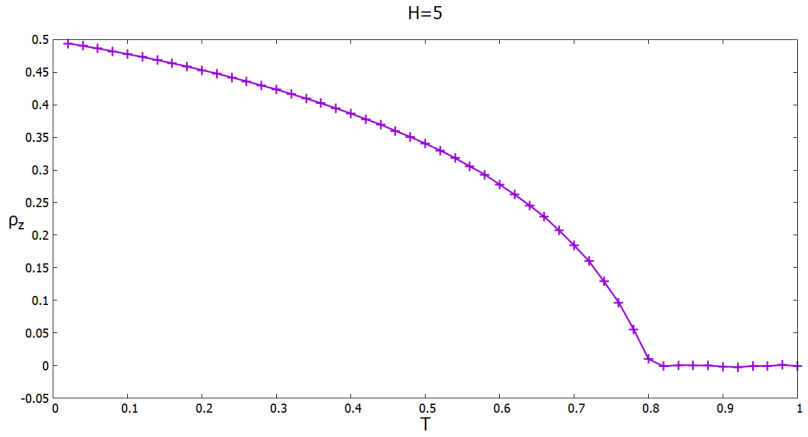

Figure 6.5: The spin stiffness ρ_z at $H = 5$ vs. T.

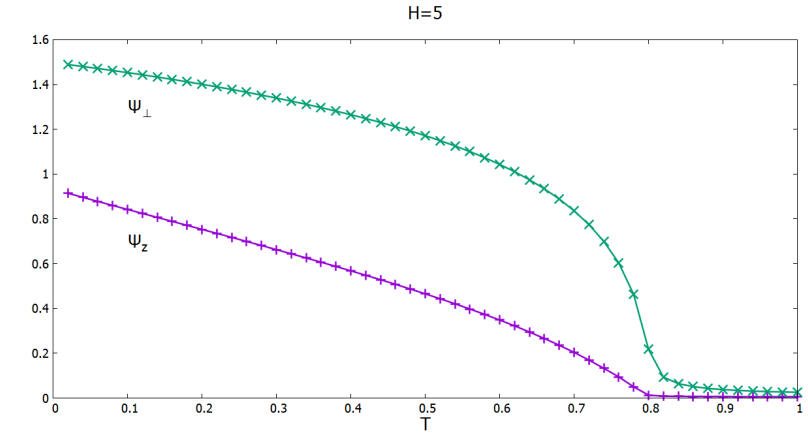

Figure 6.6: The order parameters Ψ_z, $\Psi_\perp$ at $H = 5$ vs. T.

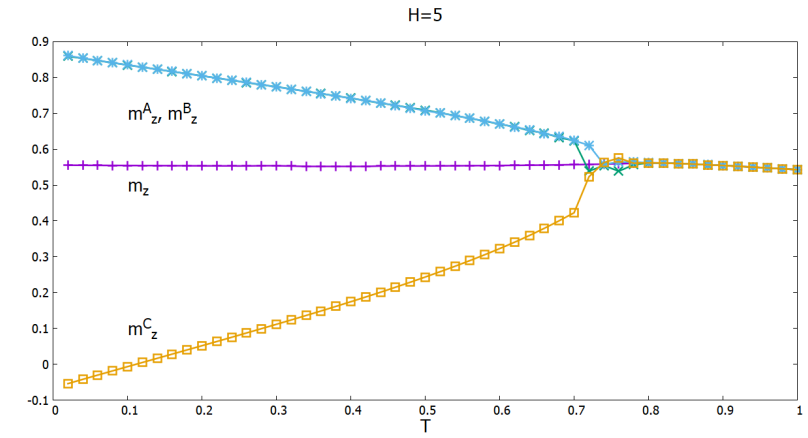

Figure 6.7: Total m_z and z-sublattice magnetizations at $H = 5$ vs. T.

increased. The only phase where all the order parameters have finite values is the V-phase, which then transitions to the paramagnetic phase as all the order parameters vanish as expected. This confirms that the behaviour of the order parameters for both the V-phase and paramagnetic phase is consistent with our predictions. Using (4.15), we predict that ρ_z should approach 0.498 at $T = 0$ as verified in Fig 6.5The spin stiffness ρ_z at $H = 5$ vs. Tfigure.6.5. The value of Ψ_z should approach 0.933 at $T = 0$ and $\Psi_\perp$ should approach 1.497 at $T = 0$ as verified in Fig 6.6The order parameters Ψ_z, $\Psi_\perp$ at $H = 5$ vs. Tfigure.6.6. These values are obtained from (3.12), (4.28) and (4.29). Finally, the sublattice magnetizations should approach 0.867 and -0.067 at $T = 0$ and the total m_z should approach 0.833 as verified in Fig. 6.7Total m_z and z-sublattice magnetizations at $H = 5$ vs. Tfigure.6.7. Fig. 6.8The specific heat per site at $H = 5$ vs. Tfigure.6.8 shows the specific heat for two different lattice sizes $L = 39, 42$. There is a peak at the $V - P$ transition which shows no significant size dependence and suggests that the specific heat critical exponent α is negative. Note that the specific heat approaches unity as $T \to 0$ since we are using a classical spin model with two degrees of freedom.

Scanning temperature at a lower fixed field value of $0 < H < 3$ was used to confirm our predictions for the other phases. For $H = 2.75$ the perpendicular order parameters ρ_z and $\Psi_\perp$ and the parallel order parameter Ψ_z are evidently non-zero at the lowest temperatures but vanish near $T_c \sim 0.14$ as shown in Figs. 6.9The spin stiffness ρ_z at $H = 2.75$ vs. Tfigure.6.9 and 6.10The order parameters Ψ_z, $\Psi_\perp$ at $H = 2.75$ vs. Tfigure.6.10. These results coupled with the plot of the sublattice magnetizations and the earlier zero temperature predictions indicate that the spins are in the Y-phase in this low temperature region. Using the results in Chapters 3 and 4, ρ_z should approach 0.054 at $T = 0$, Ψ_z should approach 1.958, $\Psi_\perp$ should approach 0.495, the sublattice magnetizations should approach 0.958 and -1.0 and m_z should go to 0.306. All of these predictions are confirmed in Figs. 6.9The spin stiffness ρ_z at $H = 2.75$ vs. Tfigure.6.9, 6.10The order parameters Ψ_z, $\Psi_\perp$ at $H = 2.75$ vs. Tfigure.6.10 and

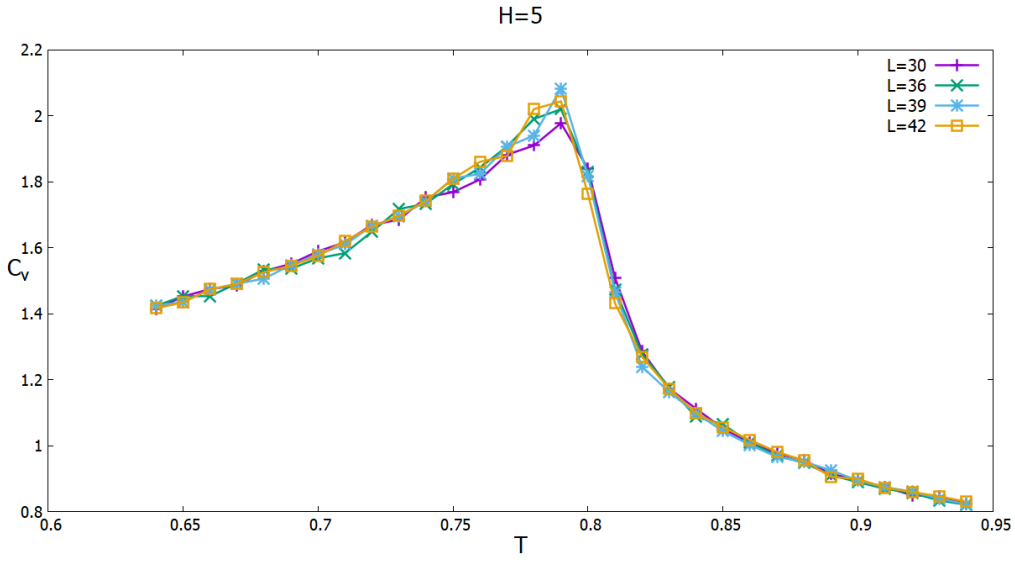

Figure 6.8: The specific heat per site at $H = 5$ vs. T.

6.11Total m_z and sublattice magnetizations at $H = 2.75$ vs. Tfigure.6.11.

At higher $T > 0.14$, the perpendicular order parameters are zero, while the Ψ_z remains non-zero. This is indicative that the sublattices are in the collinear configuration. The plots of the magnetizations in Fig. 6.11Total m_z and sublattice magnetizations at $H = 2.75$ vs. Tfigure.6.11 support this statement. At still higher temperatures, $T_c \sim 0.35$, the perpendicular order parameters again become non-zero, indicating that the system has undergone another phase transition into the V-phase. Both ρ_z and $\Psi_\perp$ increase steadily until $T \sim 0.82$, this maximum corresponds to when one of the sublattices in this phase is orientated perpendicular to the field. As the V continues to close up in this phase, the order parameters return to zero again to signify a transition into the paramagnetic phase near $T_c \sim 0.96$. The behaviour of these order parameters is consistent once again with our predictions as to their behaviour in the different phase structures. For the field scan at $H = 2.75$, the system passes through all three ordered phases.

This raises the question as to whether the sublattices can transition directly from

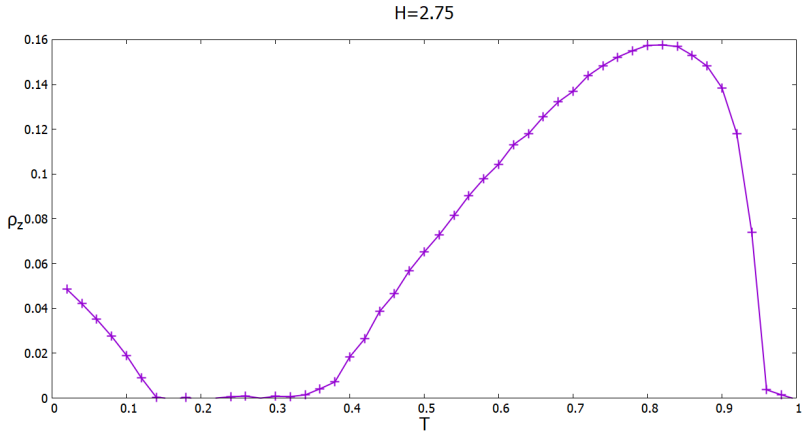

Figure 6.9: The spin stiffness ρ_z at $H = 2.75$ vs. T.

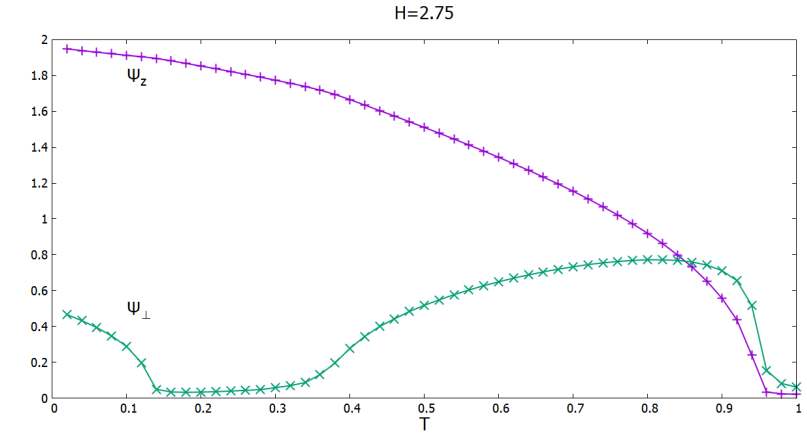

Figure 6.10: The order parameters Ψ_z, $\Psi_\perp$ at $H = 2.75$ vs. T.

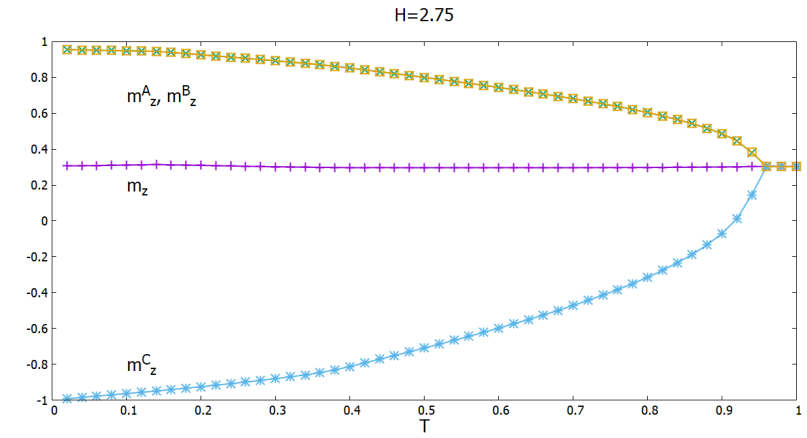

Figure 6.11: Total m_z and sublattice magnetizations at $H = 2.75$ vs. T.

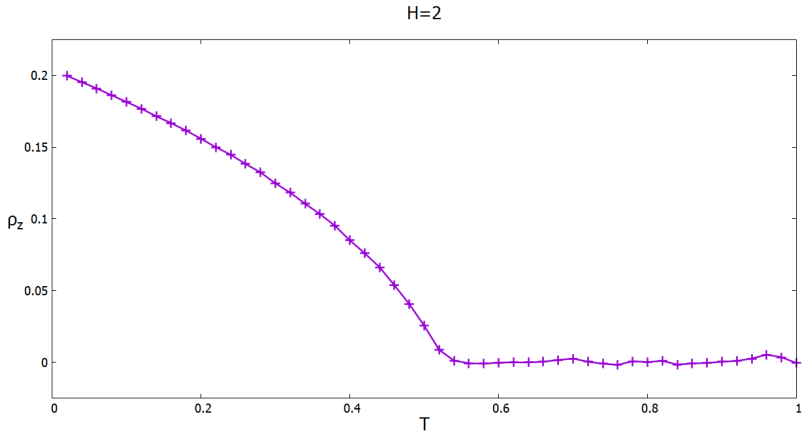

Figure 6.12: The spin stiffness ρ_z at $H = 2$ vs. T.

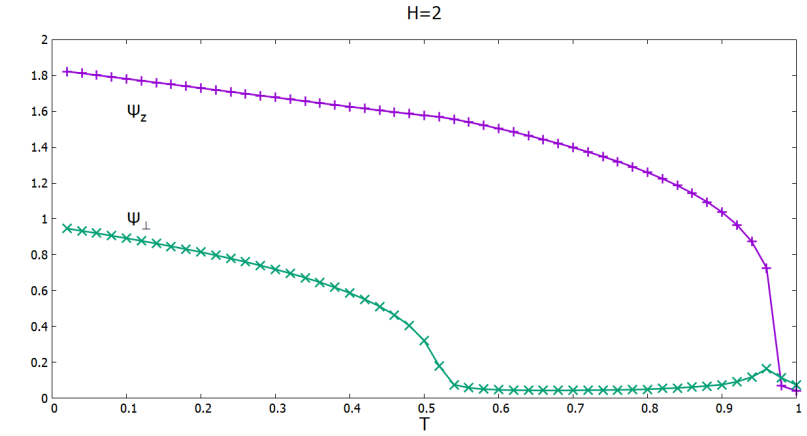

Figure 6.13: The order parameters $\Psi_z, \Psi_\perp$ at $H = 2$ vs. T.

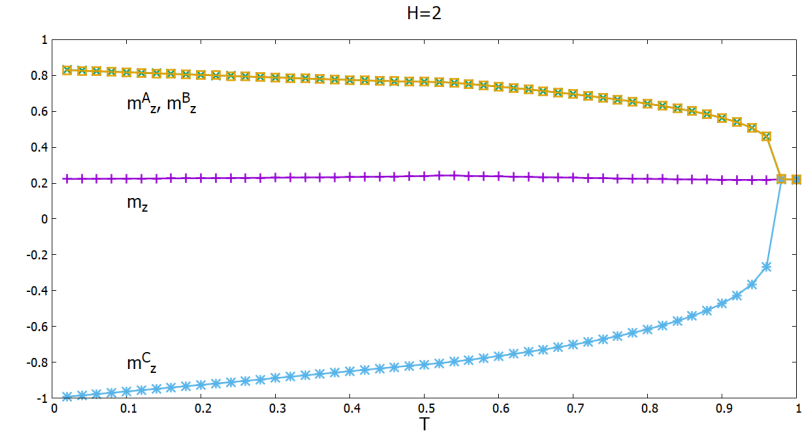

Figure 6.14: Total m_z and sublattice magnetizations at $H = 2$ vs. T.

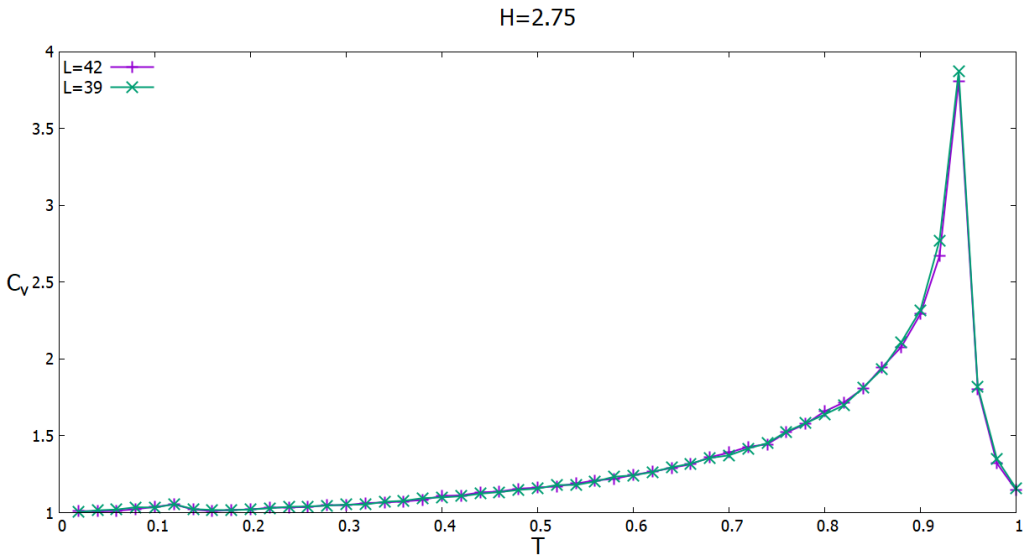

Figure 6.15: The specific heat per site at $H = 2.75$ vs. T.

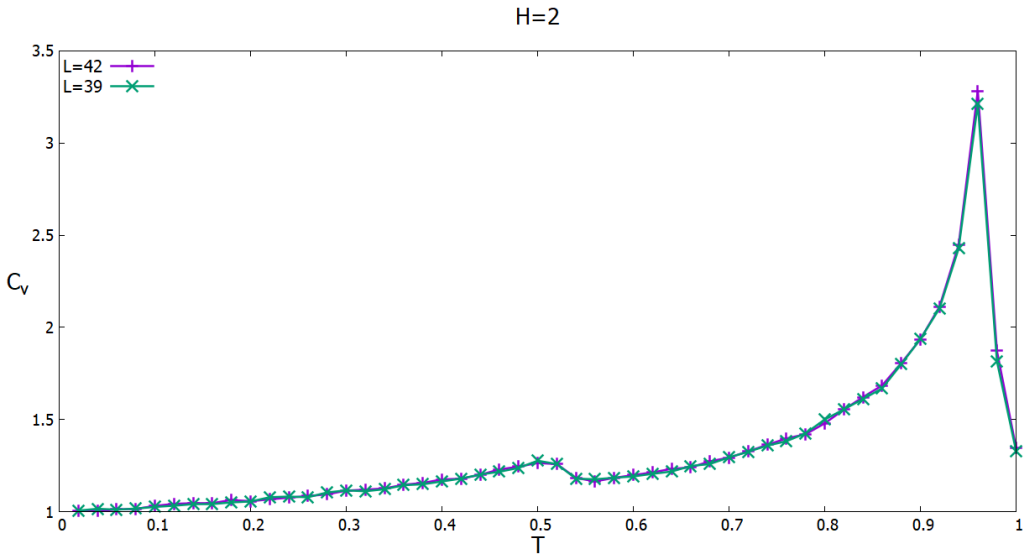

Figure 6.16: The heat capacity per site at $H = 2$ vs. T.

the collinear phase into the paramagnetic phase, skipping the V-phase in between as in the 2D cases[9]. Scans performed at a slightly lower field strength help to illuminate the scenario. Figs. 6.12The spin stiffness ρ_z at $H = 2$ vs. Tfigure.6.12, 6.13The order parameters $\Psi_z, \Psi_\perp$ at $H = 2$ vs. Tfigure.6.13 and 6.14Total m_z and sublattice magnetizations at $H = 2$ vs. Tfigure.6.14 show temperature scans at $H = 2$. Our zero temperature predictions indicate that the system is in the Y-phase at zero/low temperature. All parallel and perpendicular order parameters are non-zero and support this statement. As the temperature increases the perpendicular order parameters vanish near $T_c \sim .53$ indicating a transition into the collinear phase and these order parameters then remain zero for all higher temperatures, except for slight peaks near where the system undergoes the paramagnetic transition at $T \sim 0.96$. The parallel order parameter vanishes at a higher temperature $T_c \sim 0.96$ indicating that the system has undergone the transition into the paramagnetic phase. This picture is different to the one in the $H = 2.75$ case as at this field value the system does not undergo a C-V transition and instead transitions

Fig. 6.15The specific heat per site at $H = 2.75$ vs. Tfigure.6.15 shows the specific heat at $H = 2.75$ for two sizes $L = 39, 42$. There is a small peak near $T = 0.12$ and a much larger peak at $T = 0.94$. The smaller peak corresponds to the $Y - P$ transition and the larger peak to the $V - P$ transition. There does not seem to be any feature at the $Y - C$ transition near $T = 0.35$. There is no significant size dependence of the specific heat which would suggest that $alpha < 0$ at these two transitions. Fig. 6.16The heat capacity per site at $H = 2$ vs. Tfigure.6.16 shows the specific heat for $H = 2$ for sizes $L = 39, 42$. In this case the $Y - C$ transitions at approximately $T \sim 0.5$ and the $C - P$ transition occurs at $T_c \sim 0.96$. In both near $T \sim 0.96$ are clearly evident. The higher temperature peak exhibits a small size dependence which may indicate that α is positive for this transition.

These constant temperature and constant field scans lay out the foundation for the remainder of the analysis carried out on this system. We have correctly identified

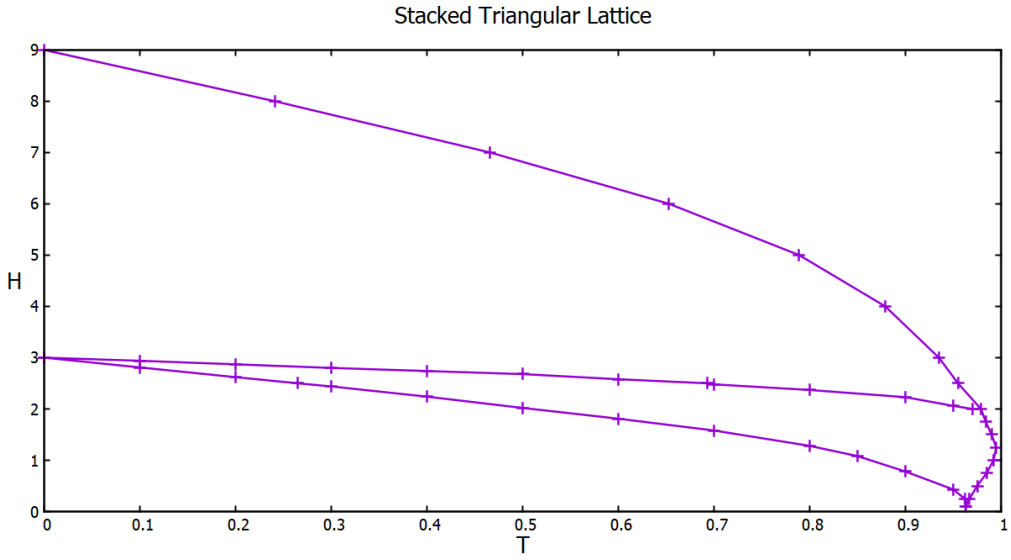

Figure 6.17: The phase diagram of the 3D triangular lattice indicating the regions of stability of the four phases Y, C, V and P.

order parameters which indicate the various ordered phases. To determine the true infinite lattice transition temperatures, finite size scaling analysis will be employed and the Monte Carlo simulations will be run multiple times at different lattice sizes. The finite size effects in the various order parameters become more pronounced at the transitions and this will be used to find the transition temperature T_c and critical exponents where possible.

6.3 Phase Diagram

We have carried out both temperature and field scans for various lattice sizes L and used the behaviour of the order parameters $\rho_z, \psi_\perp, \psi_z$ as well as the specific heat to obtain a phase diagram in the $H-T$ plane as shown in Fig. 6.17The phase diagram of the 3D triangular lattice indicating the regions of stability of the four phases Y, C, V and Pfigure.6.17. There are three ordered phases labelled as V, Y and C as well as a paramagnetic phase P. An interesting feature of the diagram is the bulge in the low

field region where the C-phase is stable to higher temperatures than the other ordered phases. As we discussed in chapter 3, this phase has a high degeneracy at $T = 0$ where one sublattice is parallel to the field but the other two sublattices are anti-parallel with each other but can have any direction. The additional entropy associated with this phase could stabilize it relative to the other phases at finite temperatures. There are four transitions between the relevant regions and we will analyse and classify each transition separately. These are the $V - P, C - P, V - C$, and $Y - C$ transitions. We will consider four different field values $H = 1.5, 2, 2.5$ and 5. The first two will be used to study the $C - P$ transition, $H = 2.5$ will be used to study the $Y - C$ and $C - V$ transitions, and $H = 5$ will be used to study the $V - P$ transition. We discuss each of these transitions in the following subsections.

6.3.1 V-phase to Paramagnetic Transition

In the V-phase we have multiple order parameters changing from a finite value in the V-phase to zero in the paramagnetic phase. The spin stiffness ρ_z, $\xi_\parallel$, $\xi_\perp$, Ψ_z, and $\Psi_\perp$ all characterize this transition. The scaled parallel and perpendicular correlation lengths are plotted in Figs. 6.18$\xi_\parallel/L$ vs. T for system sizes $L = 30, 36, 39, 42$figure.6.18 and 6.19$\xi_\perp/L$ vs. T for system sizes $L = 30, 36, 39, 42$figure.6.19 respectively and the crossing points of the different lattice sizes indicate a transition near the same temperatures. The scaled spin stiffness is also plotted in Fig. 6.20$L\rho_z$ vs. T for system sizes $L = 30, 36, 39, 42$figure.6.20 to locate the transition temperature. As mentioned in the previous section on finite size scaling, at the transition temperature these scaled values should cross at the transition point T_c. The crossing point of the largest sizes is used to estimate the transition temperature. These plots all indicate a similar transition temperature of $T_c \sim 0.7925$.

With the transition temperature known, the scaling forms of ρ_z, $\xi_\parallel$ and $\xi_\perp$ are used to find the critical exponent ν from a collapse of the data for different sizes using a least square fitting algorithm[30]. It is found that $\nu = 0.68$ collapses these three

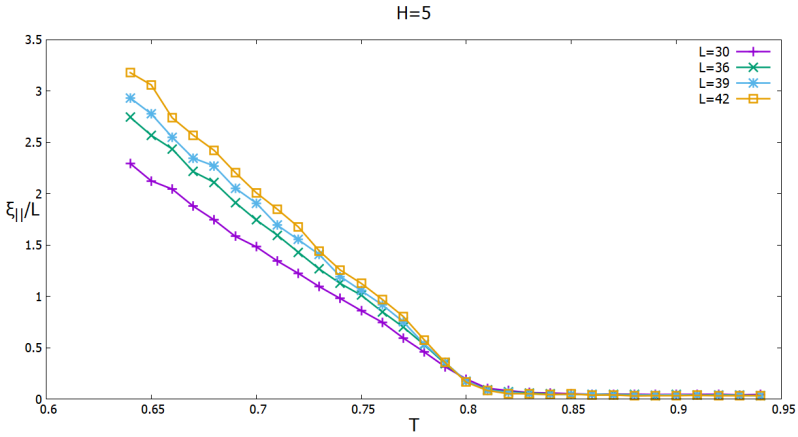

Figure 6.18: $\xi_{||}/L$ vs. T for system sizes $L = 30, 36, 39, 42$

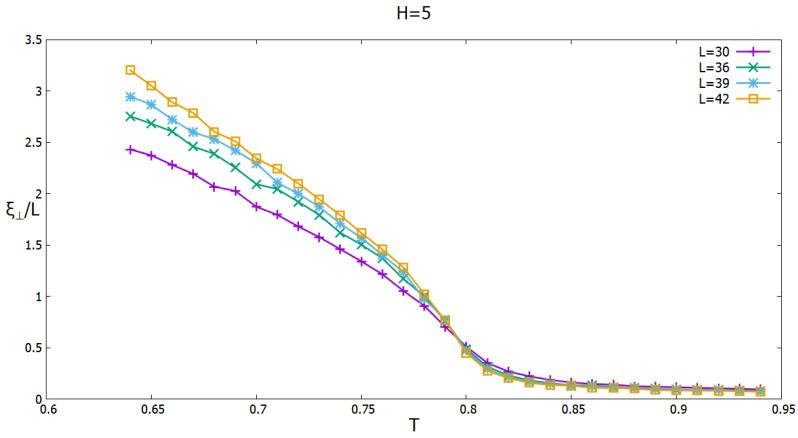

Figure 6.19: $\xi_{\perp}/L$ vs. T for system sizes $L = 30, 36, 39, 42$

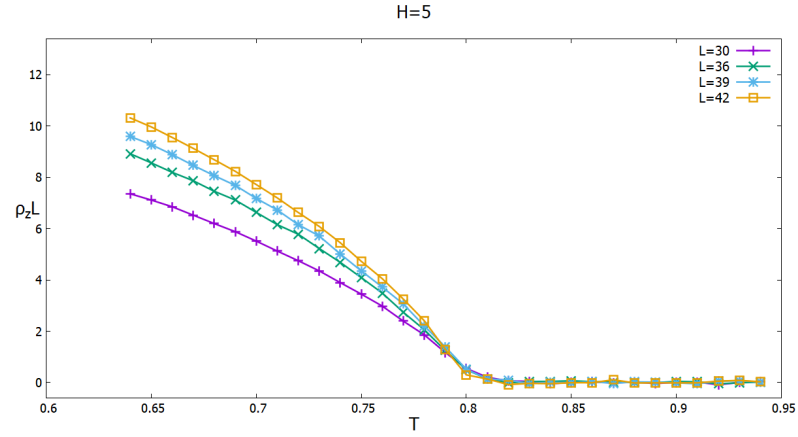

Figure 6.20: $L\rho_z$ vs. T for system sizes $L = 30, 36, 39, 42$

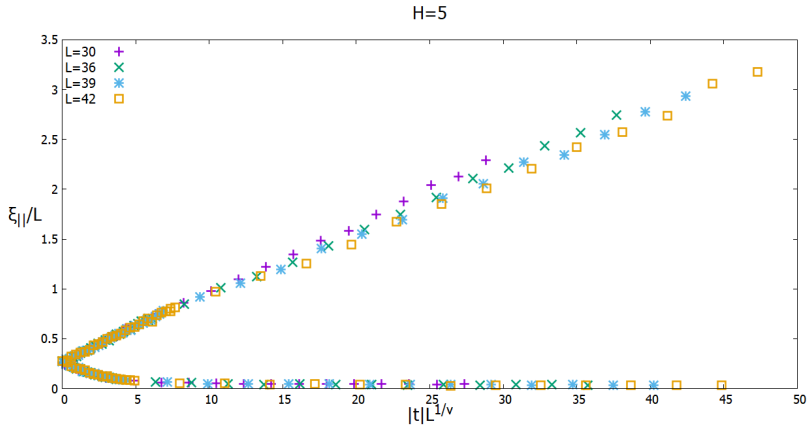

Figure 6.21: Data collapse of the correlation length $\xi_{\|}$ at $H = 5$ yields $\nu = 0.68$

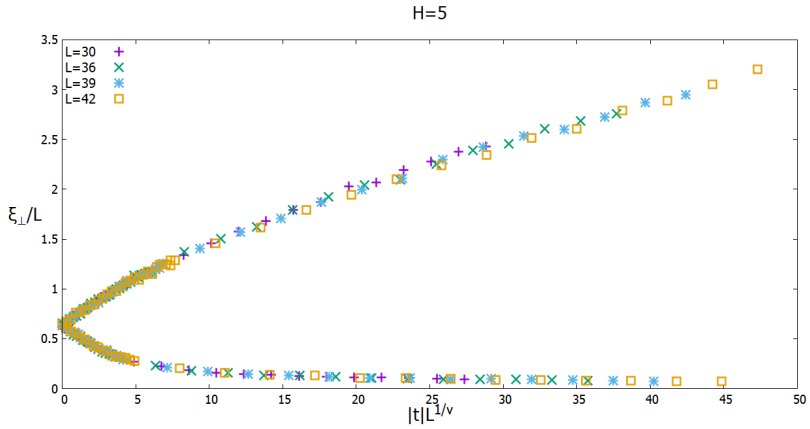

Figure 6.22: Data collapse of the correlation length $\xi_{\perp}$ at $H = 5$ yields $\nu = 0.68$

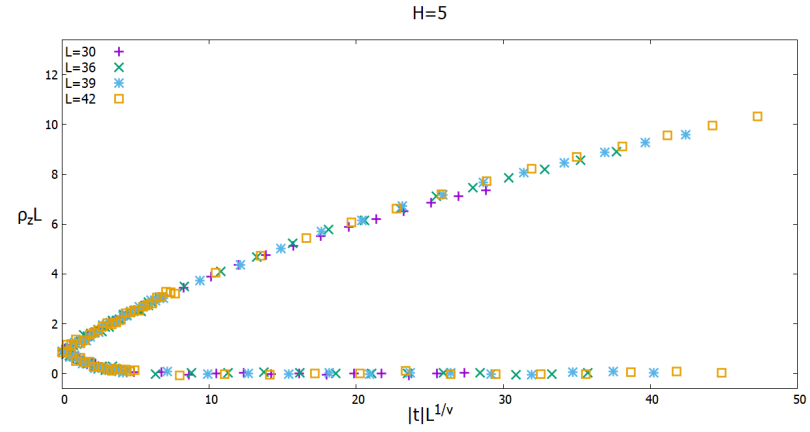

Figure 6.23: Data collapse of the stiffness ρ_z at $H = 5$ yields $\nu = 0.68$

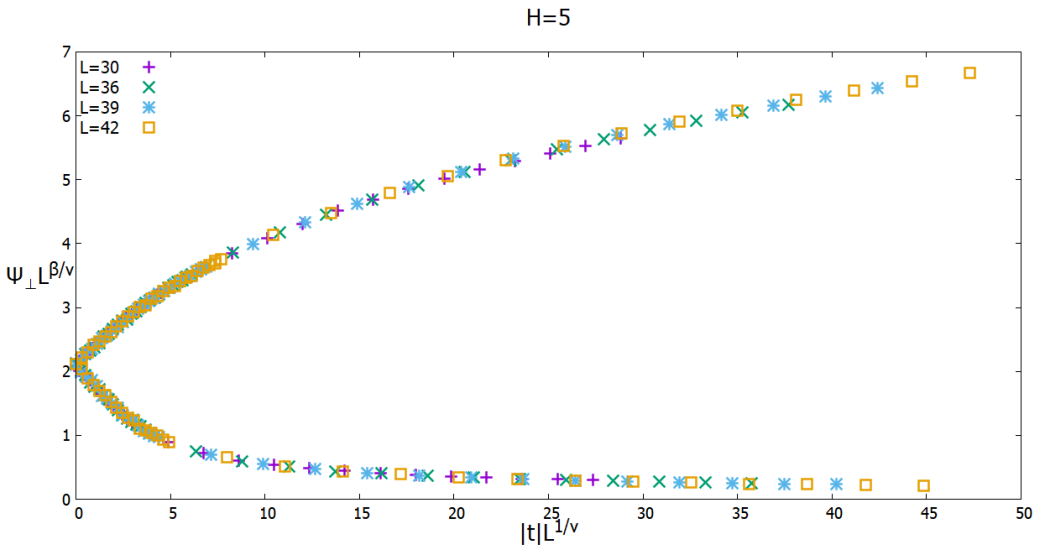

Figure 6.24: Data collapse of $\Psi_\perp$ at $H = 5$ with $\nu = 0.68$ and $\beta \sim 0.35$

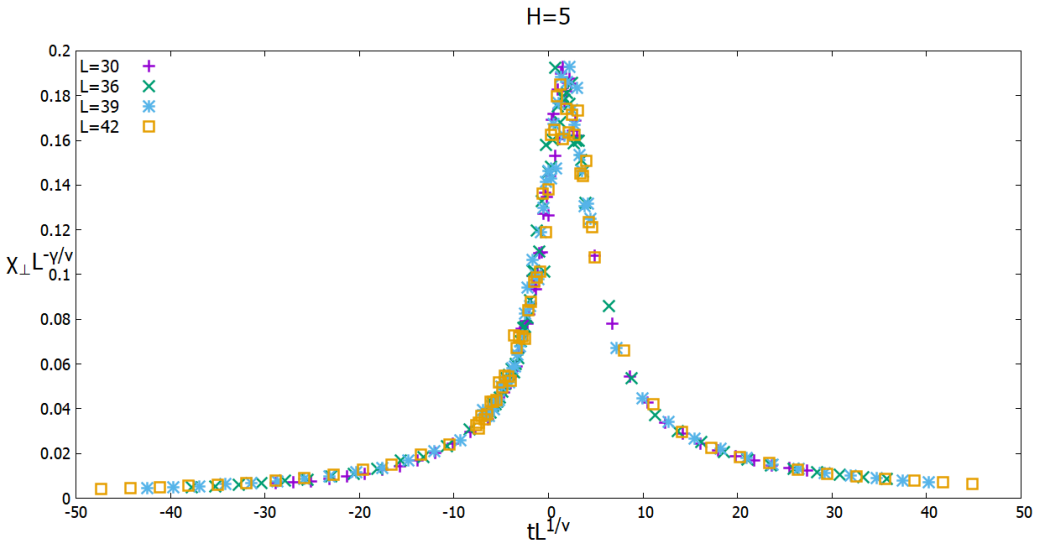

Figure 6.25: Data collapse of $\chi_\perp$ at $H = 5$ with $\nu = 0.68$ and $\gamma \sim 1.35$

quantities as shown in Figs. 6.21Data collapse of the correlation length $\xi_{\|}$ at $H = 5$ yields $\nu = 0.68$figure.6.21, 6.22Data collapse of the correlation length $\xi_{\perp}$ at $H = 5$ yields $\nu = 0.68$figure.6.22 and 6.23Data collapse of the stiffness ρ_z at $H = 5$ yields $\nu = 0.68$figure.6.23. With ν and the critical temperature T_c known the remaining critical exponents can be determined. We use $\Psi_{\perp}$ and $\xi_{\perp}$ and find a value of $\beta \sim 0.35$ and $\gamma \sim 1.35$. The data collapses for $\Psi_{\perp}$ and $\xi_{\perp}$ are shown in Figs. 6.24Data collapse of $\Psi_{\perp}$ at $H = 5$ with $\nu = 0.68$ and $\beta \sim 0.35$figure.6.24 and 6.25Data collapse of $\chi_{\perp}$ at $H = 5$ with $\nu = 0.68$ and $\gamma \sim 1.35$figure.6.25.

6.3.2 Y-Phase Transition to C-Phase

To characterize the transition from the Y-phase to the collinear phase we utilize the perpendicular correlation length $\xi_{\perp}$, the spin stiffness ρ_z, and the perpendicular order parameter $\Psi_{\perp}$. The latter two order quantities vary from finite values in the Y-phase region to zero in the collinear phase. The correlation length and spin stiffness have finite size scaling forms that allow for an accurate estimation of the critical transition temperature T_c using the crossing point as in the previous case. The parallel components of the correlation length $\xi_{\|}$ and the order parameter Ψ_z are not useful in characterizing this transition since Ψ_z does not vanish at the transition.

As can be seen from the finite size scaling forms in (5.28), plots of $L\rho_z$ and $\xi_{\perp}/L$ as a function of T for different system sizes L should intersect at $t = 0$ yielding a value of T_c. Figs. 6.26$L\rho_z$ vs. T for system sizes $L = 30, 36, 39, 42$figure.6.26 and 6.27$\frac{\xi_{\perp}}{L}$ vs. T for system sizes $L = 30, 36, 39, 42$figure.6.27 show plots of $L\rho_z$ and $\xi_{\perp}/L$ for a fixed value of the field $H = 2.5$. For both quantities the curves intersect near $T_c \sim 0.263$. The specific heat is shown in Fig. 6.28The specific heat at $H = 2.5$ vs. T for sizes $L = 30, 36, 39, 42$figure.6.28 and exhibits a small peak (note the vertical scale) at the transition which is independent of system size L suggesting that $\alpha < 0$. Using the critical temperature we can then attempt to find the ν exponent that will properly collapse the data for the correlation length and the stiffness onto a universal curve.

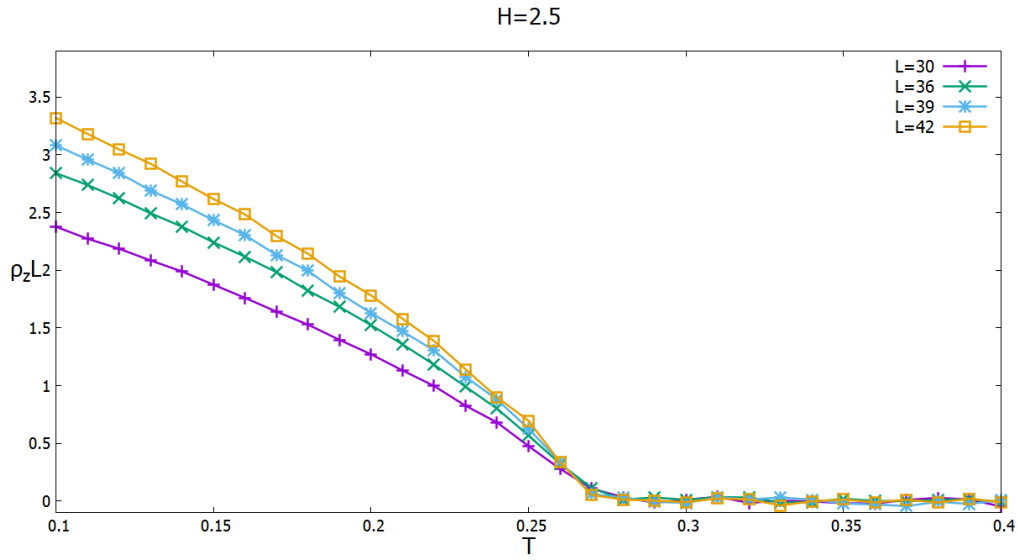

Figure 6.26: $L\rho_z$ vs. T for system sizes $L = 30, 36, 39, 42$.

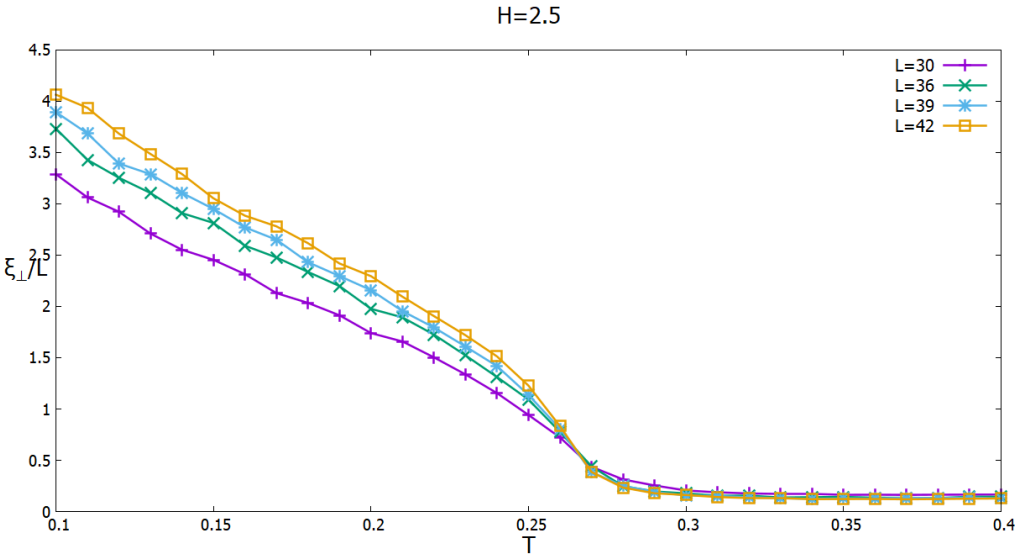

Figure 6.27: $\frac{\xi_\perp}{L}$ vs. T for system sizes $L = 30, 36, 39, 42$.

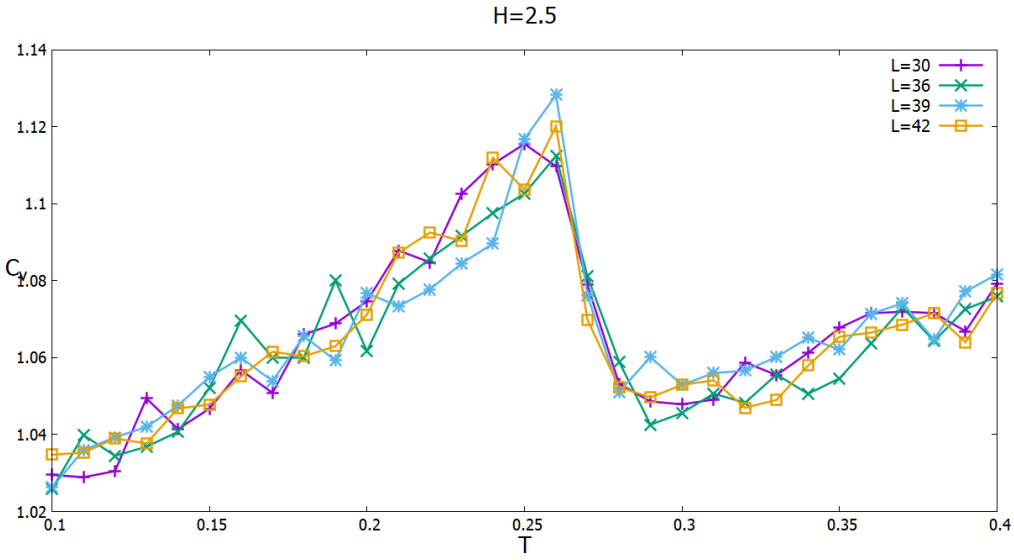

Figure 6.28: The specific heat at $H = 2.5$ vs. T for sizes $L = 30, 36, 39, 42$.

We find that both data sets can be collapsed with the same exponent coupled with the knowledge of T_c. Figs. 6.29Data collapse of the spin stiffness at $H = 2.5$ with $\nu = 0.66$figure.6.29 and 6.30Data collapse of $\xi_\perp/L$ at $H = 2.5$ with $\nu = 0.66$figure.6.30 show the collapsed data for T near T_c and we find the value $\nu = 0.66$ in both cases. The scaling laws in (5.25Continuous phase transitions : critical exponents, scaling and universalityequation.5.3.24) can be combined to yield $\alpha = 2 - d\nu = -0.02$ consistent with $\alpha < 0$ as suggested by the specific heat behaviour.

With the knowledge of both T_c and ν, we can use the scaling form for the perpendicular order parameter $\Psi_\perp$ to collapse the results for different L onto a universal curve and determine a value of $\beta = 0.35$. We can then apply (5.28$FiniteSizeScalingatSecondOrderTrans$ with the susceptibility $\chi_\perp$ to find a value of $\gamma = 1.28$. Figs. 6.31Collapse of $\Psi_\perp$ yields a value of $\nu = 0.66$ and $\beta \approx 0.35$figure.6.31 and 6.32Collapse of the order parameter susceptibility yields a value of $\nu = 0.66$ and $\gamma = 1.28$figure.6.32 show the collapsed data for these quantities. We will summarize the values of the critical exponents for all transitions in Table 6.1 at the end of this chapter.

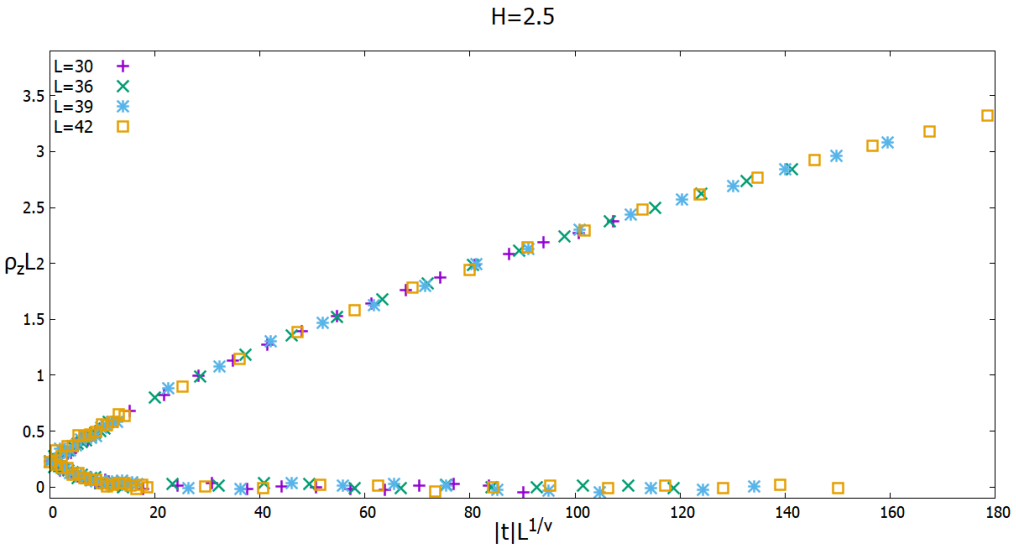

Figure 6.29: Data collapse of the spin stiffness at $H = 2.5$ with $\nu = 0.66$

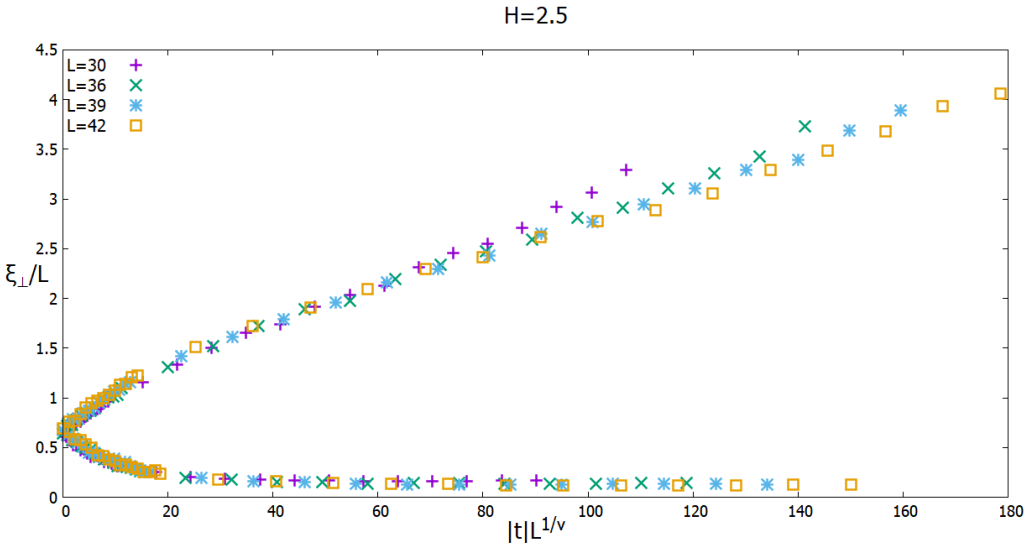

Figure 6.30: Data collapse of $\xi_\perp/L$ at $H = 2.5$ with $\nu = 0.66$

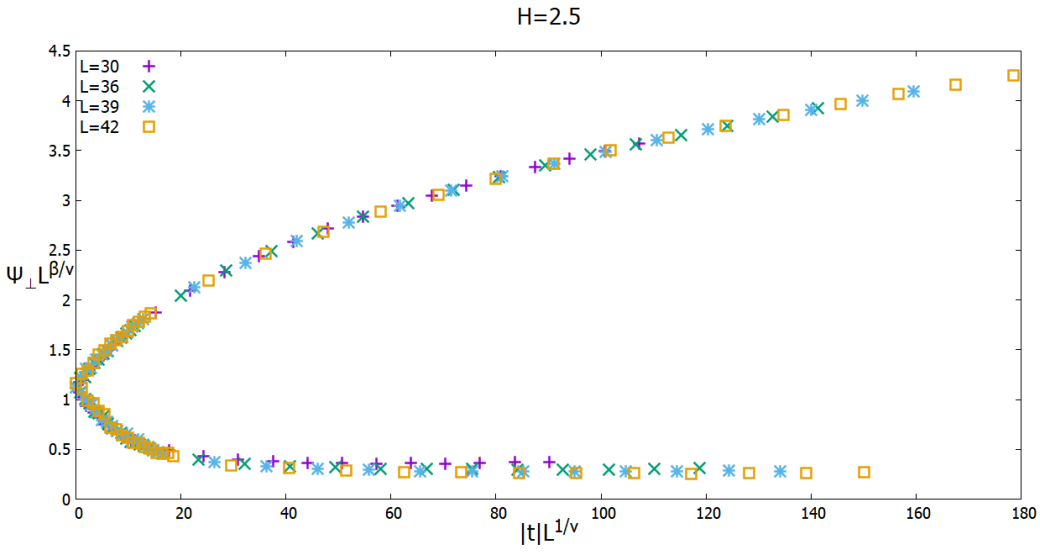

Figure 6.31: Collapse of $\Psi_\perp$ yields a value of $\nu = 0.66$ and $\beta \approx 0.35$.

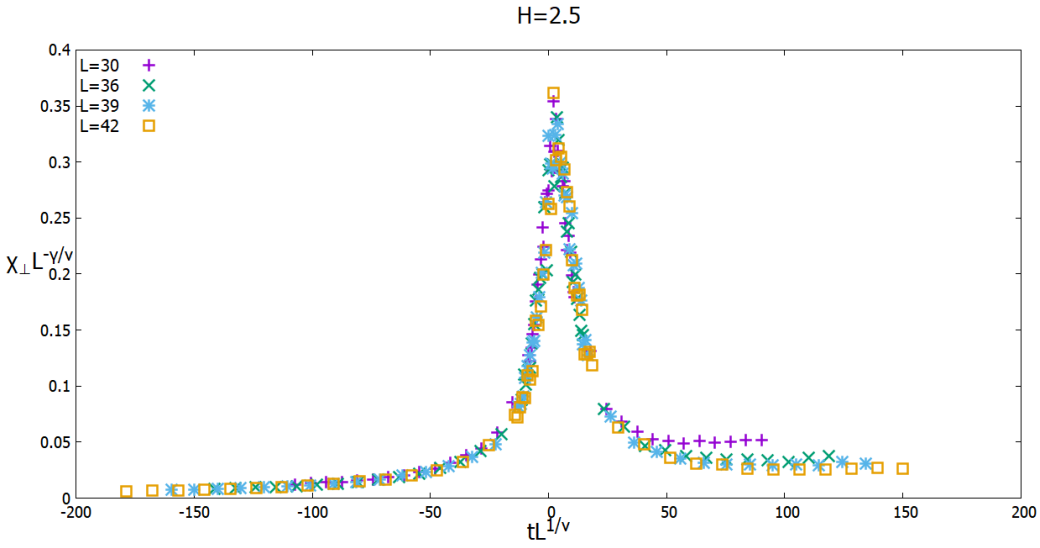

Figure 6.32: Collapse of the order parameter susceptibility yields a value of $\nu = 0.66$ and $\gamma = 1.28$

6.3.3 C-Phase Transition to V-Phase

The transition from the collinear phase to the so-called V-phase at $H = 2.5$ can be characterized with the spin stiffness ρ_z, perpendicular correlation length $\xi_\perp$ and the perpendicular order parameter $\Psi_\perp$ as in the case of the transition from the Y-phase to the collinear phase. These variables are zero in the collinear phase but are finite valued in the V-phase. Using the scaling forms for the correlation length and spin stiffness we are able to use the crossing points of the different lattice sizes as an estimate for the critical temperature of the transition. Figs. 6.33$\rho_z L$ vs. T for system sizes $L = 30, 36, 39, 42$figure.6.33 and 6.34$\frac{\xi_\perp}{L}$ vs. T for system sizes $L = 30, 36, 39, 42$figure.6.34 show plots of these quantities for different L and yield a value of $T_c \sim 0.69$. Fig.6.35The specific heat at $H = 2.5$ for system sizes $L = 30, 36, 39, 42$. The noise in this data is due to slow change of the order parameetr across this transitionfigure.6.35 shows the specific heat which does not exhibit any significant size dependence at the transition suggesting again that $\alpha < 0$.

Using the transition temperature, the ν exponent can be extracted using the scaling forms of the spin stiffness and perpendicular correlation length. Assuming a second order transition we attempt to find a common ν to collapse the data using the value of T_c. Figs. 6.36Data collapse of ρL at $H = 2.5$ with a $\nu = 0.77$figure.6.36 and 6.37Data collapse of $\frac{\xi_\perp}{L}$ at $H = 2.5$ with a $\nu = 0.77$figure.6.37 show the data collapse with $\nu = 0.77$. Once ν is found we wish to find the remaining set of exponents, β and γ using the perpendicular order parameter $\Psi_\perp$ and the corresponding susceptibility $\chi_\perp$. Using the data collapse algorithm we find $\beta = 0.40$ and $\gamma = 1.52$. The data collapse for $\Psi_\perp$ and $\xi_\perp$ are shown in Figs.6.38The data collapse of $|\Psi_\perp|$ at $H = 2.5$ with a $\nu = 0.77$ and $\beta = 0.40$figure.6.38 and 6.39Data collapse of $\chi_\perp$ at $H = 2.5$ with a $\nu = 0.77$ and $\gamma = 1.52$figure.6.39. Using the scaling law $\alpha = 2 - d\nu = -0.32$ which is large and negative as suggested by the specific heat behaviour. A summary of these exponents will be given later in Table 6.1.

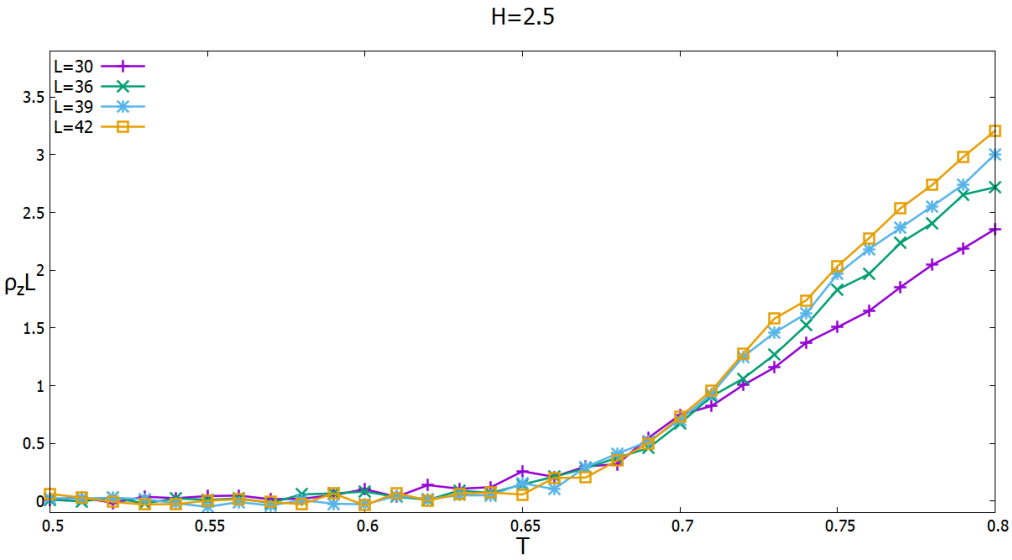

Figure 6.33: $\rho_z L$ vs. T for system sizes $L = 30, 36, 39, 42$

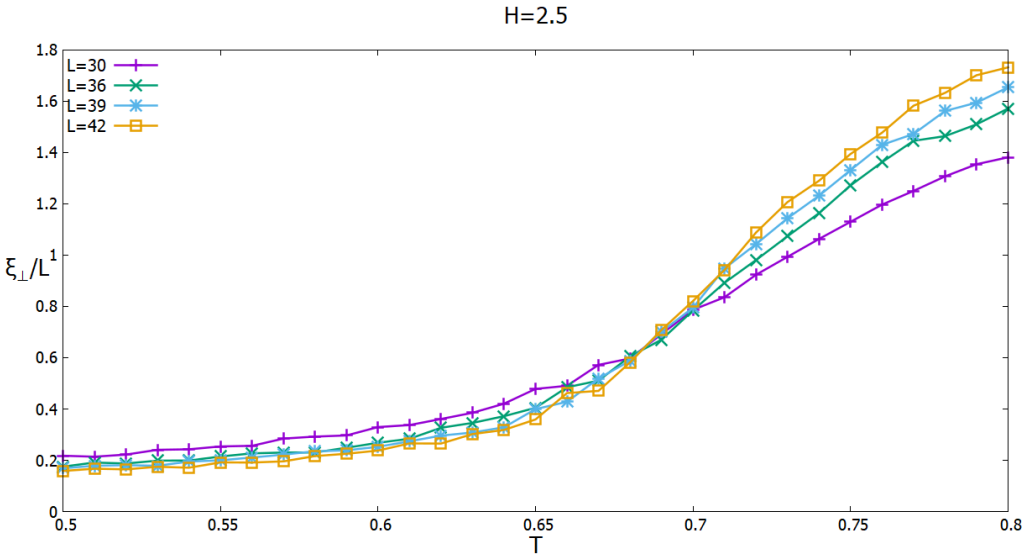

Figure 6.34: $\frac{\xi_\perp}{L}$ vs. T for system sizes $L = 30, 36, 39, 42$

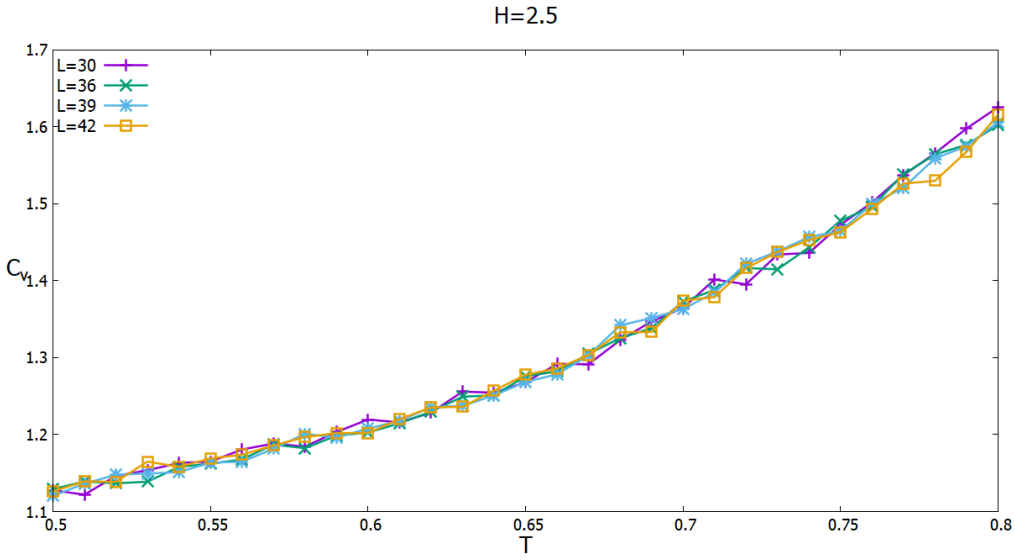

Figure 6.35: The specific heat at $H = 2.5$ for system sizes $L = 30, 36, 39, 42$. The noise in this data is due to slow change of the order parameeter across this transition.

6.3.4 C-Phase Transition to Paramagnetic Phase

To characterize the transition from the collinear phase to the paramagnetic phase at $H = 1.5$ we utilize the parallel correlation length $\xi_{\|}$ and the parallel order parameter Ψ_z. These order parameters are finite valued in the collinear phase and zero in the paramagnetic phase. The correlation length's finite size scaling form will allow for an accurate estimation of the critical transition temperature. This transition is of particular interest because on the phase diagram Fig. 6.17The phase diagram of the 3D triangular lattice indicating the regions of stability of the four phases Y, C, V and Pfigure.6.17 it is present to the highest temperature indicating that the collinear phase is surprisingly stable. This may be due to the high degeneracy of the collinear phase at low T where one sublattice is parallel to the field and the other two are anti-parallel but can have arbitrary orientation with respect to the field direction. Fig.6.40Graph of the scaling form of the parallel correlation length $\xi_{\|}$ for multiple lattice sizes at $H = 1.5$ across the C-P transition. The intersection of the points indicates a transition

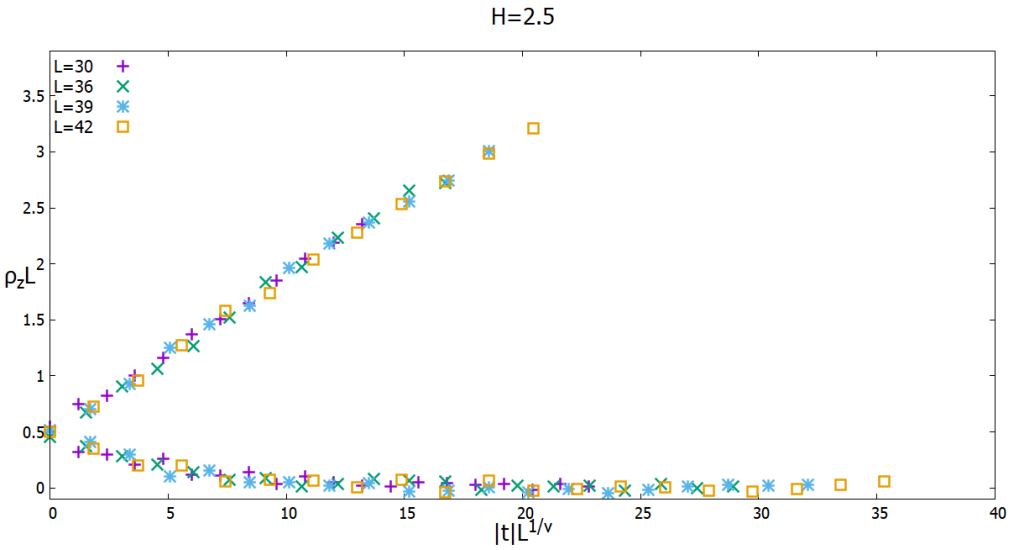

Figure 6.36: Data collapse of ρL at $H = 2.5$ with a $\nu = 0.77$

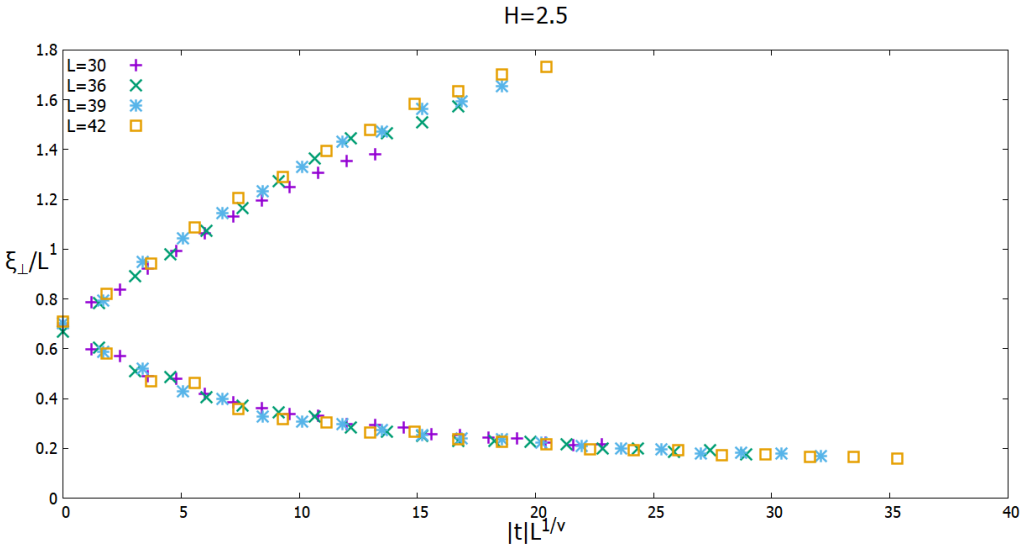

Figure 6.37: Data collapse of $\frac{\xi_\perp}{L}$ at $H = 2.5$ with a $\nu = 0.77$

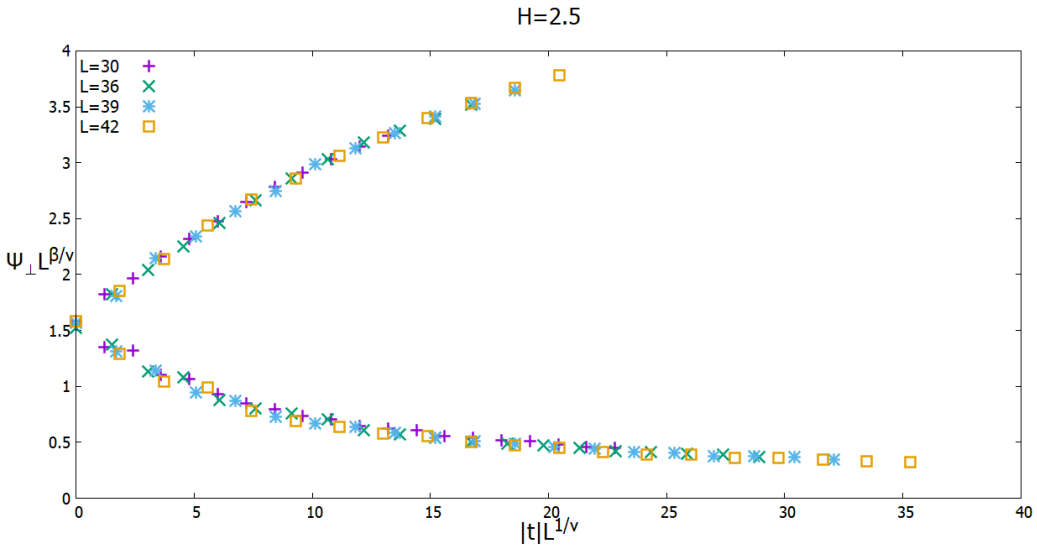

Figure 6.38: The data collapse of $|\Psi_\perp|$ at $H = 2.5$ with a $\nu = 0.77$ and $\beta = 0.40$.

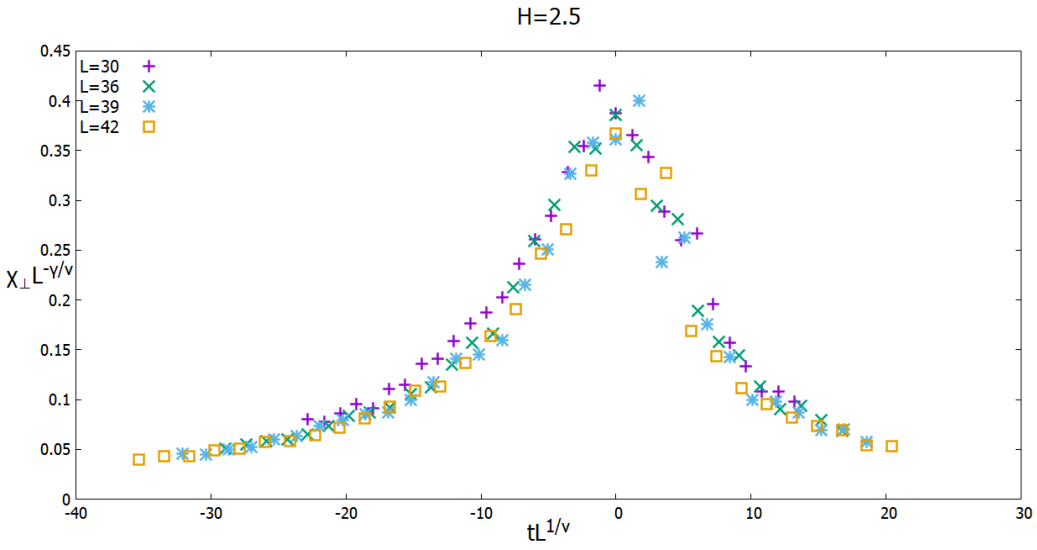

Figure 6.39: Data collapse of $\chi_\perp$ at $H = 2.5$ with a $\nu = 0.77$ and $\gamma = 1.52$

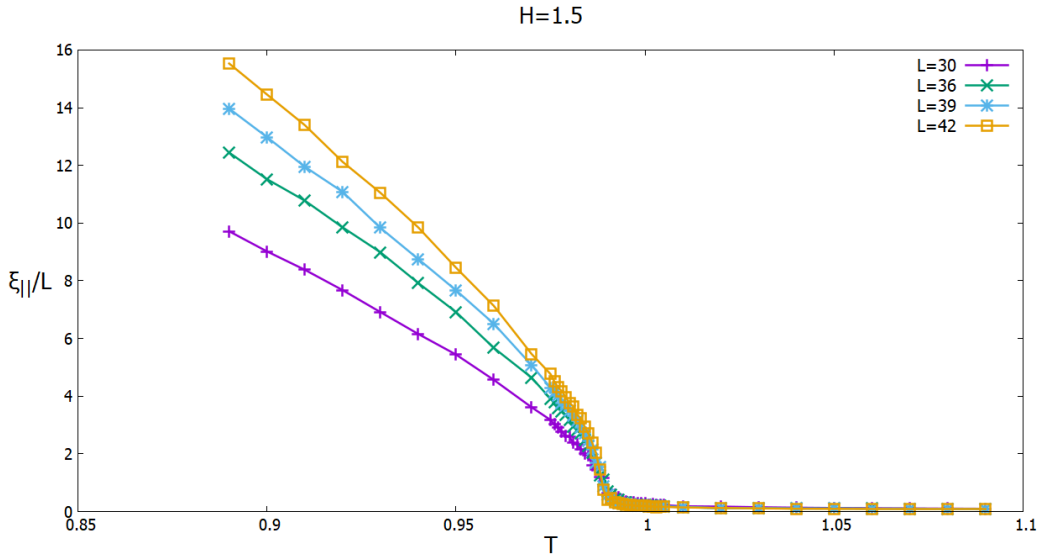

Figure 6.40: Graph of the scaling form of the parallel correlation length $\xi_{\|}$ for multiple lattice sizes at $H = 1.5$ across the C-P transition. The intersection of the points indicates a transition temperature $T_c = 0.988$.

temperature $T_c = 0.988$figure.6.40 shows the correlation length for various lattice sizes which cross at $T_c \sim 0.988$. Fig.6.41The specific heat at $H = 1.5$figure.6.41 shows the specific heat which exhibits a sharp peak at the transition with a weak dependence on L suggesting that the specific heat diverges.

Using the critical temperature we can attempt to find the ν exponent that will properly collapse the data for the correlation length using the fitting algorithm. Assuming a second order transition we expect ν to be universal and collapse both parameters Ψ_z and $\xi_{\|}$. We find that both data sets can be collapsed with the same exponent $\nu = 0.47$ as shown in Figs. 6.42Data collapse of the correlation length at $H = 1.5$ with a $\nu = 0.47$figure.6.42 and 6.43Data collapse of the correlation length at $H = 1.5$ with a $\nu = 0.47$ and $\beta = 0.22$figure.6.43.

In addition we obtain a value for β from the data of parallel Ψ_z. We can then apply (5.28$FiniteSizeScalingatSecondOrderTransitionsequation$.5.4.28) for the susceptibility $\chi_{\|}$ to find γ. We find $\beta = 0.22$ and $\gamma = 0.97$. The collapse of the data for $\chi_{\|}$ is

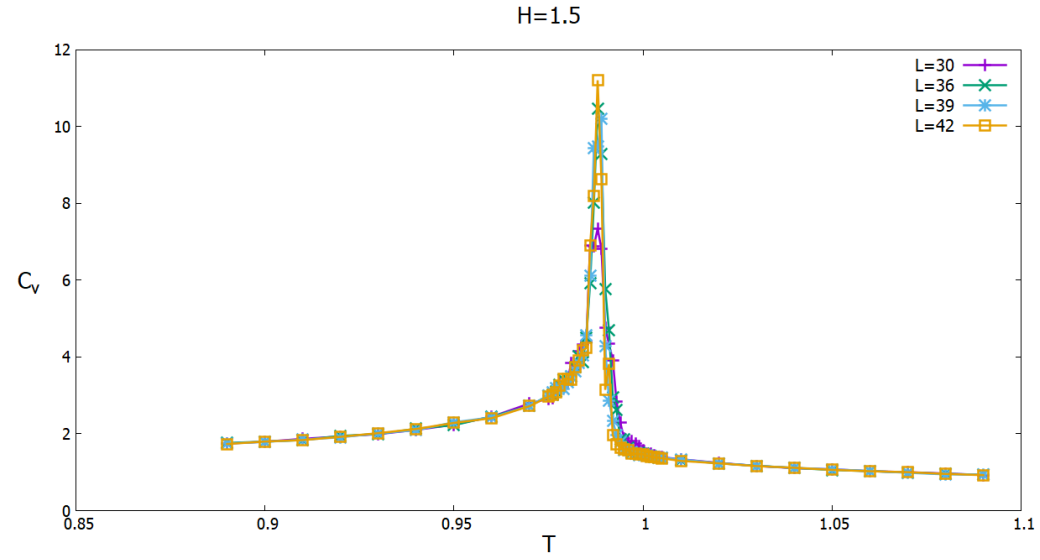

Figure 6.41: The specific heat at $H = 1.5$

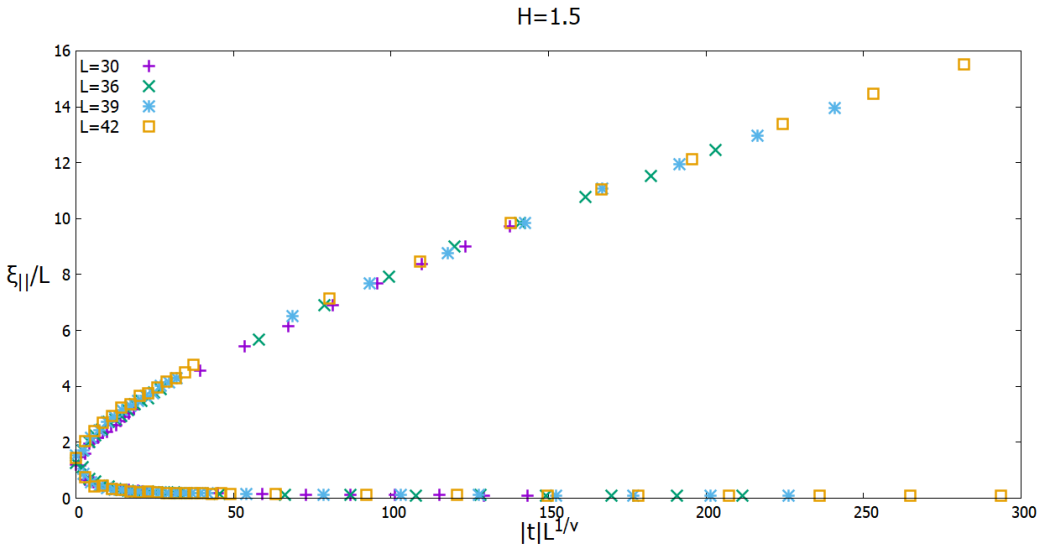

Figure 6.42: Data collapse of the correlation length at $H = 1.5$ with a $\nu = 0.47$

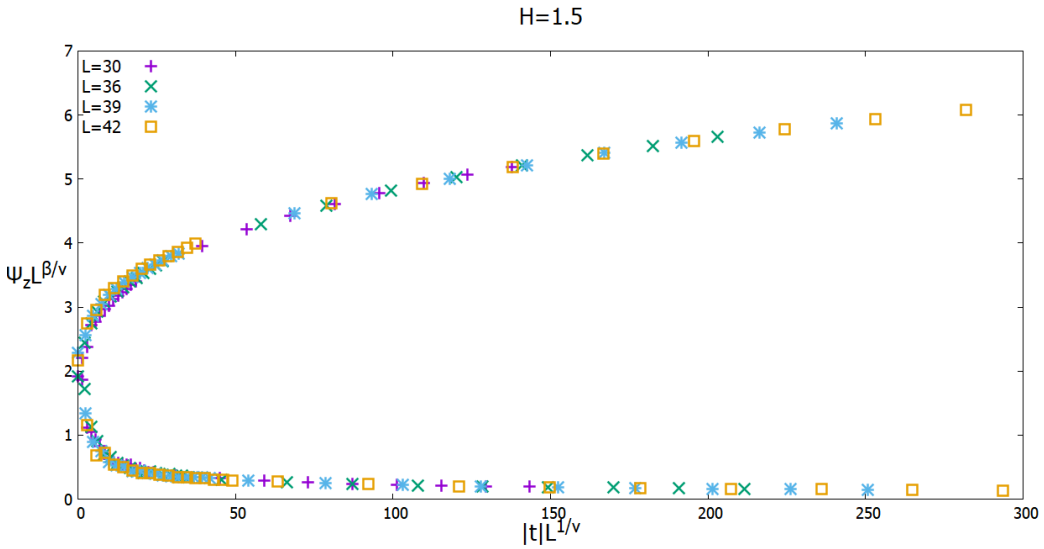

Figure 6.43: Data collapse of the correlation length at $H = 1.5$ with a $\nu = 0.47$ and $\beta = 0.22$

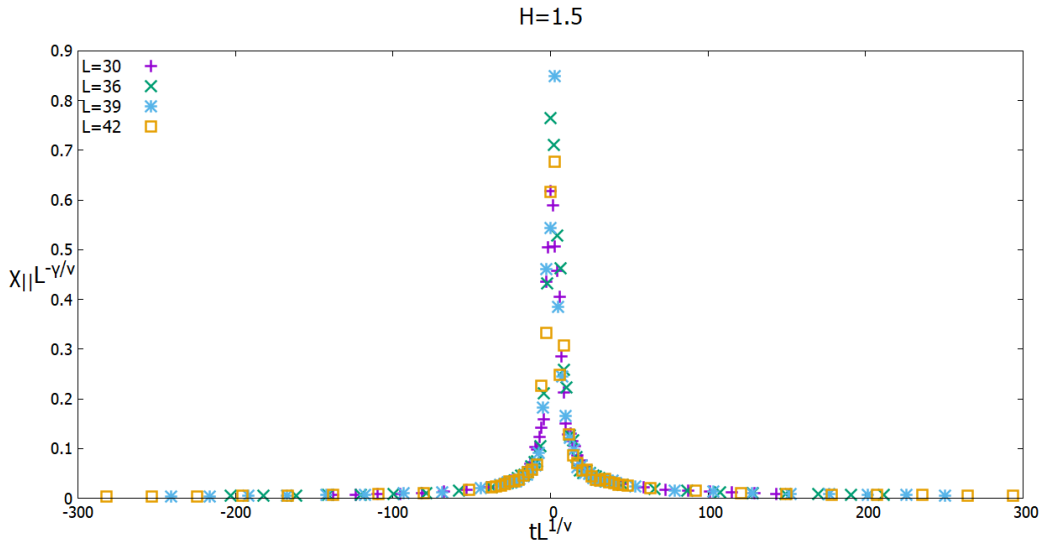

Figure 6.44: Data collapse of the order paramater susceptibility at $H = 1.5$ with a $\nu = 0.47$ and $\gamma \approx 0.97$

shown in Fig. 6.44Data collapse of the order paramater susceptibility at $H = 1.5$ with a $\nu = 0.47$ and $\gamma \approx 0.97$figure.6.44. In this case we find a value of $\alpha = 2 - d\nu = 0.59$ which is consistent with a divergent specific heat.

Our ability to collapse the data onto universal curves using critical exponents seems to indicate a second order transition. However, as we can see in the phase diagram Fig. 6.17, the $C - P$ phase boundary at $H = 2$ is very close to the point where the V, C and P phases all meet. For this reason, we performed our analysis on the $C - P$ transition at $H = 1.5$. Analysis done at $H = 2$ found similar exponents. These are summarized in Table 6.1.

6.4 Critical Exponents

We have used temperature scans at fixed values of the applied field to study the phase transitions between the three ordered phases Y, C, and V and with the paramagnetic phase P. The 3D ferromagnetic Heisenberg model universality class exponents in zero field are not known exactly but have been estimated by various Monte Carlo and renormalization group methods[31]. The values are listed in the first row of Table 6.1. Note that the specific heat exponent α is negative the correlation function exponent η is positive. It has been proven that, for second order phase transitions, η should be non-negative[32]. The antiferromagnetic zero field model has been extensively studied using field theory and Monte Carlo methods[11, 33] where it was concluded that the $Y - P$ transition is weakly first order since $\eta < 0$. Thus the exponents listed in the second row of Table 6.1 are effective exponents. The correlation length is very large at the critical temperature but does not diverge as required at a second order transition. The results obtained in the present work are listed in the remaining rows of the table. In each case we have used the scaling forms (5.28Finite Size Scaling at Second Order Transitionsequation.5.4.28) to determine ν, β and γ from the best collapse of data for different system sizes. We then use the scaling laws (5.25Continuous phase transitions

: critical exponents, scaling and universalityequation.5.3.24) to estimate α and η.

The transitions between the $V-P$ $C-V$ phases all have $\alpha < 0$ and $\eta > 0$. Meanwhile the $Y-C$ transition has similar exponents but an α that is slightly positive with an η that is positive. These transitions have exponent values close to those of the 3D Heisenberg universality class and are all second order transitions. On the other hand, the $C-P$ transition which occurs at the highest temperature has $\alpha > 0$ and $\eta < 0$. The exponents are very similar to those of the zero field $Y-P$ transition in the second row of the table. We consider that these exponents are effective exponents in the sense that there is a large but finite correlation length at the transition and that the transition is most likely weakly first order.

Table 6.1: Critical Exponents for the 3D Triangular Lattice

Transition	H	T_c	ν	β	γ	α	η
3D Heisenberg[31]	0.0	1.443(1)	0.704(6)	0.362(4)	1.389(14)	-0.112(18)	0.027(2)
Y-P [33]	0.0	0.9574(1)	.661(7)	0.298(3)	1.237(6)	0.169(21)	-0.025(5)
V-P	5.0	0.794(2)	0.68(2)	0.35(2)	1.34(10)	-0.04(6)	0.03(9)
Y-C	2.5	0.263(2)	0.66(2)	0.35(2)	1.28(10)	0.02(6)	0.06(9)
C-V	2.5	0.69(1)	0.77(2)	0.40(4)	1.51(14)	-0.31(6)	0.04(13)
C-P	2.0	0.980(2)	0.58(2)	0.23(2)	1.28(10)	0.26(6)	-0.20(10)
C-P	1.5	0.988(1)	0.47(2)	0.22(2)	0.97(10)	0.59(6)	-0.06(13)

Chapter 7

THE FCC KAGOME LATTICE IN AN APPLIED FIELD

The FCC kagome lattice consists of an ABC stacking of kagome planes along the [111] direction. There are four nearest neighbours in each plane and two in each of the planes above and below. An important example of a material with this three dimensional (3D) kagome structure is $IrMn_3$ which has geometrical magnetic frustration from the eight near-neighbour (NN) antiferromagnetic exchange interactions between the Mn ions. Interest in $IrMn_x$ alloys over the past 15 years has mainly arisen due to applications in spin-valve technology, where they have been widely used as the antiferromagnetic thin film of choice that pins the magnetic moments of an adjacent ferromagnet in the phenomenon known as exchange bias[34, 35, 36, 37]. Although there is no universally accepted microscopic mechanism for exchange bias, magnetic frustration is believed to be important and stoichiometric $IrMn_3$ appears to optimize the desired pinning.

Studies of the magnetic properties of the corresponding two-dimensional (2D) kagome NN Heisenberg antiferromagnet span 25 years due to the macroscopic spin degeneracy of the basic 120° spin structure associated with corner-sharing triangles. Previous Monte Carlo simulations of the NN Heisenberg FCC kagome lattice in zero field have shown that the basic 120° $q = 0$ magnetic structure observed in 2D persists in the 3D case, with the interspin angle being 120° between all eight nearest neighbours[16, 17]. The spin degeneracy is reduced in 3D and exists in the form of sublattice magnetization switching in the [100] stacked kagome planes. This degeneracy is believed to be responsible for the first-order nature of the zero field phase transition at T_N[16].

In this chapter we consider the effect of an applied magnetic field on the spin configurations and we use Monte Carlo methods to determine a phase diagram in the $H - T$ plane as in the case of the stacked triangular lattice. Simulations are carried out for several lattice sizes L and finite size scaling methods are used to determine the critical behaviour of the transitions between various phases. In contrast to the 3D triangular lattice which has one magnetic site per unit cell, the FCC kagome structure has 3 magnetic sites in the unit cell and the total number of sites for size L is $N = 3L^3$. The largest size that was considered in the triangular case was $L = 42$ with $N = L^3$ sites. In this chapter, we limit ourselves to $L = 30$ which corresponds to a slightly larger number of sites.

As in the triangular case all Monte Carlo simulations in this chapter used 10^5 steps, disregarding the initial 10^4 to reduce transients in the data. A random initial seed was used as well.

7.1 Low temperature Analysis

As in the previous chapter, we first carried out simulations at the low temperature $T = 0.01$, as the heat bath method restricts to using non-zero T. The Monte Carlo simulations were performed and the results for the various order parameters compared with the predicted zero temperature values obtained in Chapters 3 and 4. The z-components of the magnetizations per site are plotted in Fig 7.1 along with their predicted values. It is clear that the predictions agree quite well with the values found from the Monte Carlo simulation. Fig. 7.2Monte Carlo results for the perpendicular component (points) of the sublattice magnetizations compared to the predicted values (lines) at low temperaturefigure.7.2 shows the perpendicular sublattice magnetizations per site plotted as a function of the field strength H as well as the predicted values. For fields greater than $H = 4$, we have complete agreement but there appears to be large discrepencies when the field strength $H < 4$ corresponding to the Y-phase

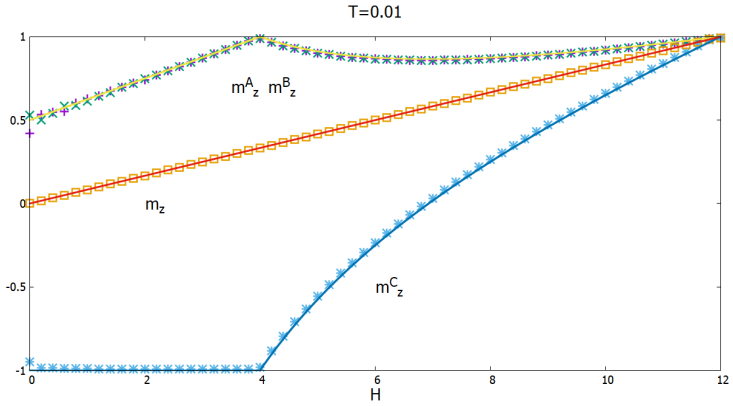

Figure 7.1: Monte Carlo results for the z-component of the magnetizations (points) compared to the predicted values (lines) at low temperature.

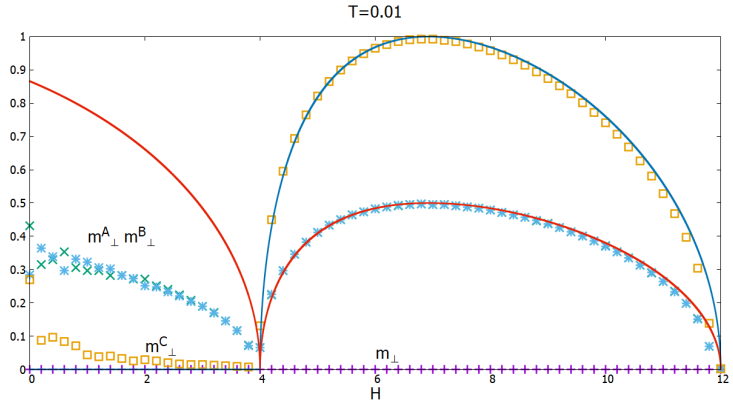

Figure 7.2: Monte Carlo results for the perpendicular component (points) of the sublattice magnetizations compared to the predicted values (lines) at low temperature.

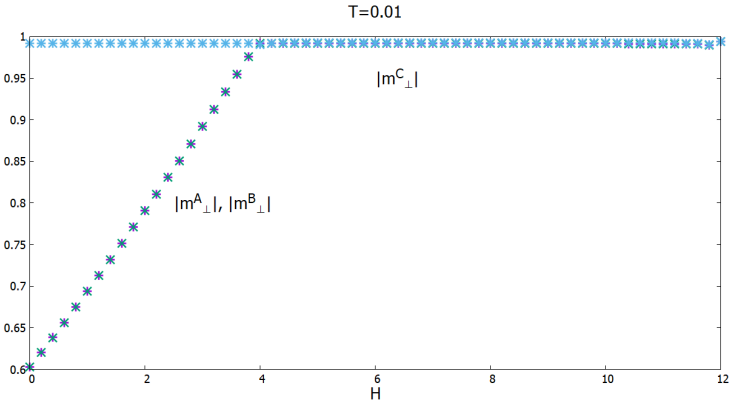

Figure 7.3: Monte Carlo results for the magnitude of the sublattice magnetizations (points) compared to the predicted values(lines) at low temperature.

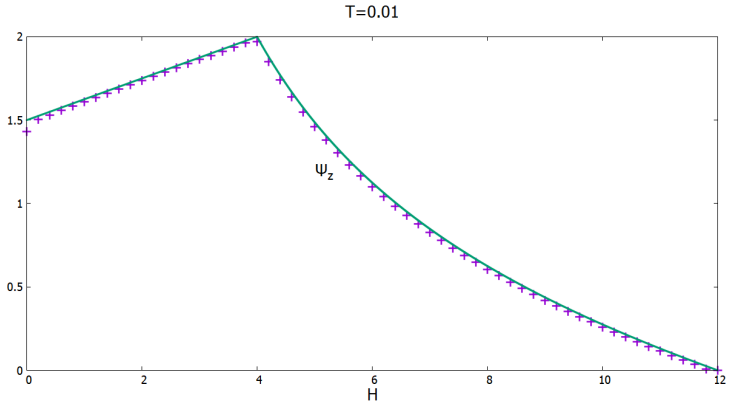

Figure 7.4: Monte Carlo results for the order parameter Ψ_z (points) compared to the predicted value (lines) at low temperature.

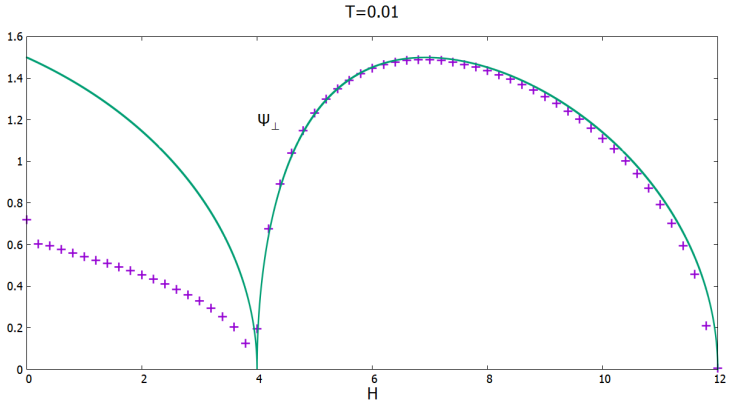

Figure 7.5: Monte Carlo results for the order parameter $\Psi_\perp$ (points) compared to the predicted value (lines) at low temperature.

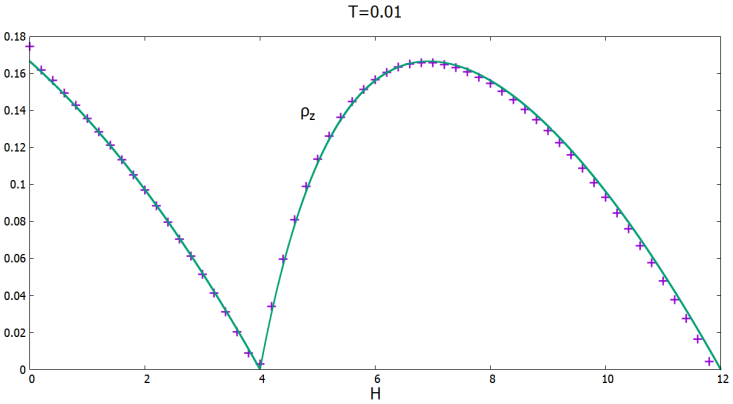

Figure 7.6: Monte Carlo results for the order parameter ρ_z (points) compared to the predicted value (line) at low temperature.

structure. There seems to be significant switching of the magnetizations of two of the sublattices in this range of field strength. As discussed in sections 3.4 and 4.4, there are two different types of switching that can occur: one involves an interchange of two sublattices with unequal z-components and the other corresponds to a rotation of two of the sublattices with equal z-components about the z-axis by 180°. However, since the z-components showed no sublattice switching, we must have the latter type of switching occuring here. Since their z-components are equal the rotation does not affect the magnetization in the z-direction but the perpendicular magnetization is affected as the sublattices are swapping perpendicular components reducing the thermal average. The magnitude of the perpendicular sublattice magnetizations are given by

$$|m_{\perp}^{A,B}| = \sin(\gamma)(1-2x) \tag{7.1}$$

for two of the sublattices where γ was given in (3.10) and x is the fraction of planes in which rotations occur. At zero field, the predicted values are $\sqrt{3}/2$ for two of the sublattices and zero for the third. Fig. 7.2Monte Carlo results for the perpendicular component (points) of the sublattice magnetizations compared to the predicted values (lines) at low temperaturefigure.7.2 clearly shows reductions in the values which are consistent with 30% of the planes rotated. There are also deviations at low field where the spin plane is not completely aligned with the z-axis. These results confirm that the planar spin configurations predicted in chapter 3 are prefered at finite temperature but that the degeneracy associated with sublattice switching is important.

Further evidence for this sublattice switching can be seen when plotting the magnitude of the sublattice magnetizations. The magnitudes of the sublattice magnetizations should remain constant at unity throughout the entire field range. As can be observed in Fig. 7.3Monte Carlo results for the magnitude of the sublattice magnetizations (points) compared to the predicted values(lines) at low temperaturefigure.7.3 there is a sharp drop in the magnitude for two of the sublattices when $H < 4$, the same region where the anomalous perpendicular magnetizations appear. If we com-

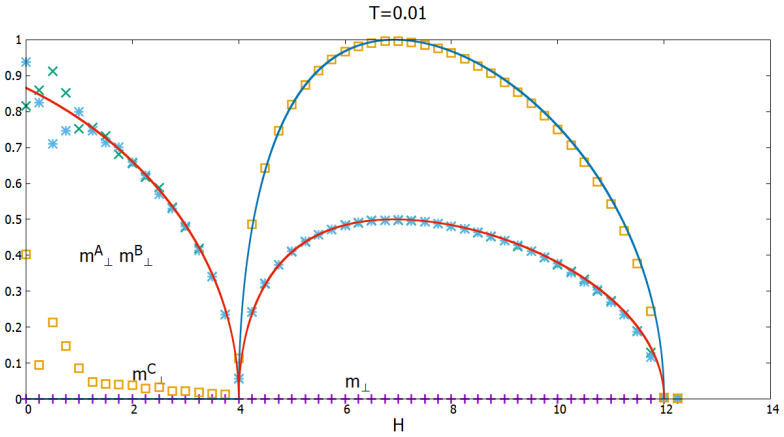

Figure 7.7: Monte Carlo results for the perpendicular component of the sublattice magnetization (points) compared to the predicted values (lines) at low temperature with $J_2 = -0.1|J|$.

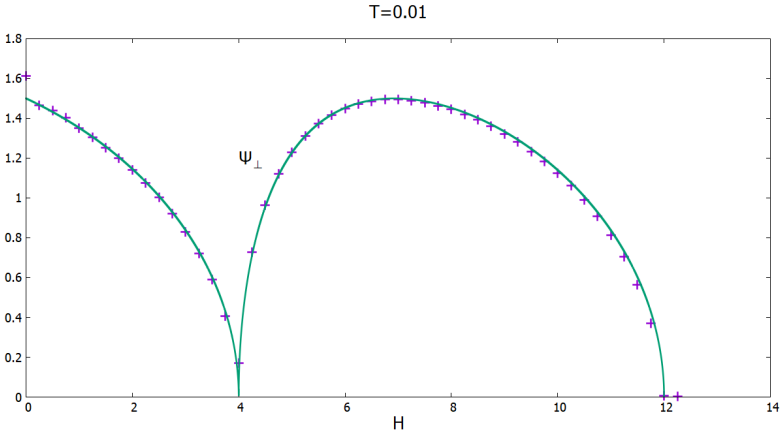

Figure 7.8: Monte Carlo results for the $\Psi_\perp$ order parameter (points) compared to the predicted values (lines) at low temperature with $J_2 = -0.1|J|$.

pare these results with the predictions in (3.14), we find that $x = 0.5 \pm 0.2$ yields a good fit to the results. Hence 30% of the planes have switched sublattices and this indicates that the degeneracy at zero field persists in the Y-Phase.

The order parameters Ψ_z, $\Psi_\perp$ and ρ_z are plotted in Figs. 7.4 - 7.6 and compared with the predicted values from Chapter 4. One can expect that the perpendicular order parameter $\Psi_\perp$ should not completely agree as it is defined in terms of the perpendicular sublattice magnetizations, which were found to undergo sublattice switching for $H < 4$. Figs. 7.4 and 7.6 show that the predicted values for the order parameter Ψ_z and the spin stiffness ρ_z agree quite well with the predicted values, which should come as no surprise since they are not affected by sublattice switching. However, in Fig. 7.5, we see that the results for $\Psi_\perp$ deviate from the predicted values in the region $H < 4$. The value at zero field is again consistent with 30% of the planes undergoing sublattice switching. Unlike the case for the triangular lattice, sublattice switching introduces complications when dealing with the 3D kagome lattice and makes it difficult to extract the critical exponents of the transitions in the range $H < 4$.

The degeneracy associated with the sublattice switching can be removed with the addition of ferromagnetic next-nearest neighbour (NNN) exchange interactions. The NNN lie on the same sublattice and hence the planes containing the A and B sublattice sites are no longer independent and each sublattice will prefer to be aligned. Figs. 7.7Monte Carlo results for the perpendicular component of the sublattice magnetization (points) compared to the predicted values (lines) at low temperature with $J_2 = -0.1|J|$figure.7.7 and 7.8Monte Carlo results for the $\Psi_\perp$ order parameter (points) compared to the predicted values (lines) at low temperature with $J_2 = -0.1|J|$figure.7.8 show the simulation results at $T = 0.01$ when a NNN coupling $J_2 = -0.1|J|$ (negative values are ferromagnetic) is added. The plots clearly indicate that the sublattice switching is eliminated with the addition of J_2 and that the co-planar states are indeed the preferred low energy state. However, there are still deviations from the predicted behaviour at the lowest field values due to the orienta-

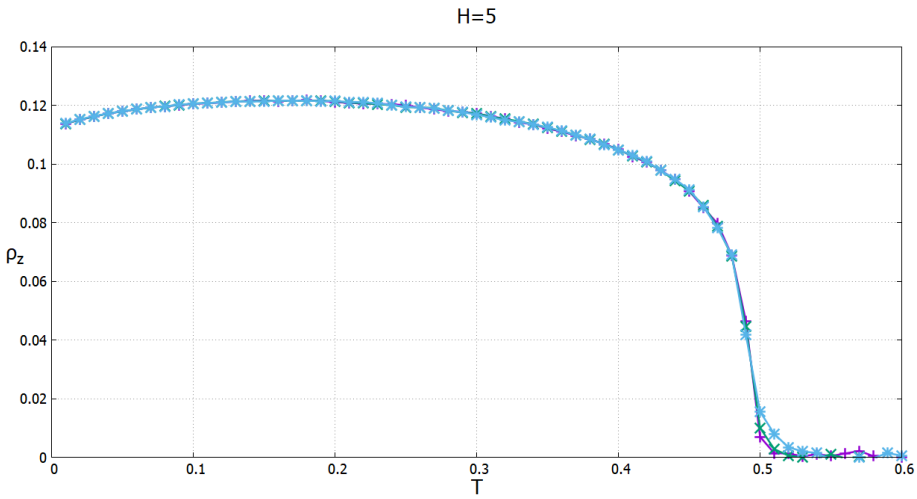

Figure 7.9: The spin stiffness ρ_z at $H = 5$ vs. T.

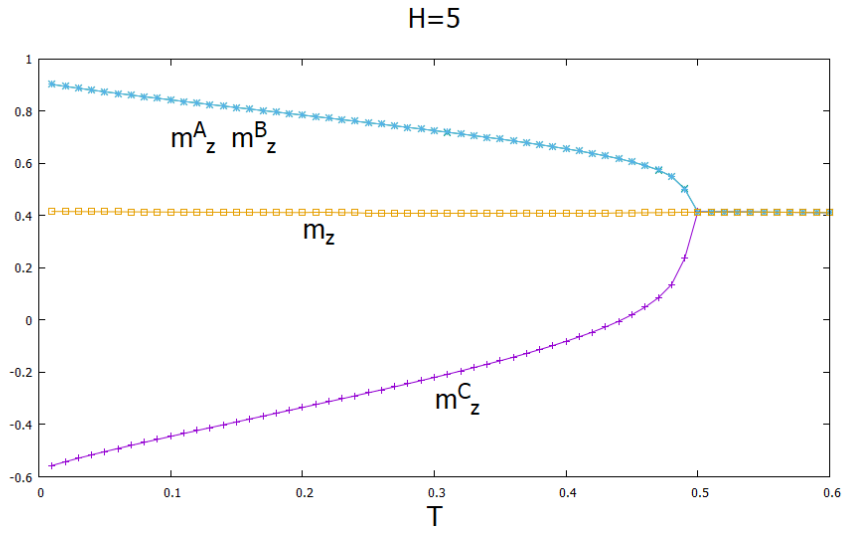

Figure 7.10: The z-sublattice magnetizations and total m_z at $H = 5$ vs. T.

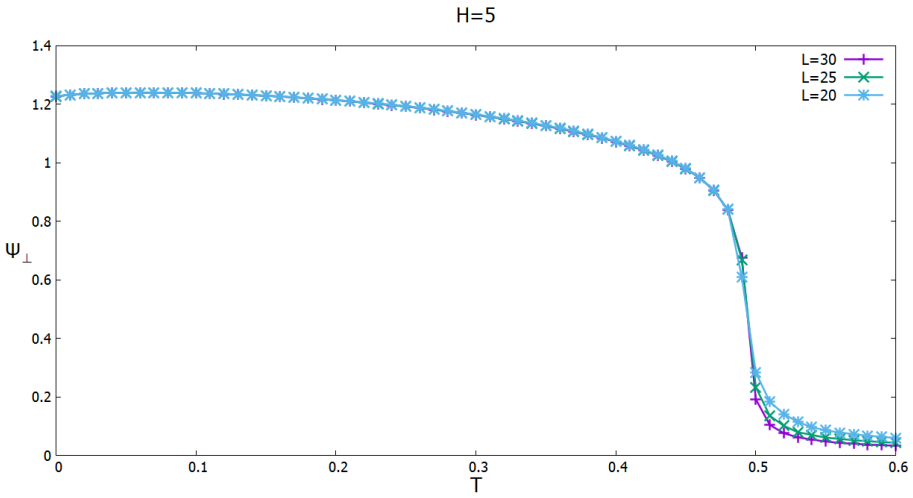

Figure 7.11: The order parameter $\Psi_\perp$ at $H = 5$ vs. T.

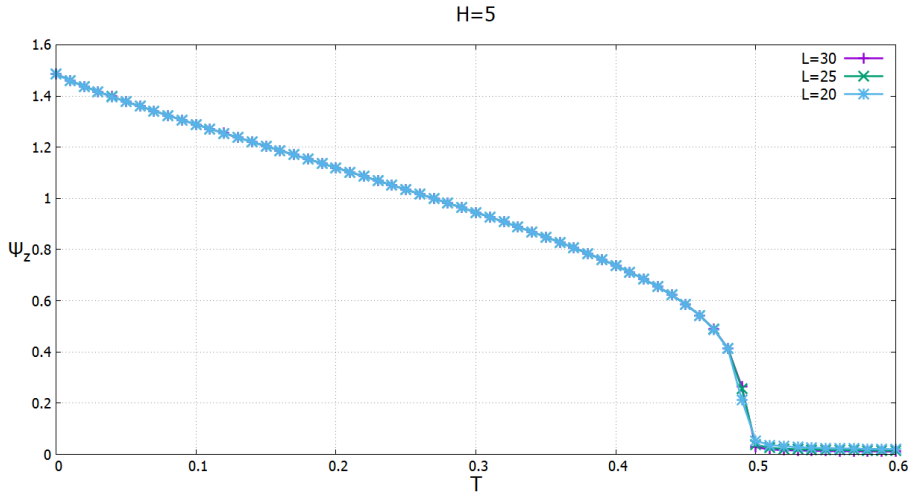

Figure 7.12: The order parameter Ψ_z at $H = 5$ vs. T.

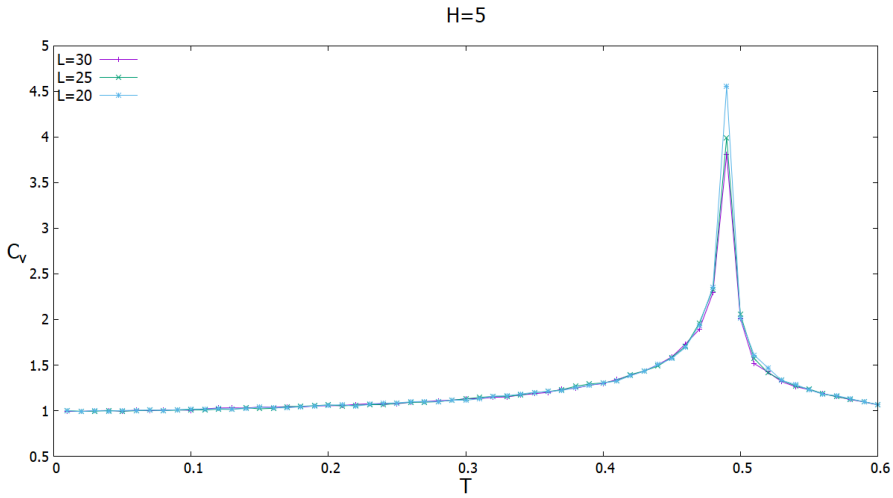

Figure 7.13: The specific heat at $H = 5$ vs. T for $L = 20, 25, 30$.

tion of the spin plane. In our study of the FCC kagome lattice we will take $J_2 = 0$ and only consider nearest-neighbour interactions. The discussion above was to verify that sublattice switching will be an important consideration.

7.2 Fixed Field Results

With the behaviour of the order parameters agreeing with the zero temperature predictions, Monte Carlo simulations were then performed at fixed field while varying temperature. This was done to verify that the order parameters at finite temperature also behave as expected. Fixing the field between $4 < H < 12$ and varying the temperature, the system is expected to be in the V-phase at low temperature. This was done and plotted for lattice sizes $L = 20, 25, 30$ to show finite size effects on the different order parameters. The V-phase is characterized by having non-zero values for all order parameters Ψ_z, $\Psi_\perp$, and ρ_z. The results from the Monte Carlo runs for field $H = 5$ are shown in Figs 7.9 - 7.12. We can see that the order parameters are all non-zero at low temperature and vanish near the same temperature $T_c \sim 0.5$ indicating a transition into the paramagnetic phase. The paramagnetic phase is char-

acterized by having the three order parameters Ψ_z, $\Psi_\perp$ and ρ_z equal to zero. This confirms the expected behaviour of the order parameters in the V-phase and the paramagnetic phase. Using equations (3.12$ZeroTemperatureAnalysisequation$.3.3.12), (4.30$StructureFactorandCorrelationLengthequation$.4.2.30), (4.31$StructureFactorandCorrelatio$ we can predict the values that the order parameters should approach in the zero temperature limit: ρ_z should approach approximately 0.116, m_z approaches approximately 0.4167, Ψ_z should approach 1.4875 and $\Psi_\perp$ should approach approximately 1.227. These predictions are consistent with the results in Figs. 7.9 - 7.12 and serve as another verification of the planar nature of the V-phase. The specific heat per site is shown in Fig. 7.13 for different system sizes and has a sharp peak at the transition to the paramagnetic phase. The peak seems to exhibit slight finite size effects but does not increase with system size. This behaviour suggests that the exponent $\alpha < 0$.

Scanning temperature at a lower fixed field value in the range $0 < H < 4$ was used to verify the behaviour of the order parameters in the remaining phases. Near zero temperature we can expect to find the system in the Y-phase at a fixed field in this field range. Monte Carlo results for a fixed field of $H = 2$ are shown in Figs. 7.14 - 7.17. The Y-phase is characterized again by having the three order parameters Ψ_z, $\Psi_\perp$ and ρ_z non-zero at low T as confirmed in Figs. 7.14. 7.16 and 7.17. As the temperature increases ρ_z and $\Psi_\perp$ fall to zero near $T \sim 0.35$ while Ψ_z remains non-zero. This is indicative of the system entering into the collinear or C-phase. Both ρ_z and $\Psi_\perp$ remain zero while Ψ_z falls to zero at a much larger temperature $T \sim 0.5$. At this temperature, Fig. 7.15 shows that the sublattice magnetizations become equal and corresponding to a transition into the paramagnetic phase.

We can compare the near zero temperature values of the quantities in Figs. 7.14 -7.17 with the predictions in equations (4.16$KagomeLatticeequation$.4.1.16), (4.30$StructureFactorandCorrelationLengthequation$.4.2.30), (4.31$StructureFactorandCorrelatio$ At $H = 2$, ρ_z should approach approximately 0.097, m_z should approach 0.167, Ψ_z should approach 1.75 and $\Psi_\perp$ should approach approximately 1.1456. The first two

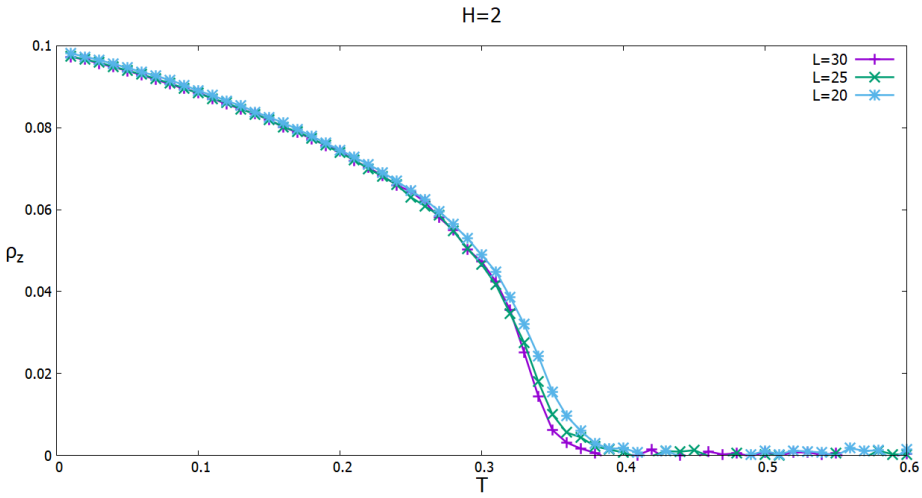

Figure 7.14: The spin stiffness ρ_z at $H = 2$ vs. T.

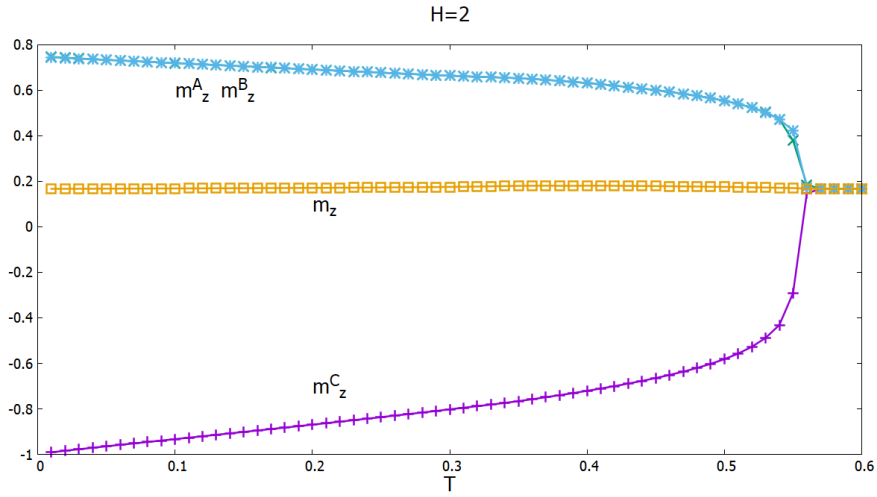

Figure 7.15: The z-sublattice magnetizations at $H = 2$ vs. T.

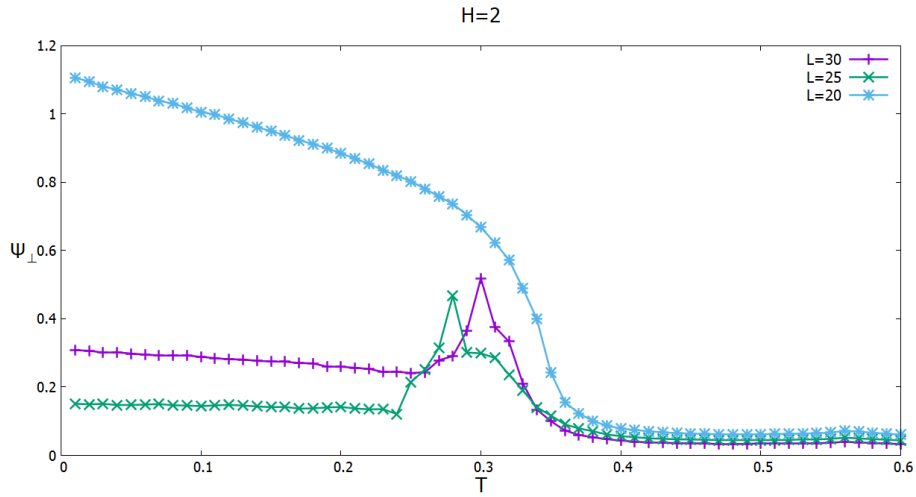

Figure 7.16: The order parameter $\Psi_\perp$ at $H = 2$ vs. T.

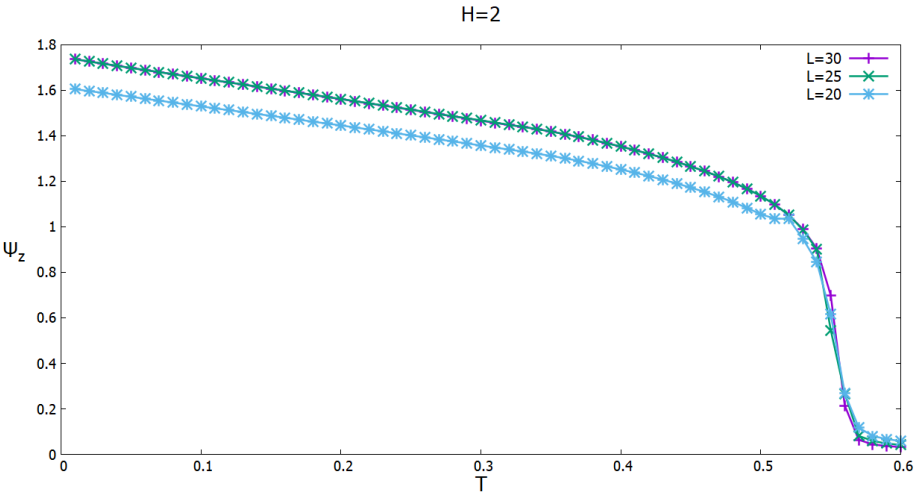

Figure 7.17: The order parameter Ψ_z at $H = 2$ vs. T.

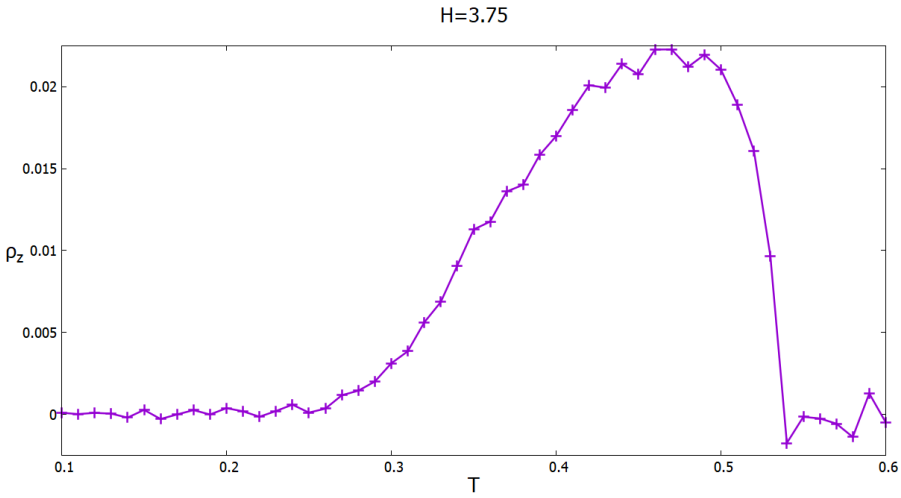

Figure 7.18: The spin stiffness ρ_z at $H = 3.75$ vs. T.

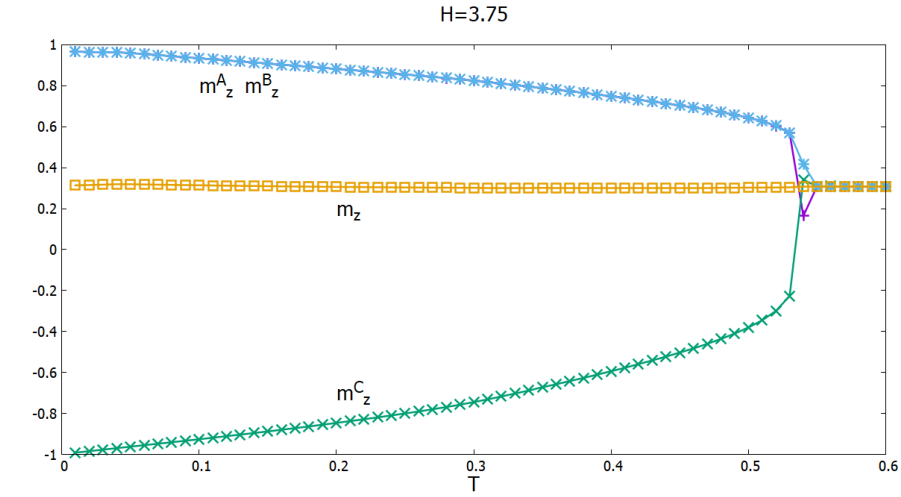

Figure 7.19: The z-sublattice magnetizations at $H = 3.75$ vs. T.

values are consistent with the plots in Figs. 7.14 - 7.17 but the values for Ψ_z and $\Psi_\perp$ are very much reduced for some of the lengths plotted. The reason for this is due to sublattice switching. The switching seems to affect $\Psi_\perp$ for the lengths $L = 30, 25$ at values of T in the Y-phase which corresponds to about 35% of the planes switching in the $L = 30$ case. The plot of $\Psi_\perp$ for the $L = 20$ case seems to approach a fraction of about 0.97 of the correct value. Ψ_z is affected by the sublattice switching only in the $L = 20$ case, which seems to approach 0.91 of the predicted value. This corresponds to a planar switching ratio of $x = 0.06$, thus about 6% of the planes show switching in this case while $L = 25, 30$ seem to approach the correct value. It seems that the $L = 20$ doesn't agree with the results from the larger sizes as it seems to experience switching in the Ψ_z and very little to none in the $\Psi_\perp$ parameter. This is most likely due to the finite size effects, the degeneracy of the collinear phase, and the fact that the sublattice switching may manifest in either the perpendicular components, parallel component or both. This is a more complicated calculation that is not explored further in this thesis.

Figs. 7.18 - 7.21 show the same quantities at a higher field $H = 3.75$. In this case both ρ_z and $\Psi_\perp$ are non-zero at the lowest temperatures but, as the temperature increases, these order parameters become zero near $T \sim 0.04$. However Ψ_z is non-zero both below and above this temperature. This behaviour indicates that the system has transitioned from the Y-phase to the C-phase. As the temperature increases further, both quantities become non-zero indicating a transition to the V-phase near $T \sim 0.3$. At higher temperatures, the system transitions into the paramagnetic phase where all order parameters vanish at a similar temperature $T \sim 0.54$. The predicted values for these quantities at $T = 0$ with $H = 3.75$ are: ρ_z should approach approximately 0.0137, m_z approaches 0.3125, Ψ_z should approach approximately 1.969 and $\Psi_\perp$ should approach approximately 0.4296. Again, $\psi_\perp$ is affected by sublattice switching and in this case approximately 50% of the planes have switched.

The behaviour of these order parameters is consistent with the predictions made

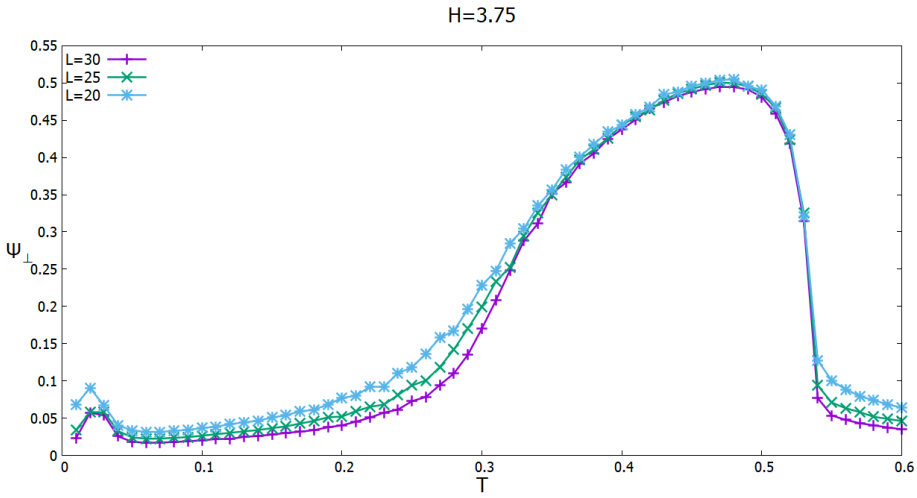

Figure 7.20: The order parameter $\Psi_\perp$ at $H = 3.75$ vs. T.

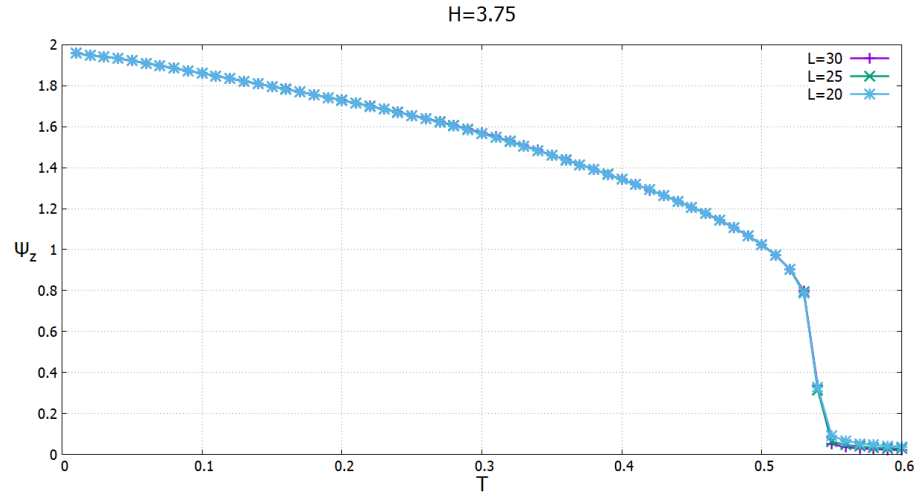

Figure 7.21: The order parameter Ψ_z at $H = 3.75$ vs. T.

in Chapters 3 and 4 of the planar structure of the spin phases but with sublattice switching affecting $\psi_\perp$. However, ρ_z , ψ_z and the z-components of the magnetizations are not affected and can be used as a means to detect the various transition temperatures (except for L=20 and H=2 as discussed earlier). Figs. 7.22 and 7.23 show plots of the specific heat at $H = 2$ and $H = 3.75$ respectively. It can be seen that there is a slight peak at the Y-C transition for $H = 2$ and a much sharper peak at the C-P transition. There is no significant size dependence of the peak which suggests that $\alpha < 0$. For $H = 3.75$ the specific heat does not exhibit peaks at the Y-C and C-V transitions but there is a very large peak at the V-P transition that increases with L suggesting that $\alpha > 0$ contradictory to our observation for $H = 5$ across the V-P transition.

7.3 Phase Diagram

The phase diagram of the Kagome lattice has a similar structure to that of the triangular case with the four distinct regions corresponding to three ordered phases Y, C and V as well as the paramagnetic phase P as shown in Fig. 7.24. As in the triangular case the collinear phase seems to remain stable to higher temperatures than the the other ordered phases. This is most likely due to the high degeneracy of the C-phase as well as the sublattice switching degeneracy. Assuming that all of the transitions between the phases are second order, we use finite size scaling to collapse the data for the order parameters of different system sizes at the transitions to obtain universal curves and critical exponents. We discuss each of the transitions in the following subsections.

7.3.1 V-Phase Transition to Paramagnetic Phase

This transition can be characterized by many different order parameters such as the spin stiffness ρ_z, and both the perpendicular and parallel components of the order

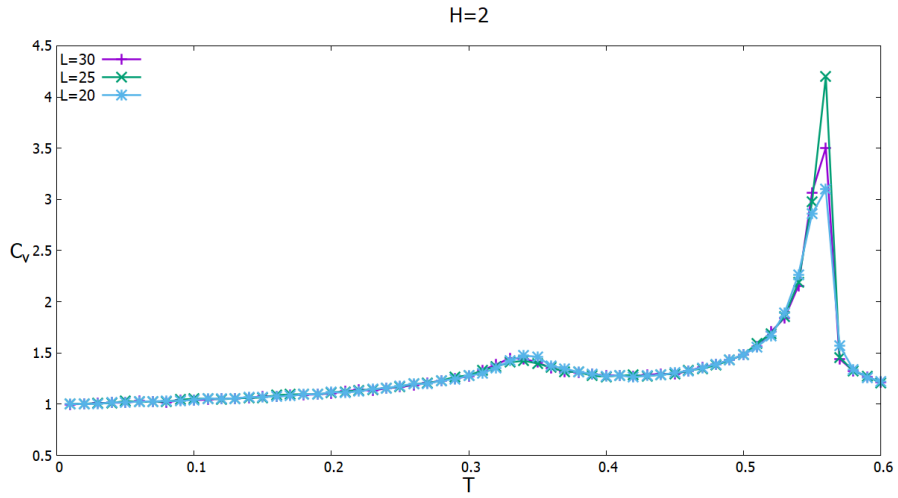

Figure 7.22: The specific heat per site at $H = 2$ vs. T.

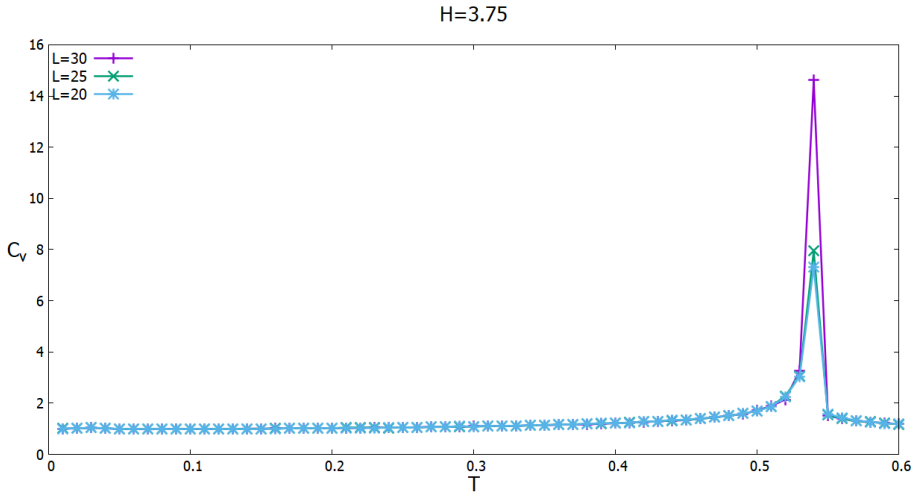

Figure 7.23: The specific heat per site at $H = 3.75$ vs. T.

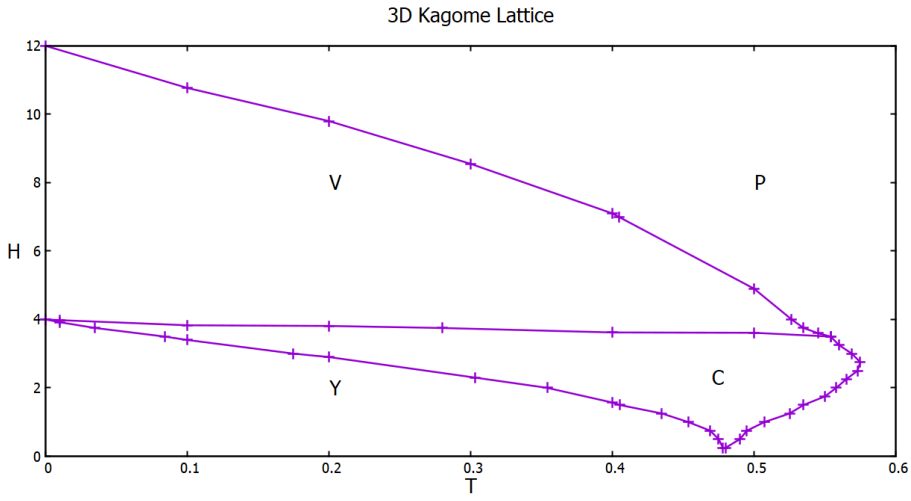

Figure 7.24: The phase diagram of the 3D Kagome lattice.

parameter Ψ_z and $\Psi_\perp$. These order parameters all transition from a finite value to zero as the system enters into the paramagnetic region. We consider the temperature scans at $H = 7$ and we use the spin stiffness to begin our analysis since the scaling form of this parameter only has the two unkowns T_c and ν. A plot of ρL vs. T for several lattice sizes as shown in Fig. 7.25 should cross at a unique temperature to yield an estimate of T_c. We then apply the least squares fitting algorithm to collapse the data to determine the ν exponent as well as a more precise value of the transition temperature. Fig. 7.26The data collapse of the scaled spin stiffness ρL at $H = 7$ with a $\nu = 0.50$. Inset zooms in and shows the collapse near transition with a step size of $\delta T = 0.001$figure.7.26 shows the collapsed data for ρ_z corresponding to $T_c \sim 0.404$ and $\nu \sim 0.50$. The data for $\psi_\perp$ can be collaped with this value of ν and with $\beta \sim 0.22$ and is shown in Fig. 7.27The data collapse of the scaled order parameter $\Psi_\perp$ at $H = 7$ with a $\nu = 0.50$ and $\beta = 0.22$. Inset zooms in and shows the collapse near transition with a step size of $\delta T = 0.001$figure.7.27. The remaining exponents can be obtained using equation (5.25Continuous phase transitions : critical exponents, scaling and universalityequation.5.3.24) and are listed in table 7.1. The exponents in this case

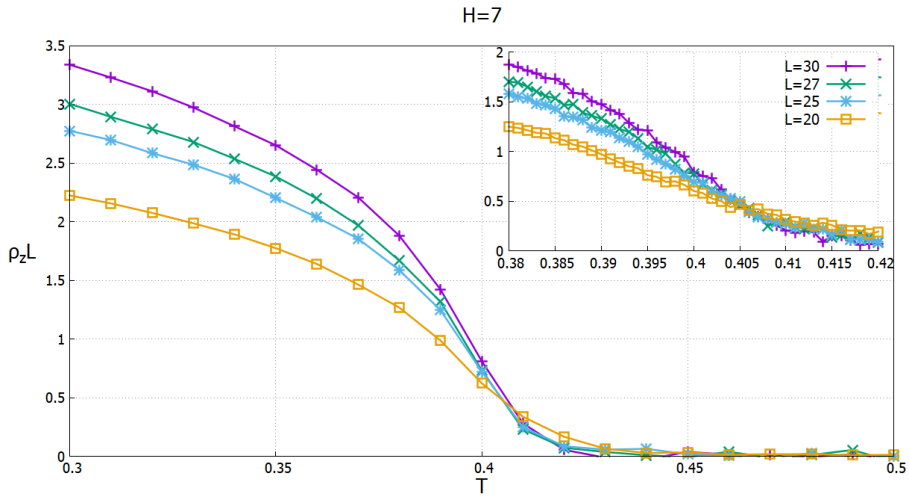

Figure 7.25: The scaled spin stiffness ρL vs temperature allows us to estimate T_c using the crossing point of the different lengths. Inset zooms in near transition with a step size of $\delta T = 0.001$.

seem to differ greatly from the triangular case.

7.3.2 Y-Phase Transition to C-Phase

The Y-phase in the FCC kagome case has the degeneracy mentioned earlier that results in significant sublattice switching in the simulations. The switching can be different for each lattice size and this makes the scaling analysis difficult. Here we consider temperature scans at $H = 3.5$ and our analysis begins by using the scaled spin stiffness $\rho_z L$ for different lengths to identify T_c using the crossing point. Figs. 7.28 and 7.29 show the results for $\Psi_\perp$ and ρ_z with sizes $L = 20, 25, 27, 30$. Unfortunately the sublattice switching mentioned earlier for values of $H < 4$ makes analysis of the transition using the order parameter $\Psi_\perp$ less accurate. Fig. 7.28$\Psi_\perp$ at different lengthsfigure.7.28$showshowtheorderparameterdoesnotseemtovaryonlyduetofinitesizeeffectsasth$ should approach a value of ~ 0.603 however that is clearly not the case in Figure 7.28$\Psi_\perp$ at different lengthsfigure.7.28.$Withtheswitchingaffectingthemagnitudeofthisorderparam$ scaled spin stiffness ρL vs temperature allows us to estimate T_c using the crossing

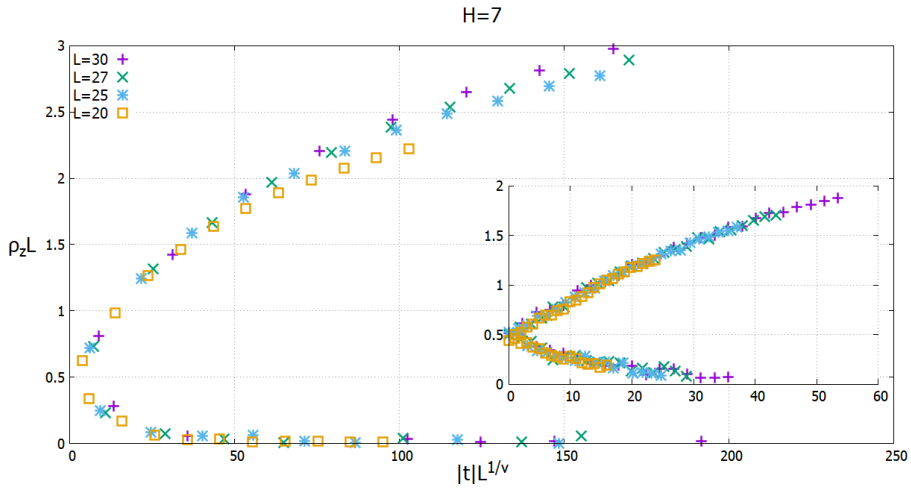

Figure 7.26: The data collapse of the scaled spin stiffness ρL at $H = 7$ with a $\nu = 0.50$. Inset zooms in and shows the collapse near transition with a step size of $\delta T = 0.001$.

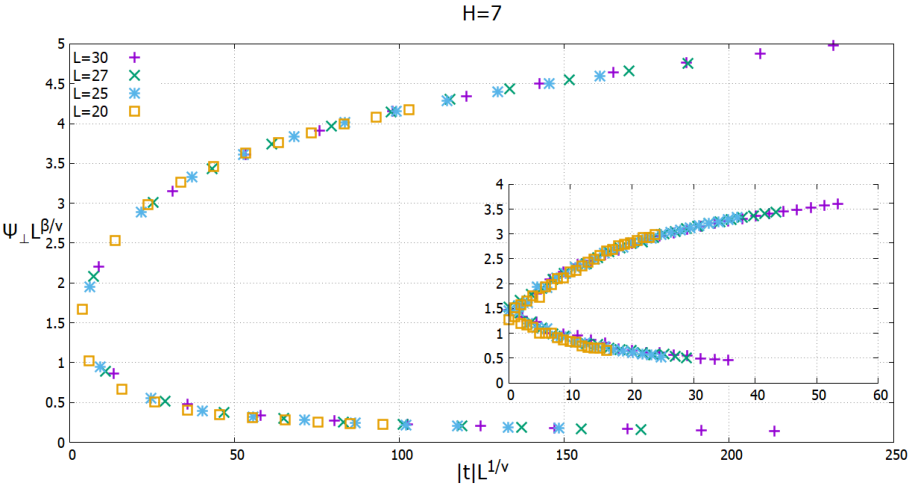

Figure 7.27: The data collapse of the scaled order parameter $\Psi_\perp$ at $H = 7$ with a $\nu = 0.50$ and $\beta = 0.22$. Inset zooms in and shows the collapse near transition with a step size of $\delta T = 0.001$.

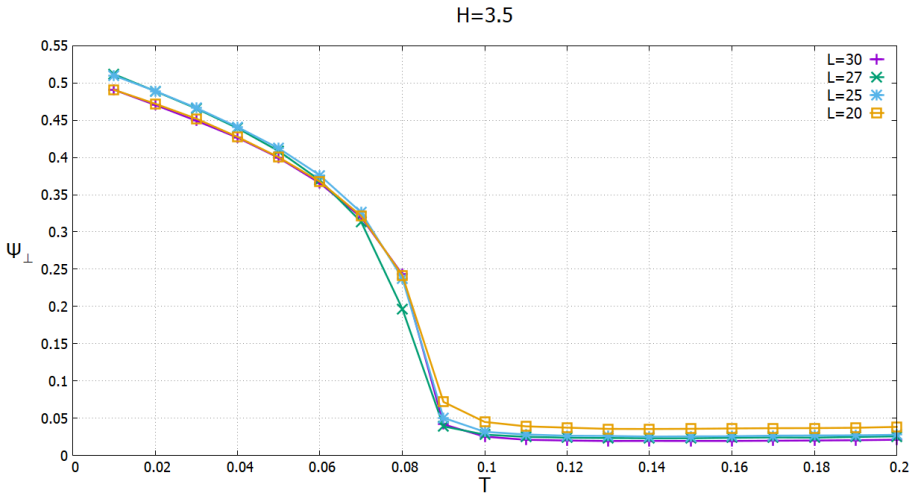

Figure 7.28: $\Psi_\perp$ at different lengths

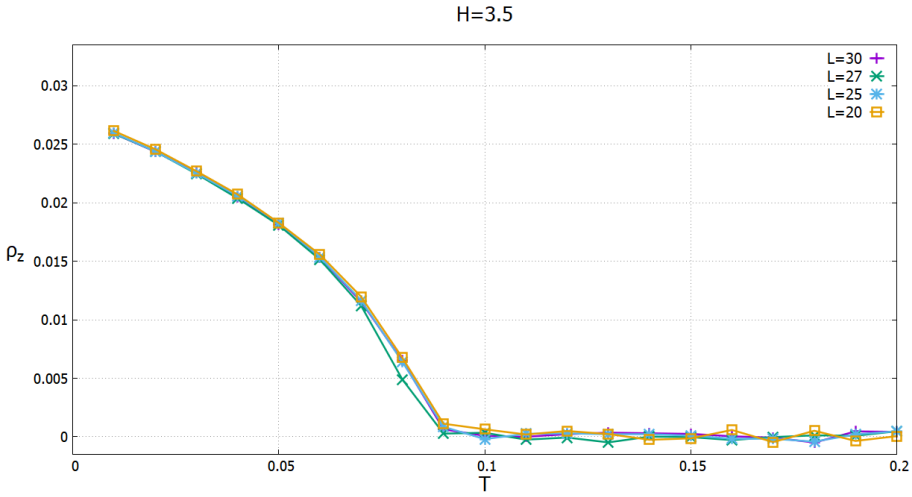

Figure 7.29: ρ_z at different lengths

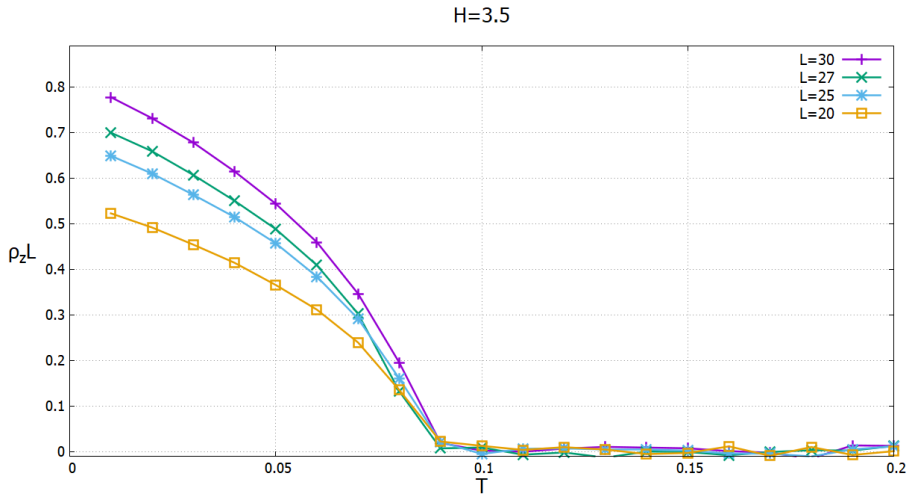

Figure 7.30: The scaled spin stiffness ρL vs temperature allows us to estimate T_c using the crossing point of the different lengths.

point of the different lengthsfigure.7.30$seemstoindicatea\mathrm{T}_c \sim 0.083$ where the curves all meet.

Fig. 7.31$Thedatacollapseofthescaledspinstiffness\rho L$ at $H = 3.5$ with a $\nu = 0.50$figure.7.31$showsthedatareductionof\rho_z$ for sizes $L = 20, 25, 27, 30$ with $T_c \sim .083$ and $\nu \sim 0.50$. A temperature increment of $\delta T = 0.001$ was unable to be used for the spin stiffness to estimate T_c in this case due to its small magnitude near the transition, as can be seen in Figure 7.29ρ_z at different lengthsfigure.7.29.$Thedifferencesintherunsendupmostly$

With these values of T_c and ν a data collapse of $\Psi_\perp$ can be performed. Fig. 7.32 shows the collapse with a $\beta \sim 0.28$. Using the scaling relation it is found that $\gamma \sim 0.96$. Using this result a reasonable collapse of the order parameter susceptibility $\chi_\perp$ is found as shown in Fig. 7.33. With these exponents found the remaining exponents can be found using the exponent scaling relations. The results are listed and discussed further in table 7.1.

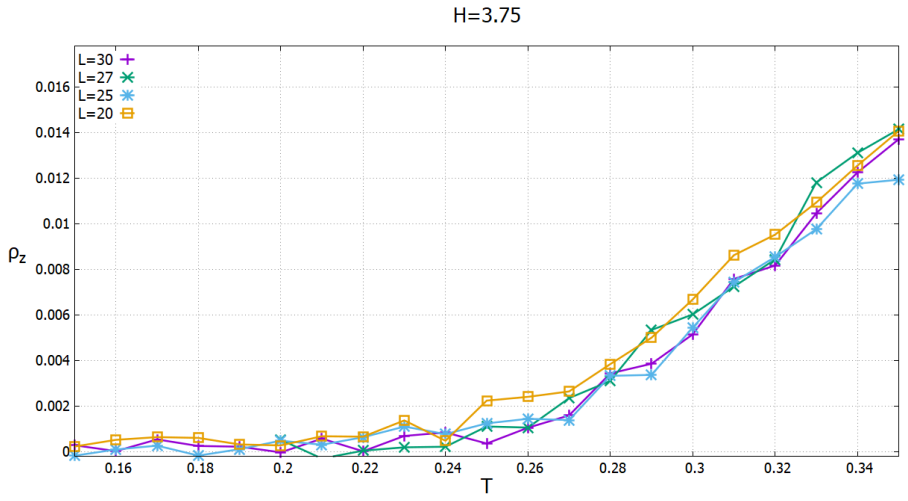

Figure 7.34: The spin stiffness at various lengths at the C-V transition.

7.3.3 C-Phase Transition to V-phase

The Monte Carlo runs used to study the transition from the C-phase to the V-phase also involved sublattice switching. As can be seen from the phase diagram in Fig. 7.24, the transition line is almost horizontal and difficult to pick up using a fixed value of the field. We used $H = 3.75$ to study the spin stiffness and the order parameter $\psi_\perp$ at this transition.

As can be seen in Fig. 7.34 the magnitude is extremely small near the transition and as a result the data is very messy. This is due to the precision of the Monte Carlo run most likely over finite size effects. Finite size analysis will prove ineffective for this transition. However the transition temperature can still be estimated using the previous methods. Fig. 7.35$The scaled spin stiffness vs. \mathrm{T} to find \mathrm{T}_c$ at the C-V transitionfigure.7.35$seems to indicate a \mathrm{T}_c \sim 0.28$. This is supported by a peak in the susceptibility $\chi_\perp$ at that temperature as well as shown in Fig. 7.36.

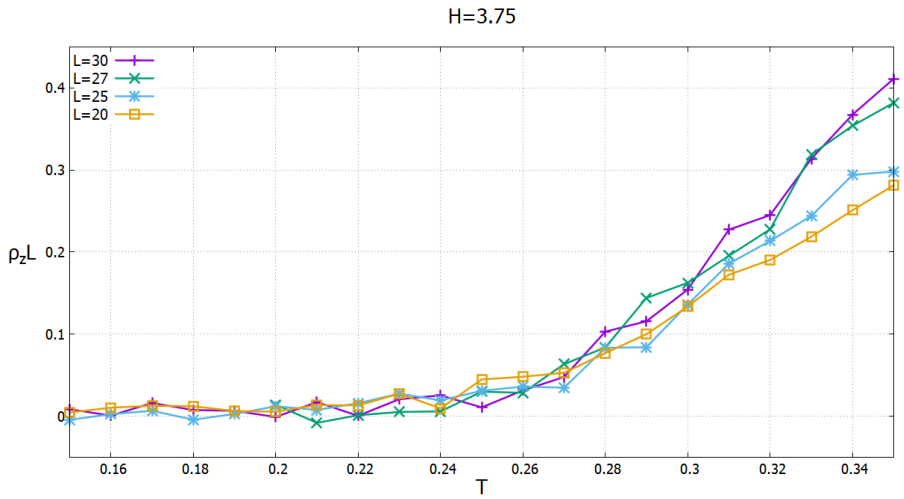

Figure 7.35: The scaled spin stiffness vs. T to find T_c at the C-V transition.

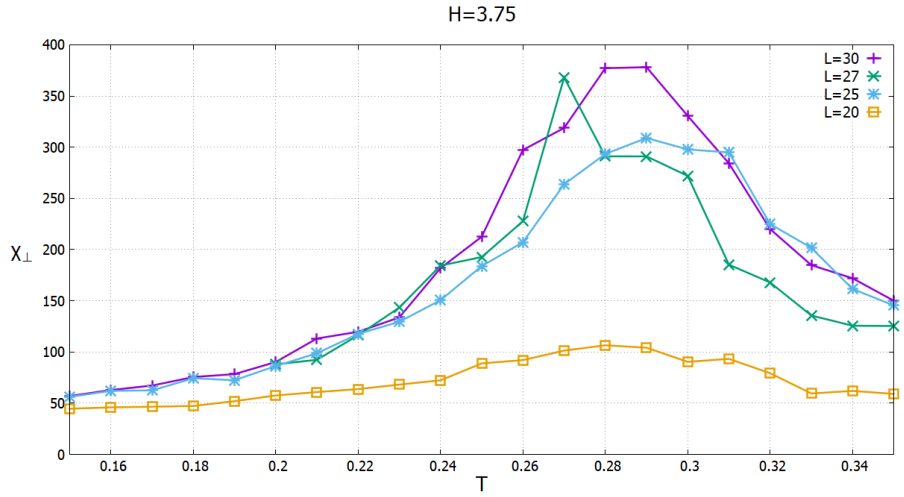

Figure 7.36: The susceptibility of the perpendicular order paramater vs. T to help find T_c at the C-V transition.

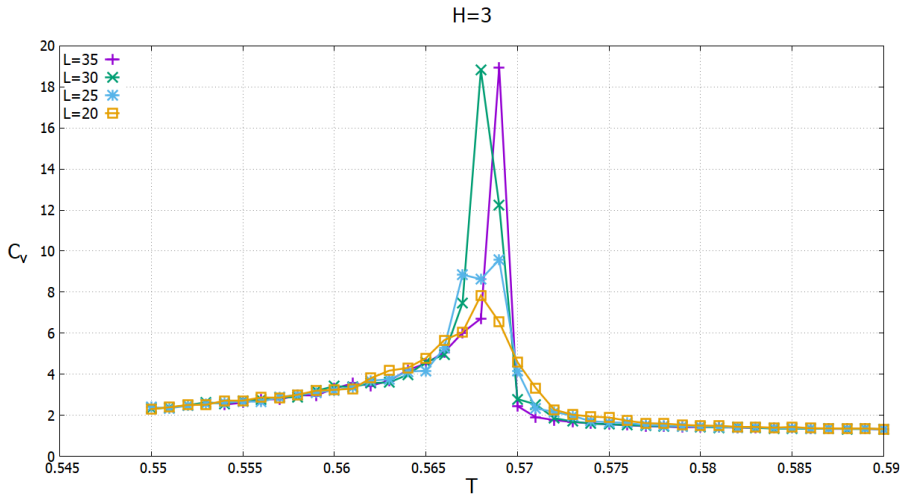

Figure 7.37: The heat capacity at $H = 3$ across the C-P transition. The peak is used to help identify T_c in this case.

7.3.4 C-Phase Transition to Paramagnetic Phase

To characterize this transition the quantity of interest is the parallel order parameter Ψ_z as it is finite in the collinear phase and vanishes in the paramagnetic phase. Unfortunately unlike the triangular case there is no way to find ν using our methods as Ψ_z is our only order paramater in this case and scaling relies on knowledge of β and ν. However using the ν value found for this transition in the triangular case, a fit was attempted by keeping ν constant and adjusting the $\frac{\beta}{\nu}$ ratio. Fig. 7.37$The heat capacity at$H=3$across the C-P transition. The peak is used to help identify$T_c in this casefigure.7.37$shows the heat capacity at this transition. This figure shows a peak at the transitio
0.569 for the largest length, which will be used as our estimate for T_c. Using finite scaling analysis on the results of the Monte Carlo simulations allows us to fit the data using the scaling form of the order parameter. As can be seen in Fig. 7.38The order parameter Ψ_z across the paramagnetic transition at $H = 3$figure.7.38 for $H = 3$ there are significant finite size effects as the order parameter transitions to the paramagnetic phase. A reasonable collapse of the data is obtained in Fig. 7.39The data collapse of

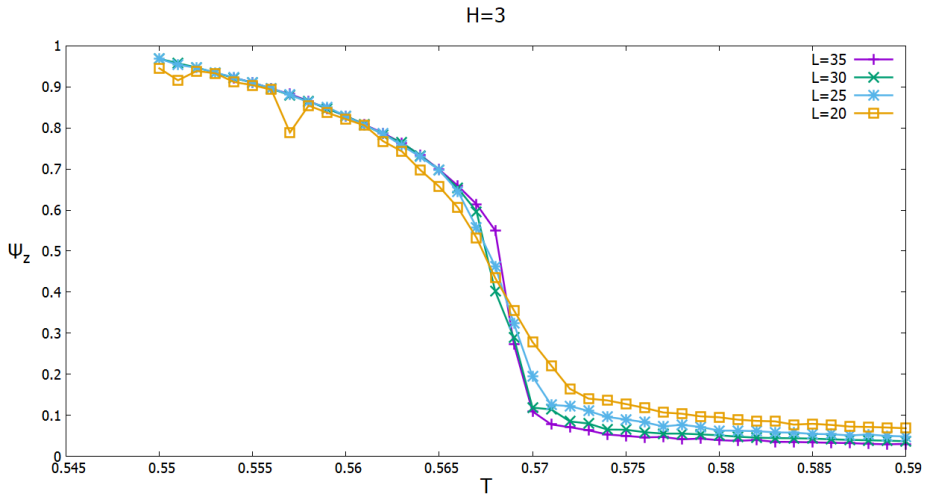

Figure 7.38: The order parameter Ψ_z across the paramagnetic transition at $H = 3$

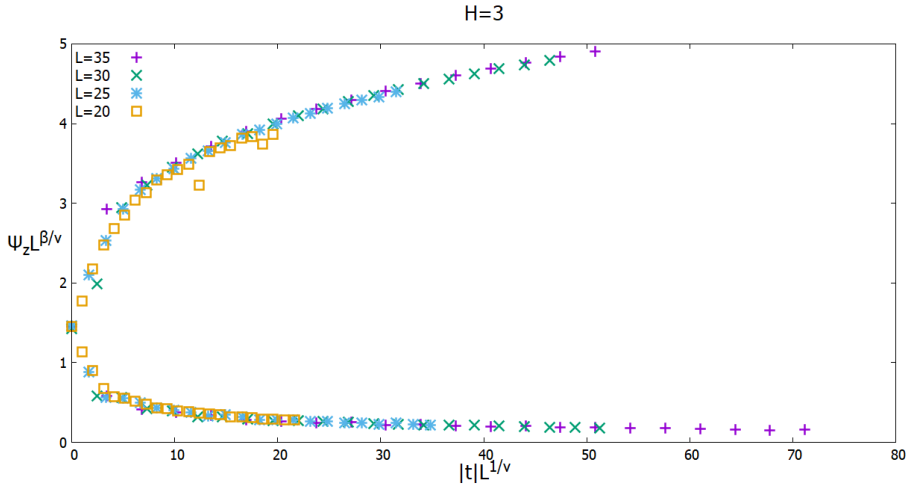

Figure 7.39: The data collapse of order parameter Ψ_z at $H = 3$ with $\nu = 0.47$ and $\beta = 0.22$.

order parameter Ψ_z at $H = 3$ with $\nu = 0.47$ and $\beta = 0.22$figure.7.39 with the values $T_c \sim .569, \nu \sim 0.47$ and $\beta \sim 0.22$ which are very similar values to those found for the triangular lattice at this transition. The remaining exponents are listed in table 7.1. The specific heat exponent $\alpha > 0$ and $\eta < 0$.

7.4 Critical Exponents

The different critical exponents found for the different transitions are compiled in the table below. The first row lists the exponents for the 3D Heisenberg universality class and the second row lists the mean field exponents for a tricritical point. For the $V-P$ transition in the third row at $H = 7$ we find exponents which are closer to those of the tricritical point than the 3D Heisenberg class which suggests that this Data collapse of the correlation length at $H = 1.5$ with a $\nu = 0.47$ and $\beta \approx 0.23$transition is second order and could correspond to tricritical behaviour. The $Y - C$ exponents in the fourth row are also very similar to the tricritical exponents in contrast to those of the triangular lattice for this same transition. The fifth row in the table considers the $C - V$ transition for which a set of exponents could not be found to collapse the data using the methods outlined. Therefore we conclude that scaling does not apply to this transition and that the transition is first order. The final row lists the results for the $C - P$ transition and they coincide with the exponents obtained in the triangular case. Since the set of exponents exactly mirrors the triangular case, coupled with an $\eta < 0$, we conclude that these are effective exponents and that the transition is first order.

Table 7.1: Critical Exponents for the FCC Kagome Lattice

Transition	H	T_c	ν	β	γ	α	η
3D Heisenberg[31]	0.0	1.443(1)	0.704(6)	0.362(4)	1.389(14)	-0.112(18)	0.027(2)
Tricritical	0.0	?	0.5	0.25	1	0.5	0.0
V-P	7.0	0.404(1)	0.50(2)	0.22(2)	1.06(10)	0.50(6)	-0.12(1)
Y-C	3.5	0.083(1)	0.50(2)	0.27(2)	0.96(10)	0.50(6)	0.08(1)
C-V	3.75	0.28(2)	?	?	?	?	?
C-P	3.0	0.569(1)	0.47(2)	0.22(3)	0.97(12)	0.59(6)	-0.06(17)

Chapter 8

SUMMARY AND CONCLUSIONS

In this thesis the magnetic phases of three dimensional frustrated lattices in the presence of an applied field have been studied. The stacked triangular lattice and the FCC kagome lattice consist of triangles of magnetic spins which either share edges of the triangles or vertices. In the case of nearest neighbour anti-ferromagnetic exchange interactions, the triangles are frustrated. In zero applied field, the ground state in both systems has the spins on the neighbours oriented at 120° to one another with zero net moment. Hence the spin state is planar. In the presence of an applied field, the 120° configuration is distorted and the states evolve as the field increases. In chapter 3 we outlined the possible states. There is a high degeneracy at zero temperature and three types of planar states are possible: the Y, C and V states are characterized by three sublattices with different orientations. Non-planar states are also possible but our Monte Carlo simulations at finite temperatures confirm that the planar states are favoured.

The FCC kagome lattice differs from the stacked triangular case in an interesting manner which yields many more degenerate planar ground states. In the Y-phase, two of the sublattices in a plane can be switched with no change in the energy. This sublattice switching is absent in the triangular lattice and complicates the study of the critical properties for the kagome lattice in the field range $H < 4$. We obtained phase diagrams in the $H - T$ plane for both systems which are quite similar. There are three ordered phases Y, C and V as well as the high T and high H paramagnetic phase P. In both cases, the collinear phase is the phase which remains stable to the highest temperature. This phase has one sublattice parallel to the field direction and

the other two sublattices anti-parallel. However, the orientation of the anti-parallel sublattices is arbitrary and hence the phase is highly degenerate. This entropic feature could be responsible for stabilizing the phase to higher T.

We used finite size scaling methods to study the critical behaviour of the transitions betweem the four phases for both systems. For the triangular lattice, the $V-P$, $Y-C$ and $C-V$ transitions have critical exponents that are very similar to those of the 3D Heisenberg universality class. We conclude that these transitions are all second order transitions. The $C-P$ transition at the highest temperatures has very different exponents and the correlation length exponent η is negative. This behaviour was also found previously in zero field where it was concluded that the exponents were effective exponents and that the transition was first order. We conclude that the $C-P$ transition in this case is first order and is most likely associated with the high degeneracy of the ordered phase. For the FCC kagome lattice, we find somewhat different results with one exception. The $Y-C$ and $V-P$ transitions have exponents that are close those of a mean field tricritical point and are second order transitions. A data collapse for the $C-V$ transition was not achieved due to a combination of sublattice switching and the high degeneracy of the collinear phase. As a set of exponents was not found we conclude that the $C-V$ transition in this case is first order. The $C-P$ transition has exponents almost identical to those of the triangular lattice and we conclude that the transition in this case is also first order.

The different nature of the continuous transitions in the frustrated systems appear to be due to the degeneracies of the FCC kagome lattice. Although both lattices have the same number of nearest neighbours, all of the nearest neighbours in the Kagome case are frustrated. Where only six of the eight nearest neighbours in the triangular case are frustrated.

Potential future studies into these frustrated lattices could involve Monte Carlo simulations at larger system sizes and Monte Carlo steps. Modifications to the Hamiltonian can also be considered such as including next nearest neighbour terms when

calculating the exchange energy, this would be useful in the Kagome case as it was shown in this thesis that it alleviates the sublattice switching problem encountered. One can also consider including additional interactions such as dipole interactions and anisotropies.

Another study which could yield interesting results is having anti-ferromagnetic interplanar interactions for the stacked triangular lattice. This could yield some interesting new phase structures and would probably lend itself to a six sublattice decomposition. The additional frustration due to the additional frustrated neighbours coupled with a possible six sublattice decomposition could yield some interesting physics.

BIBLIOGRAPHY

[1] M F Collins and O A Petrenko. Triangular antiferromagnets. *Canadian Journal of Physics*, 75(9):605–655, 1997.

[2] Hikaru Kawamura. Spin-wave analysis of the antiferromagnetic plane rotator model on the triangular lattice-symmetry breaking in a magnetic field. *Journal of the Physical Society of Japan*, 53(8):2452–2455, 1984.

[3] S E Korshunov. Phase diagram of the antiferromagnetic xy model with a triangular lattice in an external magnetic field. *Journal of Physics C: Solid State Physics*, 19(29):5927, 1986.

[4] M. L. Plumer, A. Caillé, and Kevin Hood. Multicritical points in the magnetic phase diagrams of axial and planar antiferromagnets. *Phys. Rev. B*, 39:4489–4499, Mar 1989.

[5] M. L. Plumer and A. Caillé. Magnetic phase diagrams of the antiferromagnetic planar model on a stacked triangular lattice. *Phys. Rev. B*, 42:10388–10396, Dec 1990.

[6] M. L. Plumer, A. Mailhot, and A. Caillé. Magnetic-field-induced first-order transition in the frustrated xy model on a stacked triangular lattice. *Phys. Rev. B*, 48:3840–3843, Aug 1993.

[7] Hikaru Kawamura and Seiji Miyashita. Phase transition of the heisenberg antiferromagnet on the triangular lattice in a magnetic field. *Journal of the Physical Society of Japan*, 54(12):4530–4538, 1985.

[8] A. K. Murtazaev, M. K. Ramazanov, and M. K. Badiev. Monte carlo investigation of phase transitions in the frustrated heisenberg model on a triangular lattice. *Physics of the Solid State*, 52(8):1673–1679, 2010.

[9] Luis Seabra, Tsutomu Momoi, Philippe Sindzingre, and Nic Shannon. Phase diagram of the classical heisenberg antiferromagnet on a triangular lattice in an applied magnetic field. *Phys. Rev. B*, 84:214418, Dec 2011.

[10] J. Villain, R. Bidaux, J.-P. Carton, and R. Conte. Order as an effect of disorder. *J. Phys. France*, 41(11):1263–1272, 1980.

[11] B W Southern. Triangular antiferromagnets and universality. *Physics in Canada*, 68(2):83, 2012.

[12] A. B. Harris, C. Kallin, and A. J. Berlinsky. Possible néel orderings of the kagomé antiferromagnet. *Phys. Rev. B*, 45:2899–2919, Feb 1992.

[13] David A. Huse and Andrew D. Rutenberg. Classical antiferromagnets on the kagomé lattice. *Phys. Rev. B*, 45:7536–7539, Apr 1992.

[14] Jan N. Reimers and A. J. Berlinsky. Order by disorder in the classical heisenberg kagomé antiferromagnet. *Phys. Rev. B*, 48:9539–9554, Oct 1993.

[15] M. E. Zhitomirsky. Field-induced transitions in a kagomé antiferromagnet. *Phys. Rev. Lett.*, 88:057204, Jan 2002.

[16] V. Hemmati, M. L. Plumer, J. P. Whitehead, and B. W. Southern. Monte carlo simulations of magnetic ordering in the fcc kagome lattice. *Phys. Rev. B*, 86:104419, Sep 2012.

[17] M. D. LeBlanc, B. W. Southern, M. L. Plumer, and J. P. Whitehead. Spin waves in the anisotropic fcc kagome antiferromagnet. *Phys. Rev. B*, 90:144403, Oct 2014.

[18] Riley McGouran. Magnetic phase diagram of the fcc kagome lattice in a magnetic field. Bachelor thesis, University of Manitoba, 2013.

[19] A.P.M Dirac. *On the theory of Quantum mechanics. Proc. Royal Society*, 112A:661, 1926.

[20] W. Heisenberg. *Zur theorie des ferromagnetismus. Zeits. fur Physik*, 49:619, 1928.

[21] Izumi Tomeno, Hiromi N. Fuke, Hitoshi Iwasaki, Masashi Sahashi, and Yorihiko Tsunoda. Magnetic neutron scattering study of ordered Mn_3Ir. *Journal of Applied Physics*, 86(7):3853–3856, 1999.

[22] Ornstein L S and Lorentz H A. Accidental deviations of density and opalescence at the critical point of a single substance. *Royal Netherlands Academy of Arts and Sciences (KNAW), Proceedings*, 17(II):793–806, 1914.

[23] M. E. Fisher. The renormalization group in the theory of critical behavior. *Rev. Mod. Phys.*, **46**:597, 1974.

[24] M. E. Fisher. The theory of critical point singularities. In M. S. Green, editor, *Critical Phenomena, Proceedings of the 51st Enrico Fermi School*. Academic Press, 1971.

[25] M. E. Fisher and M. N. Barber. Scaling theory for finite-size effects in the critical region. *Phys. Rev. Lett.*, **28**:1516, 1972.

[26] John Cardy. *Scaling and Renormalization in Statistical Physics.* Cambridge University Press, 1996.

[27] L. P. Kadanoff and F. J. Wegner. Some critical properties of the eight-vertex model. *Phys. Rev. B*, **4**:3989, 1971.

[28] B.D. Gaulin. Experimental studies of geometrically-frustrated magnetic systems. In H.T. Diep, editor, *Magnetic Systems with Competing Interactions*, page 286. World Scientific, 1994.

[29] Hikaru Kawamura. Universality of phase transitions of frustrated antiferromagnets. *J. Phys.: Condens. Matter*, **10**:4707, 1998.

[30] O. Melchert. "autoscale.py" a program for automatic finite-size scaling analyses: A users guide. *arXiv:0910.5403 [physics.comp-ph]*, 2009.

[31] Christian Holm and Wolfhard Janke. Critical exponents of the classical three-dimensional heisenberg model: A single-cluster monte carlo study. *Phys. Rev. B*, 48:936–950, Jul 1993.

[32] J. Zinn-Justin. *Quantum Field Theory and Critical Phenomena, 4th ed.* Oxford University Press, 2002.

[33] Mirsaeed Zelli, K. Boese, and B. W. Southern. Short-time dynamics study of heisenberg noncollinear magnets. *Phys. Rev. B*, 76:224407, Dec 2007.

[34] K. O'Grady, L. E. Fernandez-Outon, and Gonzalo Vallejo Fernandez. A new paradigm for exchange bias in polycrystalline thin films. *Journal of Magnetism and Magnetic Materials*, 322(8):883–899, 4 2010.

[35] Masakiyo Tsunoda, Hirokazu Takahashi, Tetsuya Nakamura, Chiharu Mitsumata, Shinji Isogami, and Migaku Takahashi. Linear correlation between uncompensated antiferromagnetic spins and exchange bias in mnir/co100xfex bilayers. *Applied Physics Letters*, 97(7):072501, 2010.

[36] A. Kohn, A. Kovcs, R. Fan, G. J. McIntyre, R. C. C. Ward, and J. P. Goff. The antiferromagnetic structures of irmn3 and their influence on exchange-bias. *Scientific Reports*, 3:2412, 2013.

[37] R. Yanes, J. Jackson, L. Udvardi, L. Szunyogh, and U. Nowak. Exchange bias driven by dzyaloshinskii-moriya interactions. *Phys. Rev. Lett.*, 111:217202, Nov 2013.